To the Graduate Council:
I am submitting herewith a dissertation written by Casey Morean entitled "Short Range Correlation measurements in the quasielastic region with an 11 GeV beam." I have examined the final electronic copy of this dissertation for form and content and recommend that it be accepted in partial fulfillment of the requirements for the degree of Doctor of Philosophy, with a major in Physics.

Nadia Fomin, Major Professor

We have read this dissertation
and recommend its acceptance:

Nadia Fomin

Robert Grzywacz

Maik Lang

Miguel Madurga

Thomas Papenbrock

Accepted for the Council:

Dixie L. Thompson

Vice Provost and Dean of the Graduate School

(Original signatures are on file with official student records.)

Short Range Correlation measurements in the quasielastic region with an 11 GeV beam

A Dissertation Presented for the

Doctor of Philosophy

Degree

The University of Tennessee, Knoxville

Casey Morean

December 2023

© by Casey Morean, 2023
All Rights Reserved.

Acknowledgements

It is difficult to list hear all the people who have helped me achieve my PhD since I have worked towards this goal since 10^{th} grade. Please know the pages adorning this document are not expansive enough to express my appreciation to all those who have shaped my life and career.

I thank God, my creator, for the capacity to study the natural world we collectively experience. I appreciate that pleasure can be derived from the study and interpretation of the things around us.

I could not have been born into a more loving and supportive family. I thank my parents, Cindy and Alan Morean, for answering the endless questions I would ask about the world around me. My grandfather, Jim Morean, always had a moment to explain the tools in his workshop and how they worked. It is the nurturing environment provided by my family and the formative memories from those experiences I would like to thank them for most.

Although I went to a small school, I was able to take advanced classes and independent studies because of the connections I made with teachers. I appreciate Mr. Bauer's attention to detail in physics experiments, Mrs. Beck's focus on coding projects, and Mrs. Tripodi's extra credit assignment on quarks.

Thank goodness the economy was still struggling in 2013 when I went to college, so the greatest group of honors students and physics majors could come together at Lock Haven University of Pennsylvania. I thank the many people in the honors program who helped me find my voice in crowds. A very near group in my heart

are my roommates, Brett Powell, Roman Marijczuk, John Wilkinson, Seth Peeler, and Meghan Tanner. I thank them all for the many hours spent toiling in front of whiteboards. Finally, the most instrumental person of my early physics career is John Reid. This man has knack for teaching, and the independent studies and cosmic ray physics experiments we did are the reason I do what I do today.

I thank Nadia Fomin, my advisor, for allowing me to move to Jefferson Lab. In this environment, I was exposed to many experts across multiple fields and became responsible for my own research. Nadia was always available when needed and supported me, even on occasions when I failed to meet expectations.

During graduate school, I was fortunate to work with many people at Jefferson Lab and from several Universities across the world. I thank Sebastian Seeds, Provakar Datta, Maria Satnik, and Abishek Karki for many constructive discussions. Dave Gaskell of Thomas Jefferson National Accelerator Facility, is one of my favorite people I have ever worked with. He is a walking encyclopedia of all things JLab related, and he is a smart and charismatic man. I am fortunate to have worked closely with him.

Finally, I thank my wife, Hayley Morean, for unconditional love and support through many trying times the past 5 years. Without her support, the very words on this page would likely not be written.

Abstract

Electron scattering is a powerful tool for studying high momentum nucleon and quark distributions in nuclei. Thomas Jefferson National Accelerator Facility (JLab) with its 11 GeV beam is capable of studying high momentum nucleons with unmatched precision. The role of short range nucleon configurations and quark distributions is significant for understanding the dynamics of nuclei and their underlying components. Scattering cross section measurements in the kinematic regime $x > 1$, a region forbidden to the free nucleon, are sensitive to high momentum nucleons, which are believed to come from short range correlations (SRCs). SRCs are strongly interacting, high momentum nucleons with a low center-of-mass momentum that are highly decoupled from the nuclear environment. The focus of this research is on precision measurements of 2N SRCs, the observation of 3N SRCs, and the measurement of parton distribution functions at $x > 1$[1].

Table of Contents

1 Introduction **1**

1.1 Elastic Scattering 4

1.2 Inelastic Scattering and Nucleon Resonances 6

1.3 Quasi-Elastic Scattering 9

1.4 Background on Short Range Correlations 11

1.4.1 Independent Particle Shell Model 12

1.4.2 Exclusive Measurements and Shell Occupancy 14

1.4.3 Short Distance Nucleon-Nucleon Interaction 16

1.4.4 Short Range Correlations 21

1.5 XEM2 Experiment: E12-06-105 21

1.6 The EMC Effect and SRCs 24

2 Experiment Setup **29**

2.1 CEBAF Accelerator 29

2.2 Hall C Beamline 32

2.2.1 Beam Position and Profile Measurement 34

2.2.2 Beam Energy Measurement 36

2.2.3 Beam Current Monitors 37

2.2.4 Beam Raster 40

2.3 Target Ladder 43

2.3.1 Cryotargets 43

2.3.2 Solid Targets 46
2.4 Spectrometers 46
2.4.1 Spectrometer Magnets and Optics 48
2.4.2 Event Reconstruction 48
2.4.3 SHMS Capabilities 50
2.5 Detectors 53
2.5.1 Hodoscopes 53
2.5.2 Drift Chambers 55
2.5.3 Gas Čherenkov 57
2.5.4 Lead Glass Calorimeters 62
2.6 Data Acquisition and Trigger 64
2.6.1 Trigger Configurations 64
2.6.2 CODA Event Types 65

3 Inclusive Data Analysis 67
3.1 Detector Calibrations 67
3.1.1 Reference Times and Timing Windows 68
3.1.2 Timing Windows 69
3.1.3 Hodoscope Calibration 71
3.1.4 Čherenkov Calibration 74
3.1.5 Drift Chamber Calibration 76
3.1.6 Calorimeter Calibration 81
3.2 Computer and Electronic Dead Time 83
3.2.1 Total Dead Time and the EDTM System 85
3.2.2 Computer Live time 87
3.2.3 Electronic Dead Time 87
3.2.4 Live Time Systematic Errors 88
3.3 Optics and Offsets 91
3.3.1 Momentum Offsets 93

3.3.2 Spectrometer Offsets . . . 93
3.4 Efficiencies . . . 95
3.4.1 Noble Gas Čherenkov Efficiency . . . 95
3.4.2 Calorimeter Efficiency . . . 96
3.4.3 Tracking Efficiency . . . 96
3.4.4 Trigger Efficiency . . . 99
3.5 Electron Yield Corrections . . . 101
3.5.1 Target Corrections . . . 101
3.5.2 Cryogenic Target Boiling . . . 101
3.5.3 Charge Symmetric Background . . . 104
3.5.4 Pion Contamination . . . 107
3.5.5 Charge Normalized Yield . . . 109

4 Cross Section Extraction **113**
4.1 Cross Section Extraction . . . 113
4.1.1 Cross Section Extraction Methodology . . . 113
4.1.2 Monte-Carlo Ratio Method . . . 114
4.2 Radiative Corrections . . . 114
4.3 Cross Section Model . . . 115
4.3.1 Coulomb Corrections . . . 117
4.3.2 Iterative model cross-section . . . 117
4.4 Systematic Errors . . . 118

5 Results and Conclusion **120**
5.1 Cross Sections . . . 120
5.2 Inclusive SRC Ratios . . . 120
5.3 a_2 Ratios and Scaled Nuclear Density . . . 123
5.4 Summary and Conclusion . . . 123

Bibliography **125**

Vita **132**

Chapter 1

Introduction

Electron scattering is a powerful tool used to study the structure of nuclei. The strength of the electromagnetic interaction between charged particles is quantified by the dimensionless constant, $\alpha \approx 1/137$. The interaction can be expressed as a power series expansion in α, and since $\alpha << 1$, the interaction between charged particles is well represented as single photon exchange. Electrons are an ideal probe of nuclear structure since they are charged point-particles defined by their initial state energy and momentum $(E, \vec{k})$. The resolving power of an electron is related to the momentum transfer idealized as the wavelength of a real photon,

$$\lambda \approx \frac{h}{\sqrt{Q^2}} \tag{1.1}$$

where h is Planck's constant and Q^2 is the four-momentum transfer given in the SLAC convention. The four-momentum is commonly defined in terms of the scattered electron momentum and energy,

$$Q^2 = -q_\mu q^\mu = |\vec{k} - \vec{k'}|^2 - (E - E')^2 \tag{1.2}$$

where the primed quantities are the scattered electron energy and momentum (E', k'). The energy lost by the scatterer is commonly re-written in the form $\nu = E - E'$.

It is worth noting that the electromagnetic coupling constant, α, actually grows logarithmically as the energy scale increases. For momentum transfers relevant for this thesis, ($1\text{GeV}^2 < Q^2 < 6\text{GeV}^2$), the perturbative expansion in α holds.

The kinematic variables ν and Q^2 are sufficient to define kinematic regions of interest. The length scales probed by the scattered electrons depends on their energy and momentum. At low energy transfer, scattering occurs from the entire nucleus in elastic scattering (1.1) or from an excited nuclear resonance state (section 1.2). In nuclei, as both the energy and momentum transfer increase, scattering is dominated by quasi-elastic scattering (section 1.3), where a single proton or neutron (nucleon) in a nucleus is probed. Figure 1.1 illustrates the scattering landscape as a function of ν. To prevent multiple interactions with the electron probe and the target, the time scale is decreased by increasing the momentum transfer. At sufficiently high momentum transfer, scattering from quarks can be achieved, and is well approximated as elastic scattering from a freely moving quark. This type of scattering is known as deep inelastic scattering (DIS), described in section 1.2.

It is clear from the qualitative discussion of scattering above that a relative measure of energy transfer and momentum transfer is useful. The Bjorken scaling variable, x, is introduced as a measure of the momentum transfer relative to the energy transfer,

$$x = \frac{Q^2}{2m\nu} \tag{1.3}$$

where m is the mass of the proton. Bjorken x was originally introduced in deep inelastic scattering (DIS). The physical interpretation of x in DIS is the fractional momentum parallel to $\vec{q}$ by the struck parton in the infinite momentum frame (IMF) [3]. The IMF is the frame in which the elastically scattered electron has the same outgoing momentum as incoming momentum, $\vec{p} = -\vec{p}$; sometimes referred to the Breit frame. Bjorken x has since found use in describing scattering in nuclei. In hydrogen, x can only take the values between 0 and 1, where the latter would mean the struck parton had all the momentum of the proton. In scattering from nuclei, x

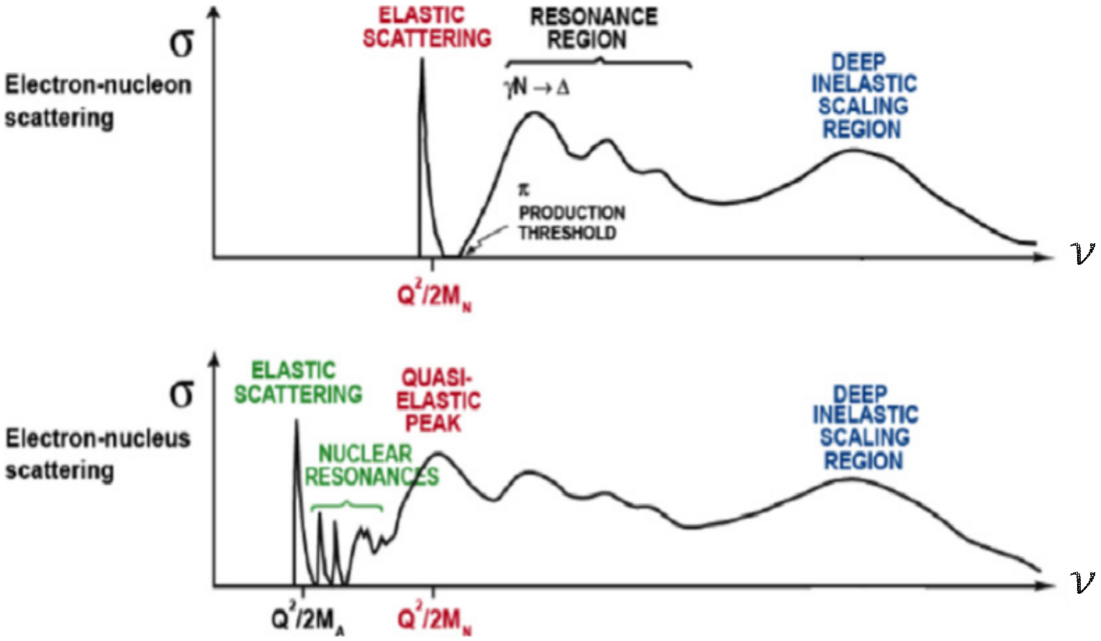


Figure 1.1: Spectra of high-energy electron-nucleon and electron-nucleus scattering as a function of ν. M_N is the proton mass and M_A is the nucleus mass. The contribution from resonances can be minimized by shifting Q^2 away from the resonance mass. Reprinted from [2].

can take values up to $x = A$. Electron scattering with values of $x > 1$ correspond to scattering from objects inside the nucleus that are not accessible to the free nucleon.

To summarize, the electron-photon interaction is well understood, and allows us to use electron scattering is a probe of nuclear structure. Figure 1.1 demonstrates qualitatively that elastic scattering, inelastic scattering, and quasi-elastic scattering, dominate the phase space at different energy and momentum transfers. Sections 1.1 to 1.3 quantify the different scattering regimes. The double differential cross section is introduced in 1.1, which is the observed number of scattered electrons at a given scattered energy and momentum over the solid angle. The primary objective of this thesis is to measure quasi-elastic cross sections from a variety of nuclei to study the high-momentum component of partons in nuclei. Quasi-elastic scattering is described in depth in section 1.3.

1.1 Elastic Scattering

Elastic scattering of charged particles was first carried out by Rutherford, where alpha particles were scattered from gold nuclei. The differential cross section for alpha scattering is given in equation 1.4, where z and Z are the number of protons in the target and beam, α is the electromagnetic coupling constant, E is the incident particle energy, and θ is the angle between the incoming and outgoing electron:

$$\left(\frac{d\sigma}{d\Omega}\right)_R = z^2 Z^2 \alpha^2 \left(\frac{\hbar c}{E}\right)^2 \frac{1}{(1-\cos\theta)^2}. \tag{1.4}$$

While Rutherford scattering was useful for localizing the positive charge to the nucleus of the atom, it can not resolve the underlying structure or distribution of charge in the nucleus. To derive the cross section from the nuclear electric charge distribution, one starts with scattering of point particles off of point targets, namely the Mott cross

section formula:

$$\left(\frac{d\sigma}{d\Omega}\right)_{Mott} = \left(\frac{d\sigma}{d\Omega}\right)_{R} \cdot \frac{1+\cos\theta}{2\left[1+\frac{(1-E\cos\theta)}{Mc^2}\right]}. \tag{1.5}$$

Nucleons and nuclei are not point particles, so the Mott cross section formula cannot agree with the experimental results. The structure of nucleons is included in the cross section by the use of form factors, which are obtained by taking the difference in the measured cross section to the Mott cross section,

$$\frac{\frac{d\sigma}{d\Omega}}{\left(\frac{d\sigma}{d\Omega}\right)_{Mott}} = \frac{G_E^2(Q^2)+\tau G_M^2(Q^2)}{1+\tau} + 2\tau G_M^2(Q^2)\tan^2\frac{\theta}{2}, \tag{1.6}$$

where $\tau = Q^2/4M^2$. The magnetic form factor, $G_M(Q^2)$, and the electric form factor, $G_E(Q^2)$, from equation 1.6 are collectively known as the Sachs form factors. The Sachs form factors are measured for the proton and the neutron (via electron scattering on deuterium), and are related to the Pauli $F_1^N(Q^2)$ and Dirac $F_2^N(Q^2)$ form factors,

$$\begin{aligned} F_1^N &= \frac{1}{1+\tau}\left[G_E^N(Q^2)+\tau G_M^N(Q^2)\right] \\ F_2^N &= \frac{1}{1+\tau}\left[[G_M^N(Q^2)-\tau G_E^N(Q^2)\right] \end{aligned} \tag{1.7}$$

where N = p,n for proton or neutron. The nuclear magnetic moment, charge distribution, and charge radius can be extracted from the form factors.

The low-momentum and low energy transfer region is dominated by the elastic scattering cross section. In this experiment, elastic scattering is performed to check the spectrometer performance. Any difference between the measured elastic scattering cross section and world data on elastic scattering signals an issue with the detector calibration. Further details are presented in section 3.3.1.

When electrons scatter elastically from hydrogen, the outgoing electron energy and momentum will be proportional to the proton mass. The invariant mass of the

proton is reconstructed from the scattered electron energy and momentum as,

$$W^2 = 2m_p\nu + m_p^2 - Q^2 \tag{1.8}$$

where m_p is the mass of the proton. From figure 1.1, elastic scattering is separated from the quasi-elastic scattering in ν relevant in this experiment. Inelastic scattering, however, is a competing process for quasi-elastic scattering. In order to extract the quasi-elastic cross section, the inelastic cross section must be fully constrained.

1.2 Inelastic Scattering and Nucleon Resonances

In inelastic scattering, momentum and energy are transferred from the electron to the nucleus. This process commonly results in the breakup of a nucleon, illustrated in figure 1.2. At high Q^2, the form factors F_1 and F_2 become independent of Q^2. In other words, the structure functions are left unchanged by a scale transformation, $Q^2 \to \kappa Q^2$. The implication of this observation is that nucleons are composed of point particles. Scattering in this regime is known as deep inelastic scattering (DIS). The cross section can be written in terms of two new structure functions, W_1 and W_2,

$$\begin{aligned} 2MW_1(\nu, Q^2) &= F_1(x, Q^2) \\ \nu W_2(\nu, Q^2) &= F_2(x, Q^2) \end{aligned} \tag{1.9}$$

where ν has been replaced with Bjorken-x. This is known as Bjorken scaling. Scattering from the point particles (now known to be quarks), is the dominant process that competes with quasi-elastic scattering. DIS dominates the phase space, $Q^2 > 1$ GeV and $W > 2$ GeV. Figure 1.3 shows scaling behaviour in F_2^p for $0.1 < x < 0.4$ versus Q^2. The DIS structure functions F_1 and F_2 can be reduced further by the Callan-Gross relation $F_2(x) = 2xF_1(x)$[5]. The Callan-Gross relation provided further evidence that the point particles in the nucleus are spin-1/2, fitting the quark model. This is based on the interpretation of structure functions as linear combinations of

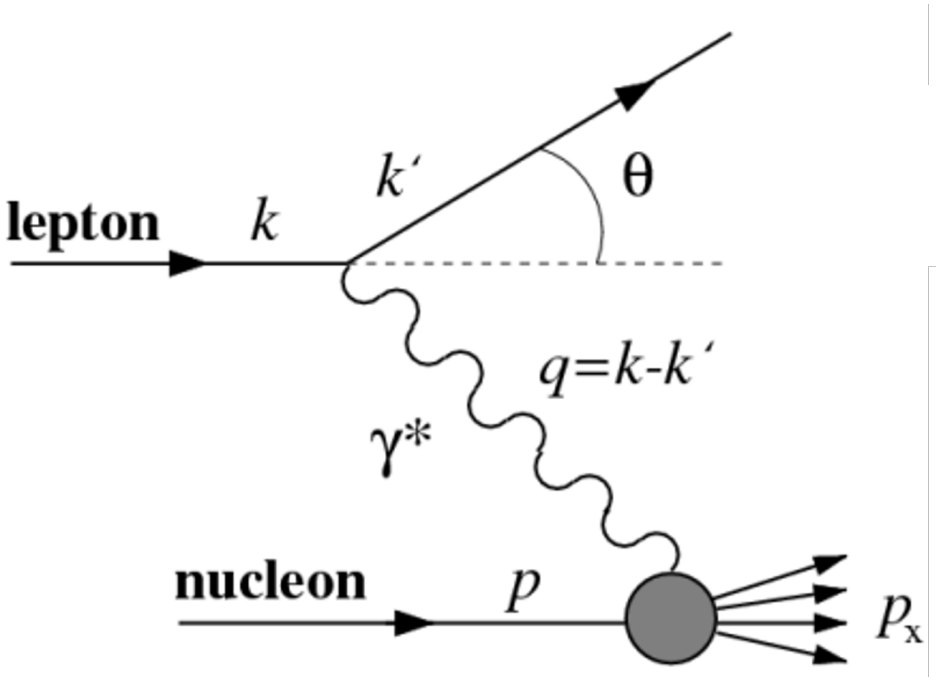


Figure 1.2: Lepton scattering from a nucleon under the single photon approximation. The electron-photon vertex is well understood, leaving the nucleonic degrees of freedom as the only unknowns.

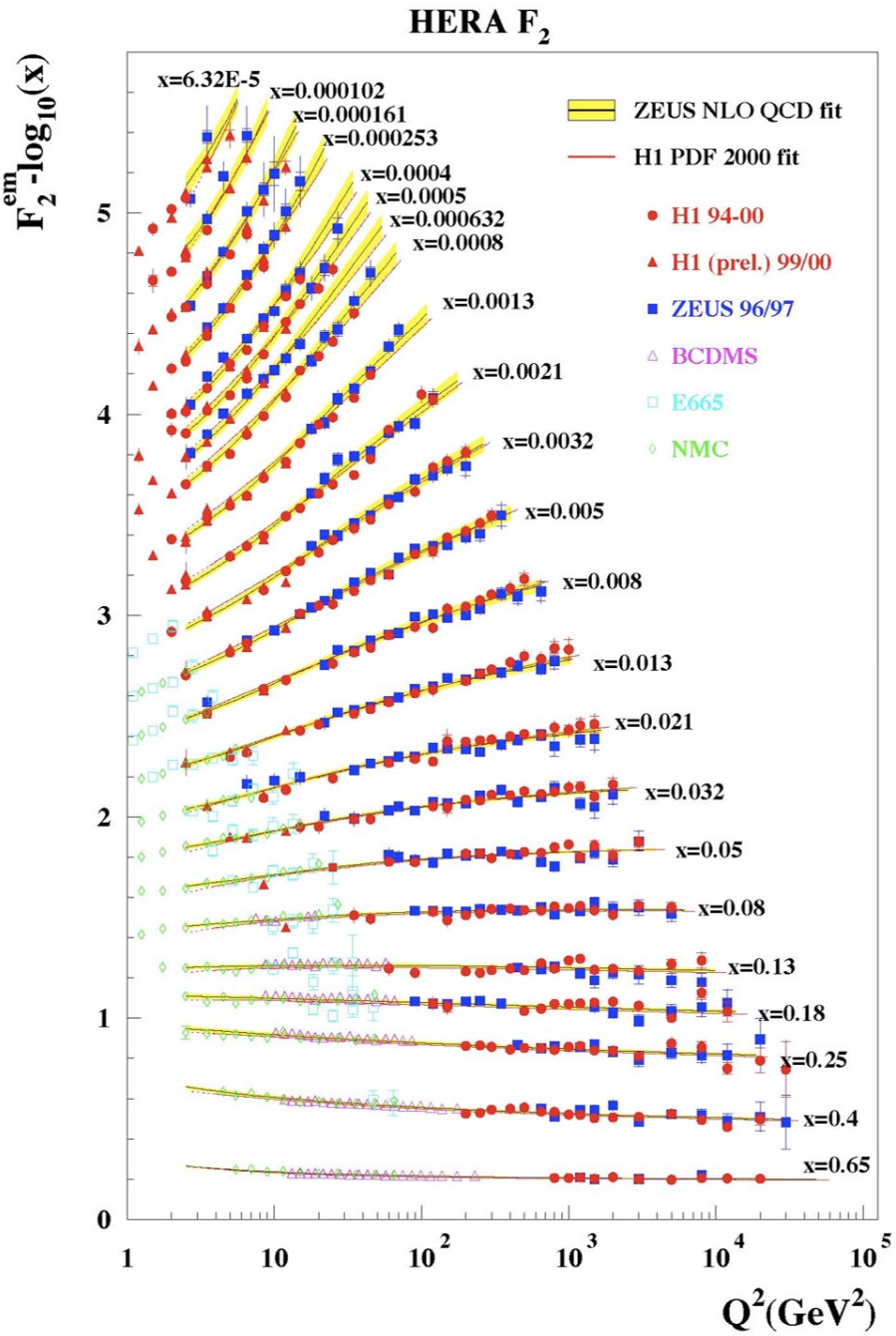


Figure 1.3: The F_2 structure function of the proton as a function of Q^2 at different values of x. The data is from fixed target electron scattering experiments as well as positron and muon experiments. As x increases, the structure function no longer depends on Q^2; this is known as Bjorken scaling[4].

quark distribution functions.

Contributions from resonant states appear in inelastic scattering regimes and resonant peaks have the potential to overlap with the quasi-elastic peak[6]. Resonances are excited states of nucleons with invariant masses ranging from about 1 GeV to 2 GeV. The inclusive resonant photocouplings of most excited nucleon states in the mass range up to 2 GeV have been well determined [6]. The Q^2 for this experiment has been tuned to minimize the contributions from resonances near the quasielastic peak.

1.3 Quasi-Elastic Scattering

Quasi-elastic scattering is a process in which a single nucleon is knocked out of the nucleus by an electron. Both the knocked out nucleon and scattered electron can be measured (exclusive), or just the scattered electron can be measured (inclusive). Figure 1.4 illustrates the Feynman diagram for quasi-elastic electron scattering. Quasi-elastic scattering is dominant in the regime, 0.5 GeV $< Q^2 <$ 2 GeV. The quasi-elastic peak occurs at $x = 1$, and the peak is broadened due to the motion of nucleons in the nucleus. Quasi-elastic scattering is commonly treated in the impulse approximation, where no secondary interactions with the nucleus occurs. The cross section for quasi-elastic scattering can be written as[7, 8]:

$$\frac{d^2\sigma}{dE_{e'}d\Omega_{e'}} = \sum_1^A \int d\vec{p_o} \int dE_s \cdot \sigma_{ei} \cdot S_i(p_o, E_s) \times \delta(\nu + M_A - \sqrt{M^2 + p'^2} - \sqrt{M_{A-1}^{*2} + p_o^2}), \tag{1.10}$$

where $\vec{p_o}$ and $\vec{p'} = \vec{p_o} + \vec{q}$ are the initial and final state momentum, E_s is the separation energy, and δ is the energy and momentum conservation term. The sum over i is for all protons and neutrons σ_{ei} are the electron-nucleon cross sections from bound nucleon states. The spectral function $S_i(p_o, E_s)$ describes the probability of finding a nucleon with a certain energy and momentum. M_A is the initial nucleus mass, M^*_{A-1} is the mass of the residual (A-1) system, and M is the mass of the nucleon.

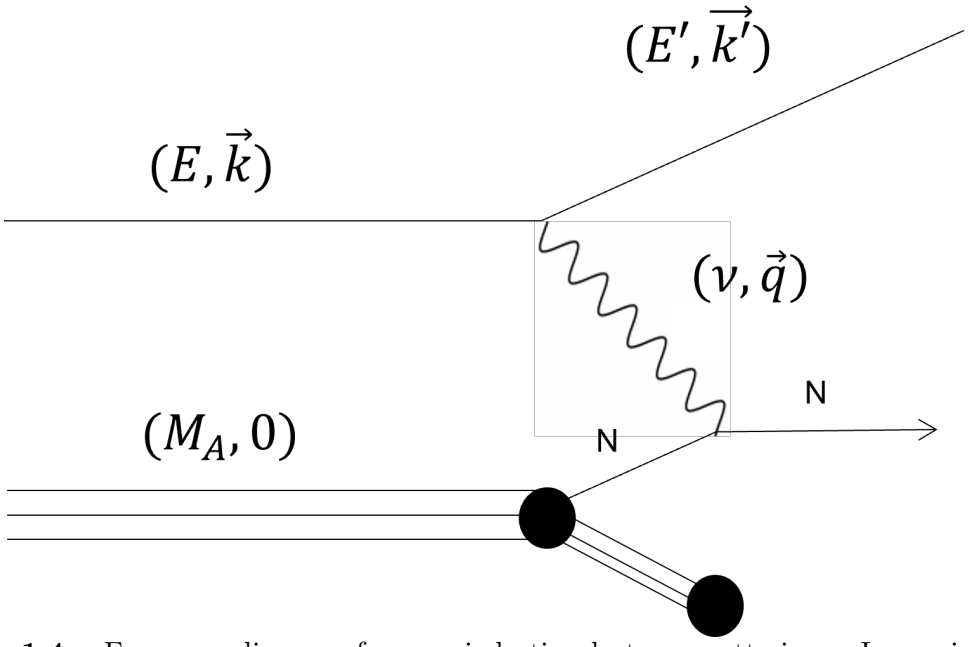


Figure 1.4: Feynman diagram for quasi-elastic electron scattering. In an inclusive measurement, only the scattered electron final state (E', k') is measured. In an exclusive measurement, both the scattered electron and knock-out proton are measured. Typical quasi-elastic scattering occurs at $Q^2 \geq 1\,\mathrm{GeV}^2$.

The impulse approximation breaks down at the lowest momentum transfers $Q^2 \approx$ 0.5 GeV as multiple interactions with the nucleus begin to occur. Final state interactions (FSIs) are any secondary interaction the observed particles have with the nucleus that causes a change in energy or momentum. It has been shown that at sufficiently high Q^2, the hadronic FSIs vanish [9, 10]. The long range Coulomb final state interactions do not vanish and are parameterized separately as coulomb corrections in section 4.3.1. For this experiment, the momentum transfer is always greater than $2GeV$, so FSIs are safely neglected.

Scaling occurs when a cross section becomes independent of the usual kinematic variables, Q^2 and ν and takes on a new form, described in 1.2. The power of scaling is that it often implies a single dominant process, and information on that process can be extracted in a model-independent way[11]. Scaling has also been demonstrated in inclusive short range correlation (SRC) measurements, which are demonstrated in section 5.2.

1.4 Background on Short Range Correlations

Many properties of nuclei, including magic numbers, angular momentum, parity, and spin can be described using the nuclear shell model. This model is strikingly similar to the atomic shell model used for atomic electrons. However, not all properties of nuclei can be explained under this model. High energy electron scattering experiments performed in the 1980s showed that a large fraction of nucleons occupied states with higher momentum and energy than predicted under the independent particle shell model (IPSM). One possible explanation for the energetic nucleons observed in nuclei are the contributions from 2-body interactions between nucleons at short distances. The term short range correlation (SRC) is used to describe the pair of nucleons interacting at close range in nuclei. These pairs are characterized by high back-to-back momentum, and low center-of-mass momentum. This property, and many other properties of SRCs have been observed experimentally, and are outlined in this

section. The background information covered in this section supports the observation of SRCs, and motivates further study on the properties of SRCs.

1.4.1 Independent Particle Shell Model

As early as the 1940s, atoms were known to be composed of nucleons, and the nucleons were known to be spin-1/2 particles (fermions). The Hamiltonian for the many-body problem can be written in terms of n-body operators [12],

$$H = T + \sum_{i<j}^{A} V_2(i,j) + \sum_{i<k<j}^{A} V_3(i,j,k) + ... \tag{1.11}$$

where V_2 and V_3 are 2-body and 3-body operators respectively. The independent particle shell model (IPSM) was developed to model the interaction between nucleons as an effective potential. Under the IPSM, the nucleons occupy well defined shells (quantum orbits) in an average potential (V_m) and there are no interaction between particles:

$$H = T + V_m. \tag{1.12}$$

The effective potential in the IPSM includes two terms, motivated by experimental observations. The potential is given as a Woods-Saxon potential, and a spin-orbit interaction,

$$V_m = \underbrace{\frac{-U_o}{\exp\left(\frac{r-R_o}{a}\right)+1}}_{\text{Woods-Saxon Potential}} + \underbrace{\left[U_{ls}(r)\vec{L}\cdot\vec{S}\right]}_{\text{Spin-orbit intxn.}} \tag{1.13}$$

where $U_o \approx 50\text{MeV}$, $a \approx 0.5\text{fm}$, $R \approx 1.25A^{1/3\text{fm}}$[12].

Neutrons and protons have separate potentials where the proton potential has an additional Coulomb component. Figure 1.5 illustrates the filling of IPSM states for neutrons and protons for ^{116}Sn[13]. The highest energy of nucleons in the nucleus is called the fermi energy, which corresponds to the highest momentum state a ground state nucleon may have, called the fermi momentum. The success of the IPSM is

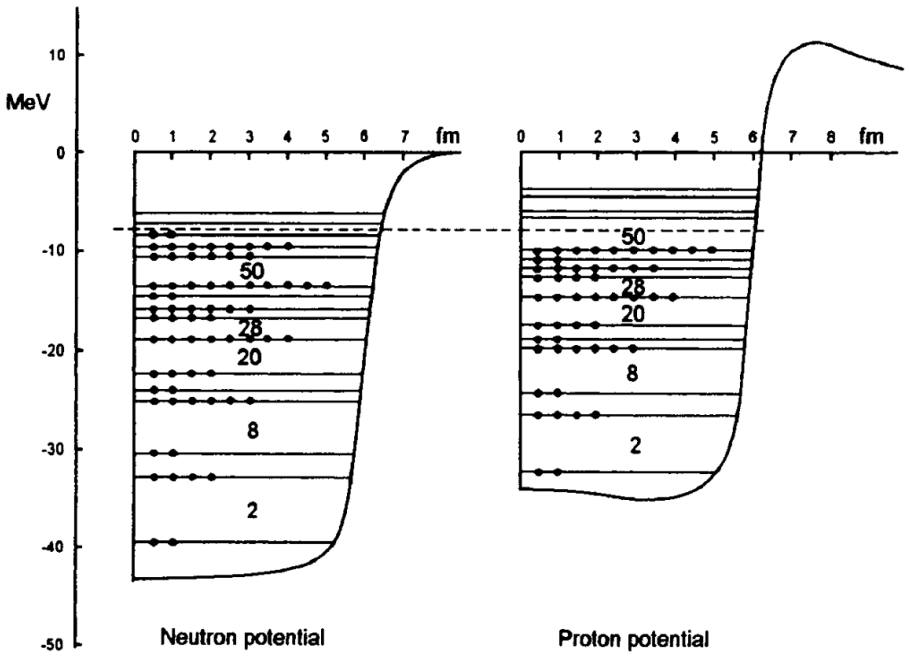


Figure 1.5: The separate neutron (left) and proton(right) potentials filled up to the fermi energy. The proton potential has a long range Coulomb component. Closes shells are enumerated and shows as gaps in energy levels. Figure reprinted from [13].

very impressive given the simple assumptions used, and further detail is expounded in [14]. Limitations of the model were subsequently determined in exclusive experiments, where a coincident proton is observed with a scattered electron.

1.4.2 Exclusive Measurements and Shell Occupancy

Exclusive quasi-elastic proton knock-out cross sections have been measured[15], and spectral functions, $S(p, E)$, have been extracted from data. Exclusive experiments put tight constraints on the momentum and energy of the knocked out nucleon from the nucleus. The extracted spectral functions are compared to predictions under IPSM. Spectral functions under IPSM are expanded in a basis of single particle wave functions and energies,

$$S(E, p) = \sum_i |\Phi_i(p)|^2 \delta(E + \epsilon_i). \tag{1.14}$$

The $\delta(E + \epsilon_i)$ comes from the conservation of energy and momentum for each state. By integrating over the different energy states of the spectral function extracted using the IPSM model, the momentum distribution can be obtained:

$$n(p) = \int S(E, p) dE. \tag{1.15}$$

From the momentum distirbution, $n(p)$, the occupancy of specific shells in IPSM[16]. The number of knocked out protons in specific shells was found experimentally to differ from the predicted number from shell occupancy under the IPSM[15]. This result led to experiments devoted to studying occupancy across many different nuclei. In these experiments, a depletion of valence orbits of approximately 65% were observed across all nuclei studied. Additionally, an abundance of nucleons were observed with momentum higher than the fermi momentum[17]. These observations are summarized in figure 1.6. Exclusive quasi-elastic scattering experiments in the 1980s showed that scattering from single particle states above the fermi momentum

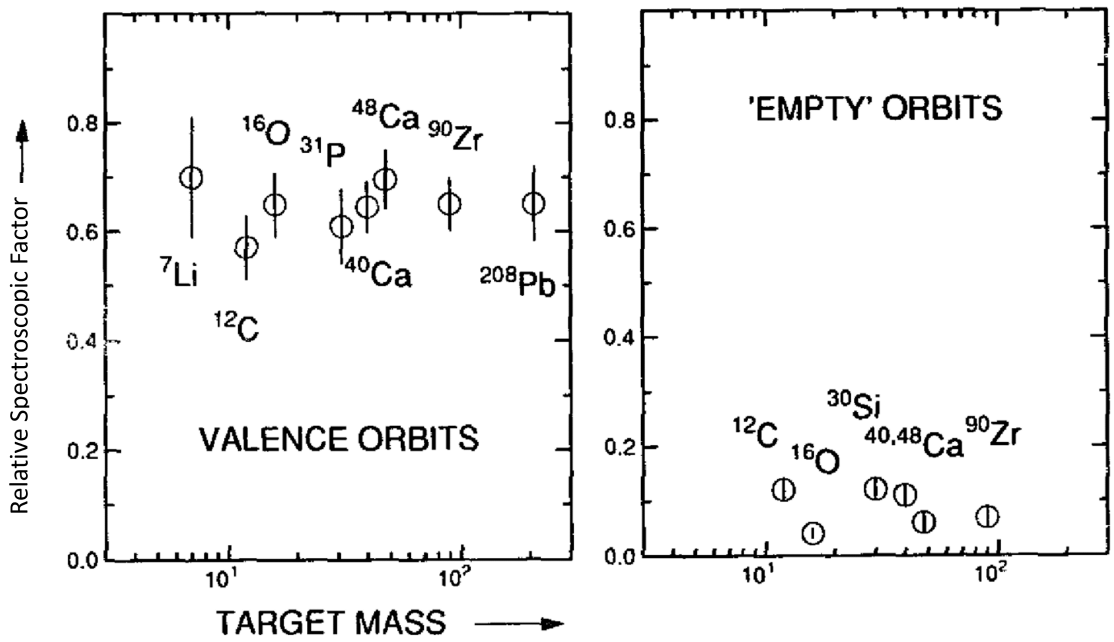


Figure 1.6: Left: Spectroscopic factor for valance shell levels from $A(e, e'p)$ reactions. A nearly constant depletion of levels of $\approx$ 65% is observed relative to IPSM. Right: Enhancement of spectroscopic factor just above the valence shell[17].

was possible. The observed depletion of nucleons in valence orbitals relative to empty orbitals can be explained by two-body short range correlations in nuclei[18], described in 1.4.3. Exclusive quasi-elastic experiments demonstrated high momentum nucleons are a universal component of nuclei. In inclusive quasi-elastic scattering experiments, the scattered electron momentum and energy are constrained to scatter from high momentum nucleons in the nucleus.

1.4.3 Short Distance Nucleon-Nucleon Interaction

The two-body interaction can be modeled by adding a nucleon-nucleon potential to the Hamiltonian of the IPSM. Nucleon-nucleon interaction models come as either phenomenological models or ab initio models, such as chiral effective field theory (χ^{EFT}). At present, AV18[19] (a phenominological model), has the best agreement with $A(e,e'p)$ and $A(e,e'pp)$ measurements [20]. Figure 1.7 shows the central component of three modern phenomenological models of NN interaction.

SRCs can be characterized by short-range repulsion and contributions of intermediate and long range tensor character[24]. The tensor component of the NN potential is comprised of a scalar isospin component and a vector spin-spin component that increases as the distance between nucleons decreases:

$$V_T = (\tau_1 \cdot \tau_2) S_{12} V(r). \tag{1.16}$$

τ_1 and τ_2 are the isospin component of nucleon 1 and 2, S_{12} is the spin-spin interaction term, and $V(r)$ is the radial dependence of the tensor force, see figure 1.8 . Isospin is a measure of the relative up and down quark content of nucleons. The possible isospin combinations of a proton and neutron are 0 and 1.

Neutron-proton pairs (np), proton-proton (pp) pairs, and neutron-neutron (nn) pairs can be formed. Measurements from the $^{12}C(e,e'pn)$ and $^{12}C(e,e'pp)$ reactions indicate a dominance of np pairs over pp pairs[25]. This is an indication of the tensor nature of the NN interaction. These experiments show that Carbon is composed of

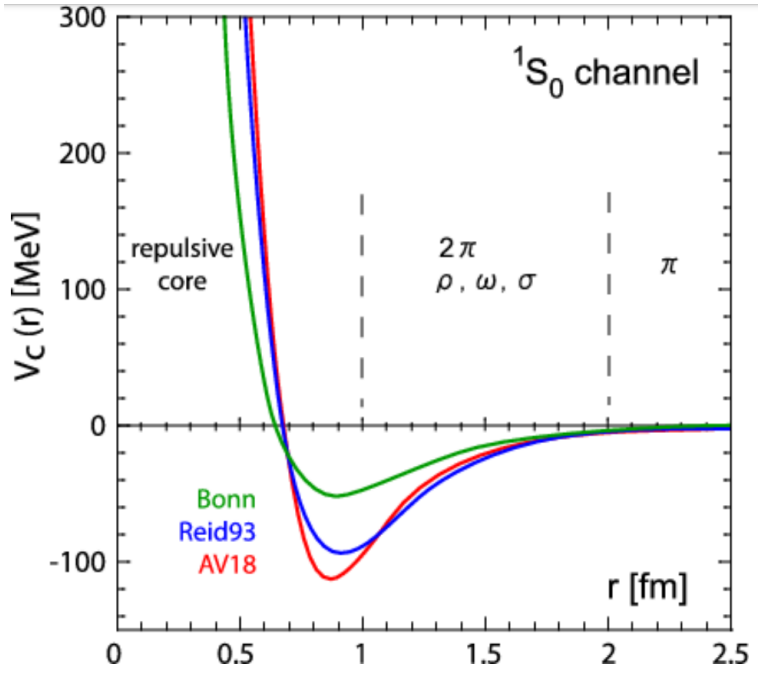


Figure 1.7: The central component of three modern NN potentials in the $^1S_0$ (spin singlet and s-wave) channel: CD Bonn[21], Reid93 [22], and AV18[19]. Reprinted from [23].

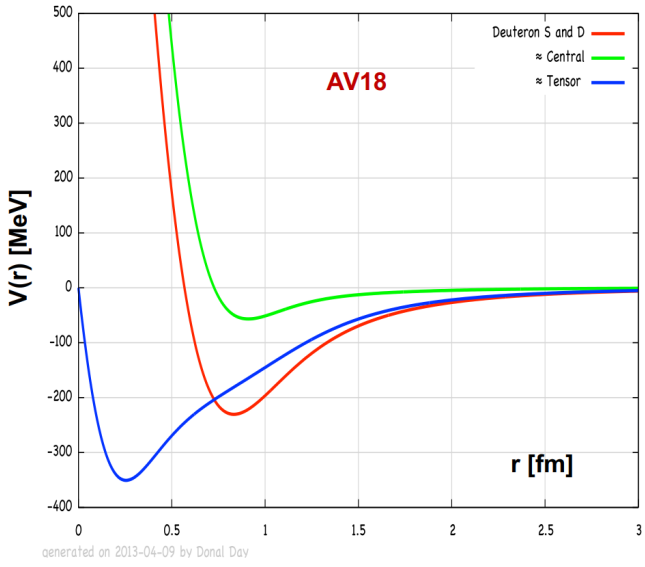


Figure 1.8: Tensor and Central component of the NN potential from AV18. Plot generated courtesy of Donal Day[7].

about 80% IPSM nucleons and 20% SRC pairs, where the SRC pairs are composed of about 90% np pairs, and 5% pp and 5% nn pairs[26]. Figure 1.9 shows the breakdown of ^{12}C and the associated errors with the measurements.

The repulsive core of the NN potential between nucleons drives the formation of SRCs. The SRCs are characterized by high relative momentum, but low center-of-mass momentum. The momentum distribution of IPSM is compared to the momentum distribution generated by AV18. In the case of AV18, the phenomenological model is built out of hard interactions between nucleons. Hard interactions are those that involve particles with a large amount of kinetic energy. The AV18 potential, shown in figure 1.7, is deeper compared to CD Bonn[21] and Reid93 [22] is which is a signature of the hard interactions the model was parameterized to. AV18 generates momentum distributions with a high momentum component, as seen in figure 1.10. The success of AV18 in modeling the SRC momentum distribution is determined by the interactions used to build the model. In the era of high-precision SRC measurements, it is important to move past phenomenological models to understand what drives SRCs in nuclei.

χ^{EFT} NN potentials have been calculated up to next-to-next-to-leading-order (N^2LO)[28], with the possibility of future improvement over AV18. The present χ^{EFT} calculations have explicit cut offs at distances of 1.0 fm and 1.2 fm, which corresponds to a momentum cutoff of about (400-500 MeV/c)[29], which limits the predictive power of these models.

Under similarity re-normalization group theory (SRG), any potential can generate any momentum distribution, but the difference is absorbed in the operators. In AV18, one-body current operators with correlated wave functions are responsible for the high momentum tail. For soft potentials, the high-momentum tail comes from two-body current operators with uncorrelated wave functions[30].

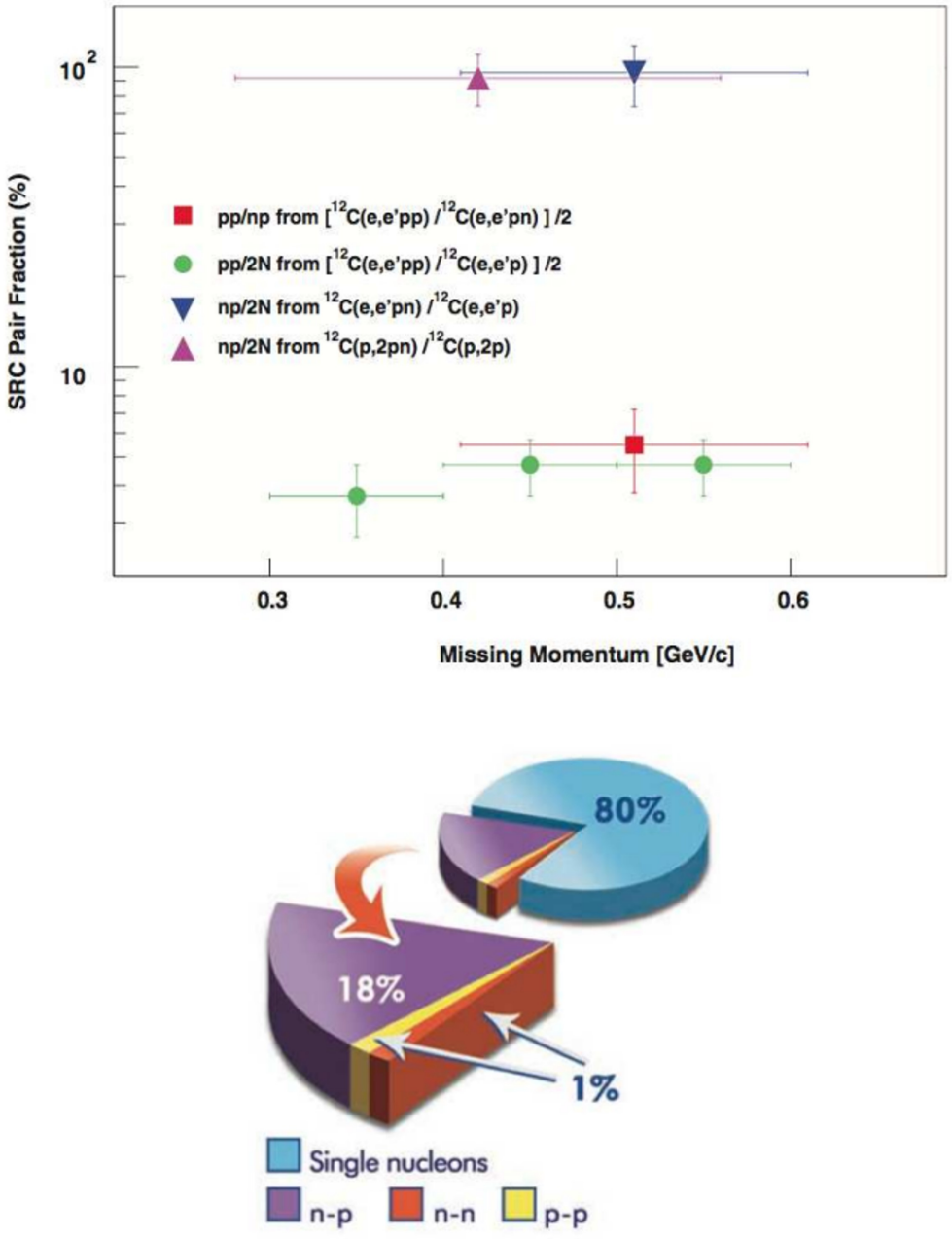


Figure 1.9: Top: A clear np-pair dominance is observed suggesting the importance of the tensor nature of the NN interaction over the specified momentum range. Bottom: Our current understanding of the structure for ^{12}C. Figure modified from [26].

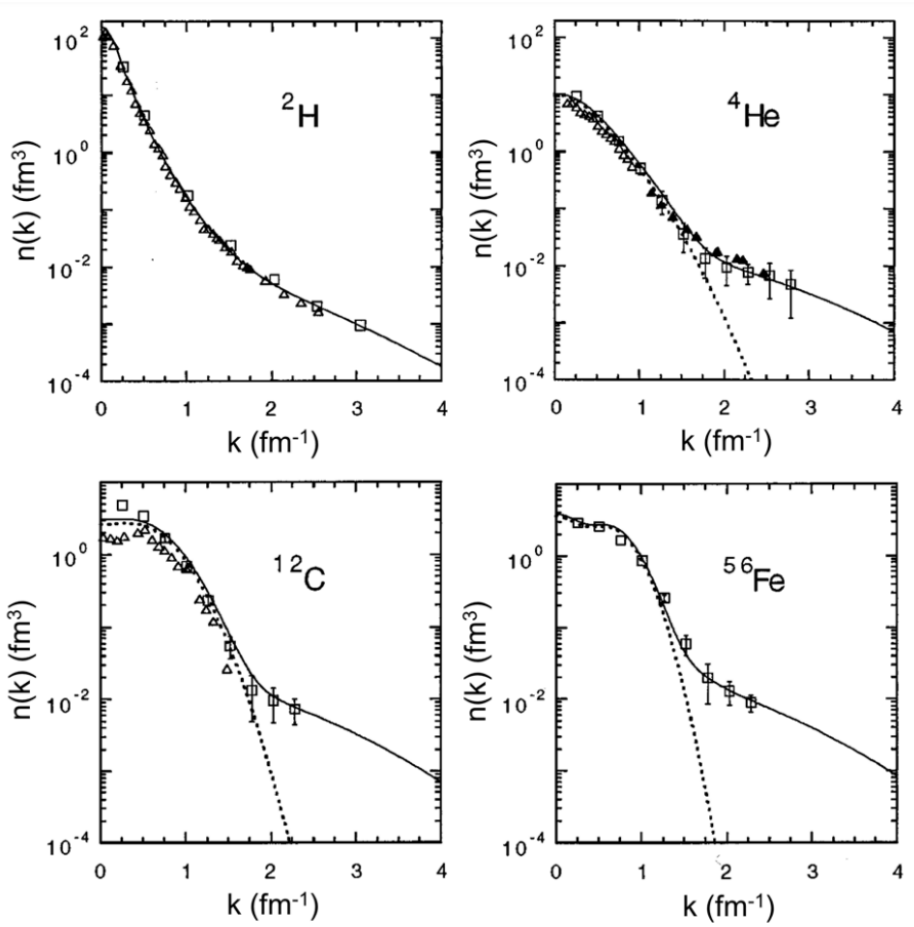


Figure 1.10: From top left to bottom right, momentum distribution for Deuterium, Helium-4, Carbon-12, and Iron. Figure adapted from [27]. Comparison of IPSM momentum distribution (dashed line) to AV18. Symbols are extracted from data using the $F(y)$ scaling model, detailed in 4.3.

1.4.4 Short Range Correlations

Scattering from high-momentum nucleons is separated from scattering from low-momentum nucleons by the use of the variable, P_{min}. This kinematic variable is constructed from the energy and momentum conserving delta function in the spectral function observed from exclusive reactions, equation 1.10. Figure 1.11 shows the P_{min} variable as calculated for deuterium.

The inclusive quasi-elastic scattering cross sections are expected to scale at sufficient Q^2 based on the spectral functions obtained in exclusive reactions. This has been shown at SLAC and JLab with 6 GeV beam energies for a wide range of nuclei[31]. Per-nucleon cross-section ratios are the primary observable in inclusive experiments. This is described in detail in section 1.5.

1.5 XEM2 Experiment: E12-06-105

The XEM2 experiment was designed to continue the study of nuclear structure in nuclei using inclusive scattering at $x > 1$. XEM2 was approved by the 2006 JLab Program Advisory Committee (PAC) in the first year 12 GeV proposals were accepted. The energy transfer, ν, was chosen to be as small as possible while increasing Q^2 as high as possible. With these kinematics, scaling in the inclusive quasi-elastic cross-section ratios, is observed. Figure 1.12 illustrates the kinematic coverage for the XEM2 experiment. The angles in figure 1.12 refer to the central angle of the spectrometer, which constrains the kinematics (Q^2 and x). The running period at a central angle of 8° yields 2N SRC measurements on a wider range of targets than ever before, see figure 1.13. At a central angle of 10°, aim to measure 3N SRCs, which is not a part of this thesis. The additional runtime at high Q^2 is designed to make EMC measurements on the same set of nuclei, described in 1.6. These results will be used to investigate the relation between the EMC effect and SRCs, described in 1.6.

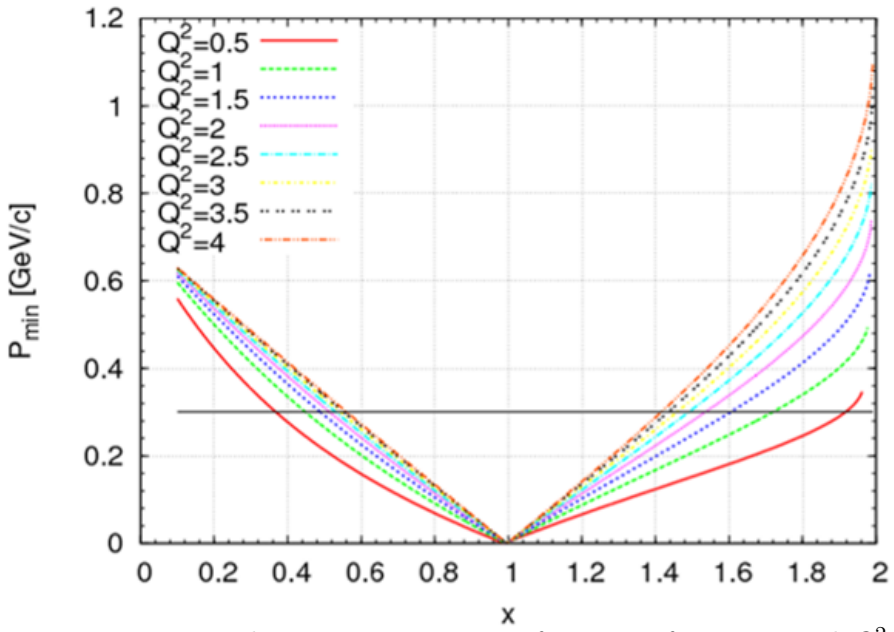


Figure 1.11: Minimum nucleon momentum as a function of x at several Q^2 values for deuterium. The black line corresponds to a momentum of 300 MeV/c, over which scaling is observed. The Q^2 must be sufficiently high in order to see a plateau in the cross section ratios relative to deuterium.

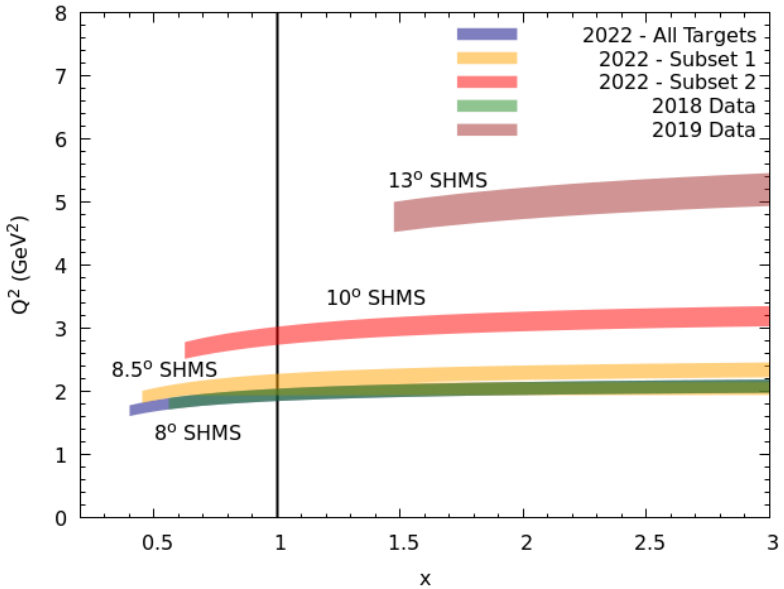


Figure 1.12: The kinematic coverage in Q^2 vs x for several central angles of the SHMS. Several data taking periods are shown, with the focus of this thesis on the 2018 and 2019 data.

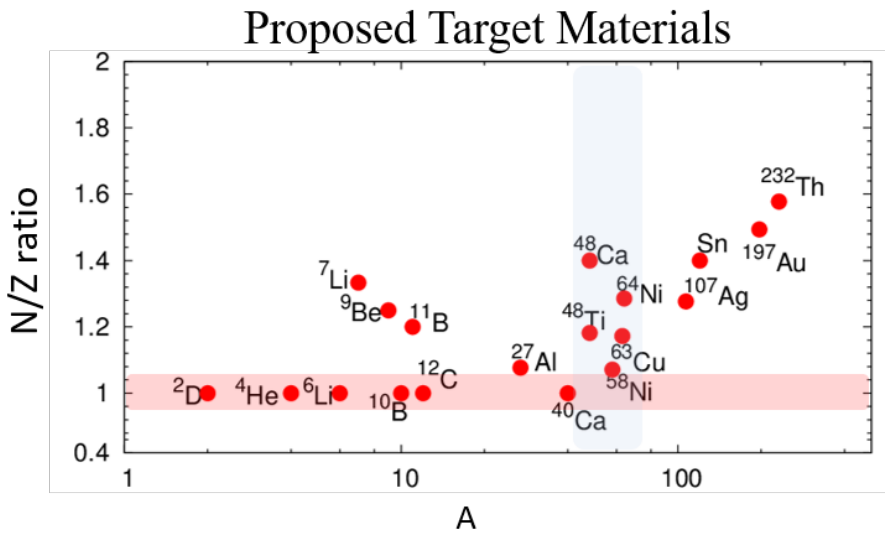


Figure 1.13: Largest set of nuclei to be measured at $x > 1$. Nuclei were chosen to for study of np-pair dominance and nuclear dependence in light nuclei[9].

The cross section at low ν decreases rapidly as the momentum transfer increases, necessitating a high luminosity machine. Inclusive scattering at $x > 1$ has previously been measured at several different energy transfers and has confirmed scaling of the inclusive quasi-elastic cross sections for nuclei. Figure 1.14 shows the double differential cross sections per-nucleon for ^3He, ^4He, ^9Be, ^{12}C, ^{63}Cu, and ^{197}Au relative to deuterium. A plateau is observed in figure 1.14 above $x \approx 1.4$. The scaling observed in the quasi-elastic cross section binned in x suggests the isolation of scattering from nucleons arising from 2N SRCs. This hallmark observation is characterized by the best fit to the plateau, namely a_2. The characteristic rise in $x \approx 1.95$ is due to the kinematic limits on deuterium[31].

XEM2 ran in the fall of 2022 at Thomas Jefferson National Accelerator Facility (JLab) in experimental Hall C. There were two commissioning periods, one in spring 2018 and the second in spring 2019. The purpose of the commissioning periods were to characterize the capabilities of the new spectrometer and optimize for the full run of the experiment. A target ladder was constructed to accommodate a large number of targets, described in section 2.3. Focus was placed on light targets that can be directly compared to χ^{EFT} calculations.

1.6 The EMC Effect and SRCs

The EMC effect refers to the observation made in the 1980s by the European Muon Collaboration (EMC) of an anomalous structure function in iron, deuterium, and hydrogen. The measurement was performed taking the ratio of the structure functions of iron, deuterium and hydrogen in deep inelastic scattering[32]. They concluded that the structure of nucleons inside the nucleus differs from the structure of free nucleons. A Rochester-SLAC-MIT group confirmed the EMC results for electron scattering on iron and aluminum shortly after[33]. Many experiments have confirmed the existence of the EMC effect in multiple nuclei, most notably SLAC experiment E139[34], which are shown in figure 1.15. The EMC effect could be the result of SRCs in nuclei.

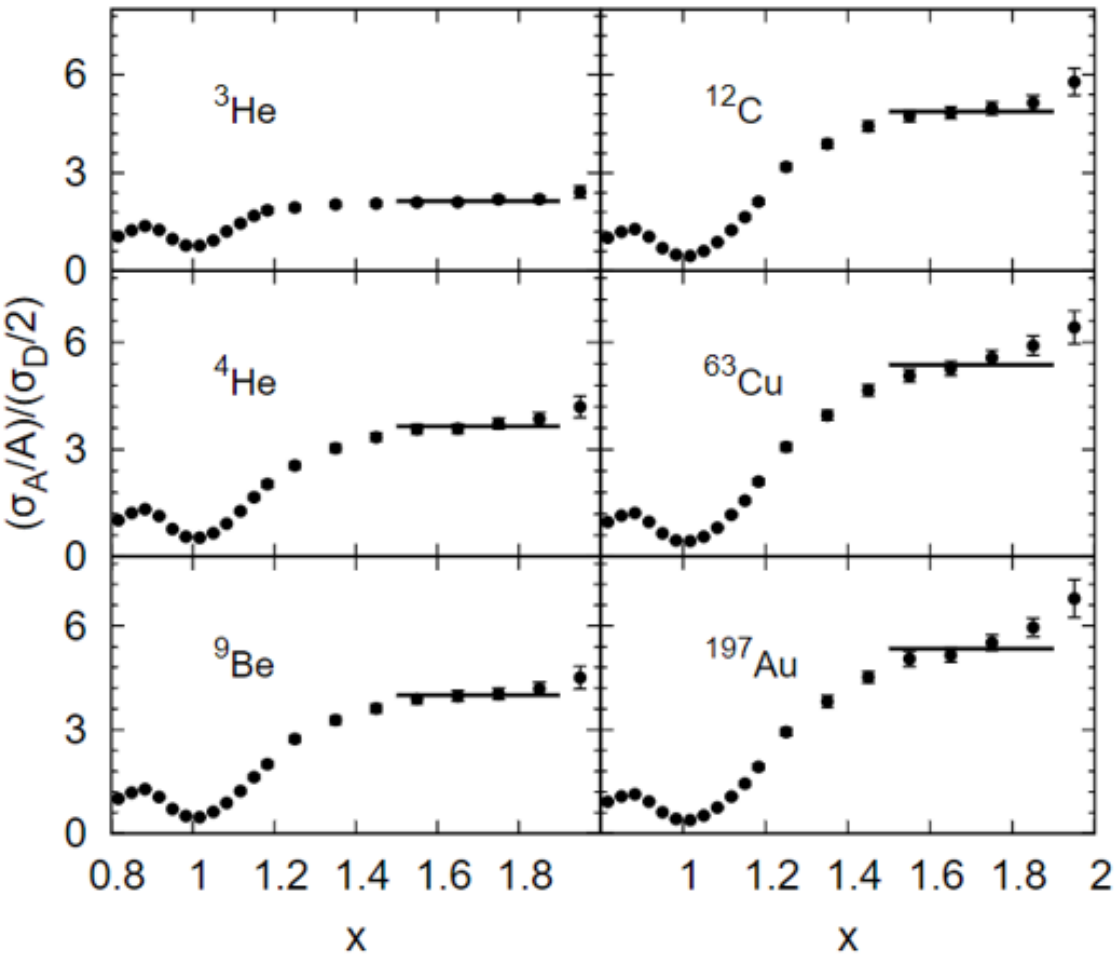


Figure 1.14: Per-nucleon cross section ratios vs x at $\theta_e = 18^\circ$ and 6 GeV from experiment E02-019[31]. The horizontal line is the average in the scaling region, which corresponds to the relative number of high momentum nucleons in a nucleus relative to deuterium[9].

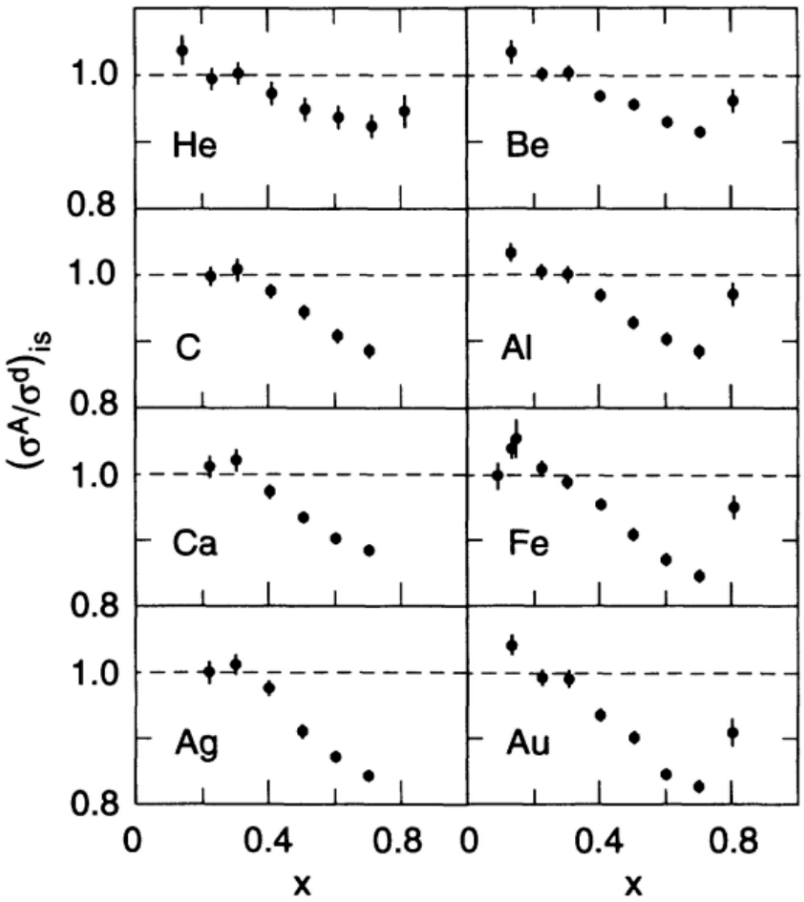


Figure 1.15: EMC results from SLAC experiment E139[34]. A correction has been applied to non iso-scalar nuclei to the cross section ratio, $(\sigma^A/\sigma^d)_{is}$. We see the universal depletion of high momentum nucleons across all measured nuclei.

Nucleons in SRC pairs are greatly modified and there is a non-zero probability the wave functions for nucleons will overlap[18]. The range of the quark confinement would be modified in these SRC pairs and modify the quark momenta. In this case, depletion in the EMC region from $0.3 < x < 0.8$ would display an A dependence. Figure 1.16 shows the EMC-SRC correlation as extracted from world data.

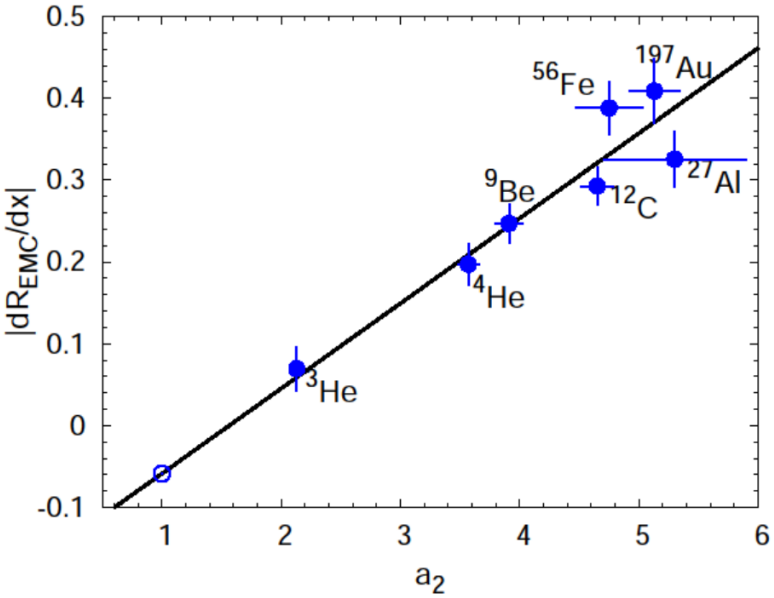


Figure 1.16: The EMC slope is correlated with the number of SRC pairs a_2 for all measured nuclei. Figure provided courtesy of Nadia Fomin for [27].

Chapter 2

Experiment Setup

Experiment E12-06-105, "Inclusive Scattering from Nuclei at $x > 1$ in the quasielastic and deeply inelastic regimes", made use of the Continuous Electron Beam Accelerator Facility (CEBAF) at Thomas Jefferson National Accelerator Facility (Jefferson Lab). Inclusive electron scattering on Deuterium, Carbon, Beryllium, Boron-10 and Boron-11 was performed using a 10.6 GeV incident electron beam and the new Super High Momentum Spectrometer (SHMS) in the spring of 2018 and spring of 2019. These experimental run periods were a part of the larger program to commission the new SHMS spectrometer, which boosted the capability of Hall C to study scattering from an 11 GeV beam. The full experiment was taken in 2022/2023 across 37 PAC days on more targets than can be listed here. We ran in conjunction with our sister experiment E12-10-008. This chapter provides an overview of CEBAF, the Hall C beamline, target ladder, spectrometers and trigger setup.

2.1 CEBAF Accelerator

CEBAF provides a continuous wave (CW) electron beam of up to 12 GeV with amazing beam quality due to small angular spread and very small momentum spread with beam currents up to $70\mu A$. The construction of a CW machine was first proposed in 1976 with the Friedman panel and affirmed at the Livingston panel (1977). A

continuous wave electron beam machine was an upgrade to the pulsed machines of the time because the duty factor could be increased to complete the coincident experiments proposed in a suitable time frame. The high duty cycle of CEBAF is ideal as it minimizes accidental coincidence in exclusive experiments and reduces instantaneous trigger rate in inclusive experiments as compared to lower duty cycle machines of the same average current (i.e. SLAC). CEBAF, originally proposed as a 2 GeV machine, was boosted up to 4 GeV prior to construction to reach higher Q^2. Two further upgrades to CEBAF would increase the energy even higher to 6 GeV and 11 GeV beam to the experimental halls A,B, and C, as well as a 12 GeV beam to a new Hall D. CEBAF has remained relevant with changing nuclear physics demands because the high luminosity it provides, multiple energy upgrades, and the ability to deliver highly polarized electron beam to the experimental halls. The following is a subset of the ongoing experimental nuclear physics program at CEBAF.

- "Determine to what extent nucleons retain their identity in an environment of other nucleons in close proximity" (This experiment)
- Mapping out structure functions for deep inelastic scattering
- Measurement of generalized parton distributions (GPDs) realized in 12 GeV upgrade
- Using parity-violating to probe electroweak interaction

While electrons entering the hall is primarily of interest, it is important to understand the upstream components of CEBAF and their impact on beam quality. CEBAF consists of an injector, two anti-parallel linear accelerators (linacs) connected by 5 re-circulation arcs on either end, a beam switch yard (BSY), a central helium liquefier, and four experimental halls (A, B, C, and D). A top view of CEBAF is illustrated in figure 2.1. The electrons are injected into the north linac from the injector at 123 MeV (already-relativistic)[35]. The electrons are accelerated up to an additional 1090 MeV in the north linac by superconducting radio frequency (SRF) cavities,

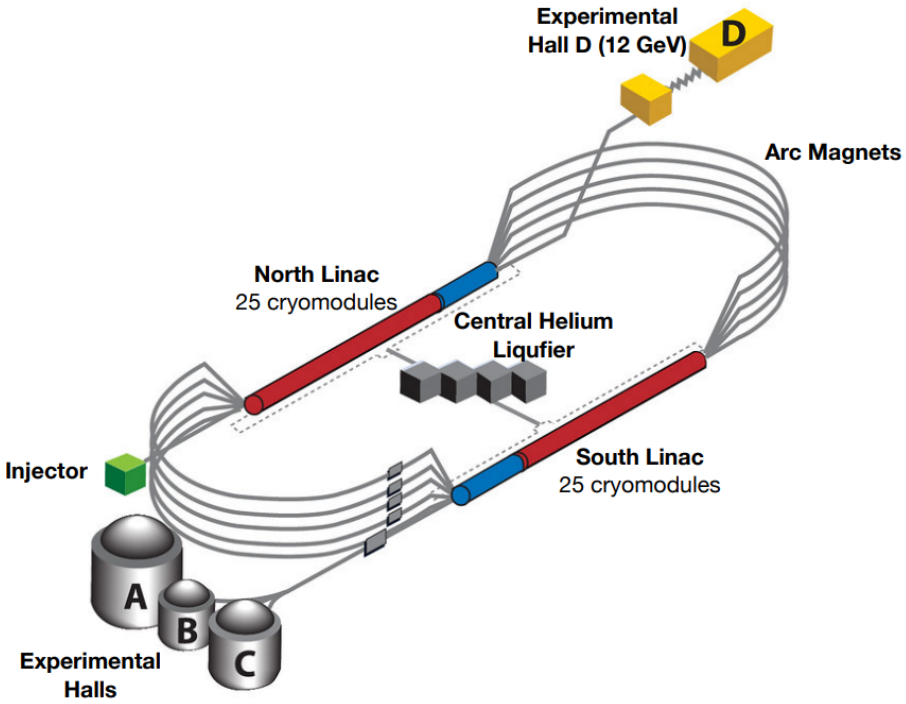


Figure 2.1: Schematic of CEBAF after 12 GeV upgrade. Modified from Ref. [35]. Two anti-parallel linear accelerators are connected by arc magnets tuned to different beam energies. Experimental halls receive 4 passes in each accelerator while Hall D receives an additional pass in the northern linac.

bent through the east arc, and accelerated up to an additional 1090 MeV in the south linac. The electrons can be extracted at the end of any pass through the south linac, providing a beam energy equal to the injector energy plus a multiple of twice the single linac energy. Hall D receives an additional pass through the north linac raising the maximum possible beam energy to 12 GeV. Hall D always get 5.5 pass beam while any one of the other halls can have a lower pass beam at a time. The SRF technology used to accelerate electrons in the linacs use cavities tuned to a frequency of 1497.00 MHz, which is nearly the third harmonic of the fundamental frequency of the cavities. The Central Helium Liquefier (CHL) keeps the cavities at 2 Kelvin in order to maintain superconductivity. The beam has a structure that consists of 1.67 ps pulses coming at 1497 MHz. In order to support 5th pass operation with Hall D, each hall has 249.5 MHz beam. Without Hall D, the other halls can have 499 MHz operation.

2.2 Hall C Beamline

Upon exiting the south linac, the beam is split based on beam bunches in the separator and sent to halls A, B or C in the beam switchyard as depicted in figure 2.1. The hall C arc, located in the beam switchyard, bends the electron beam 34.3° by a series of 8 dipole magnets and 5 smaller deflector magnets as shown in figure 2.2. A straight alcove spans the distance from the shield wall to the hall C entrance and contains various equipment used to steer the beam and measure the position and polarization. Additional beamline diagnostic equipment exists between the hall entrance and the physics target that is mounted on the central pivot of the Hall C spectrometers. The physics target is depicted in figure 2.3 and outlined in the next section. The beam position, current, and energy measurement equipment are critical for counting experiments like ours and each measurements technique is outlined in detail in this section. The downstream beamline and beam dump for electrons are critical for safe operation of the experiment, but have been left out for brevity.

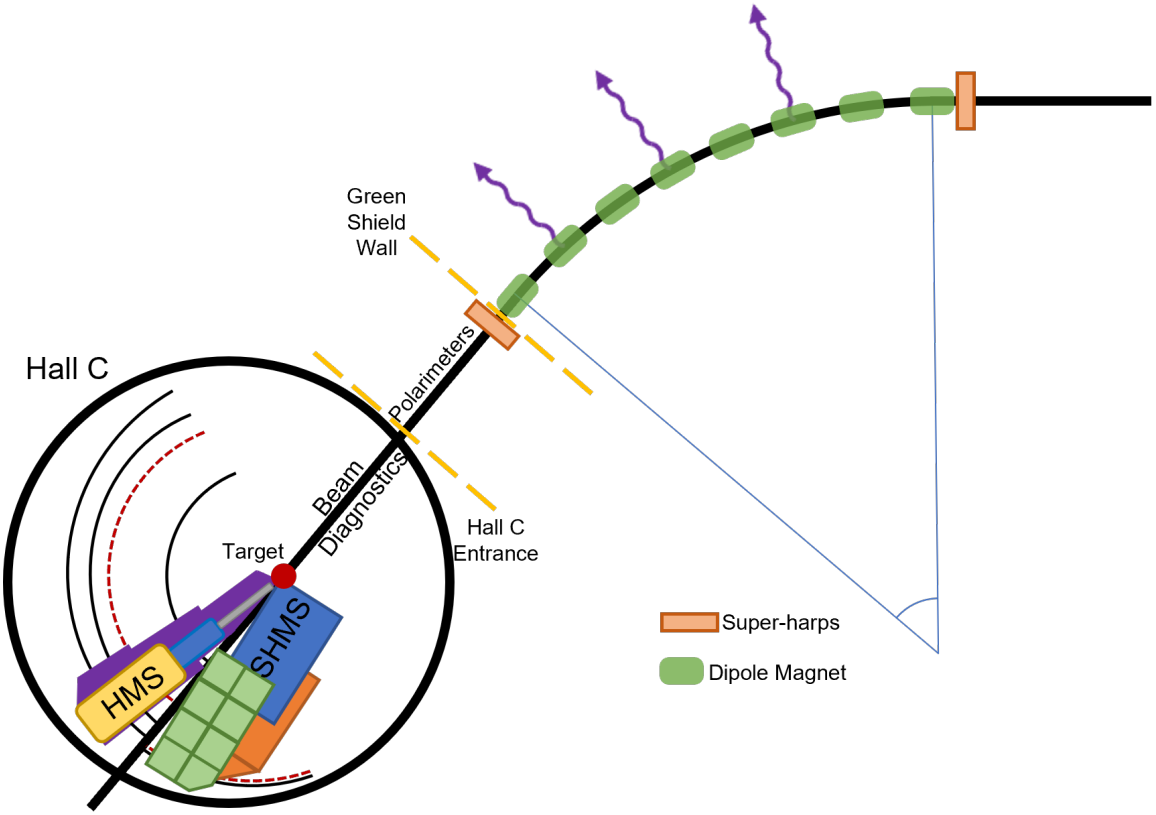


Figure 2.2: Artistic depiction of Hall C arc with the 8 bending dipoles. No deflector or corrector magnets illustrated.

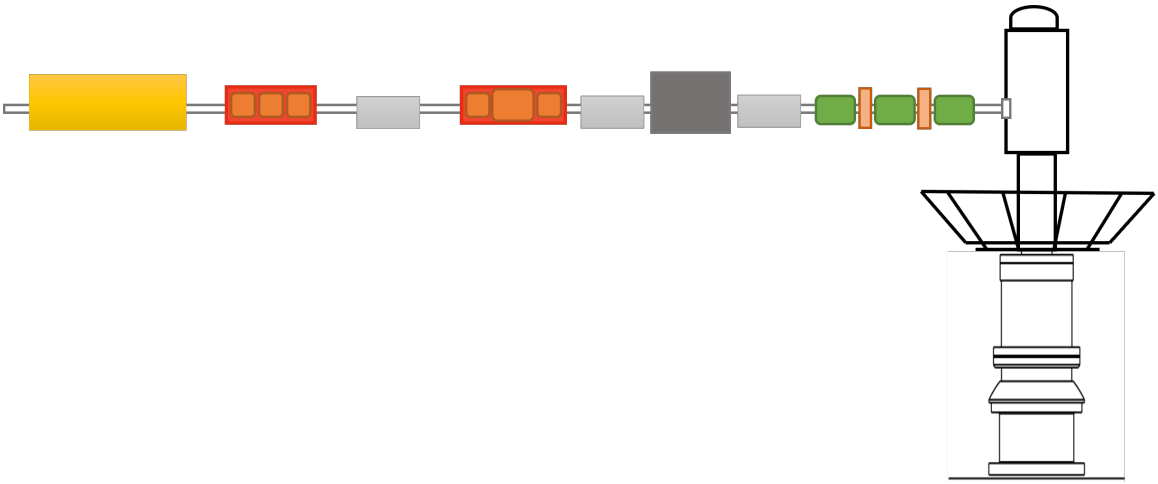


Figure 2.3: Relative position of beam diagnostics to target chamber (right) and hall entrance (left). Møller polarimeter not shown to illustrate beam diagnostics between polarimetery arms. Exit beam pipe and beam dump not shown.

2.2.1 Beam Position and Profile Measurement

The beam position and angle of attack relative to the target must be known in order to determine the number of scatterers encountered by the beam. The Survey and Alignment group determines the absolute position of beamline components including devices known as Harps, which are used to measure the absolute beam position relative to the beamline. The Harps are destructive, so the Harp position is mapped to a set of non-destructive cavity BPMs that actively monitor the beam position. The operating principles of Harps and BPMs are described below. Harps are a series of wires suspended on a fork which is guided into the beam at a 45 degree angle with a stepper motor as shown in figure 2.4. As the wires travel through the beam, secondary electrons are emitted inducing a current in the wire, which is amplified and read out using an ADC. The digitized signal is plotted against the measured beam position as determined by the stepper motor encoder. The normally distributed signal is produced for each wire that passes through the beam, which gives not only the beam position relative to the surveyed components, but also the beam profile. Figure 2.5 shows the results of a typical Harps scan. The absolute position of the beam as measured by the Harps is projected to the cavity BPMs. In this way, the non-destructive cavity BPMs are calibrated and used during production data taking. Cavity BPMs consist of two pairs of antennae oriented at 45 degree angles relative to the vertical and horizontal on opposite sides of the cavity. The beam position is determined by the difference over the sum between opposite antennae. Since this measurement is the difference between two antennae, the beam position measurement is unaffected by beam current. Small non-linear effects in the electronics are taken into account. The beam position on target was kept the same for the entire experiment and systematic effects are outlined in the data analysis chapter. The intrinsic electron beam size of CEBAF is $200 - 700\mu m$ in diameter as determined from the harp scans. The beam profile is typically Gaussian with a full width of $2\sigma \approx 600\mu m$. In nearly all circumstances the beam is rastered to spread out the power dissipated on the target.

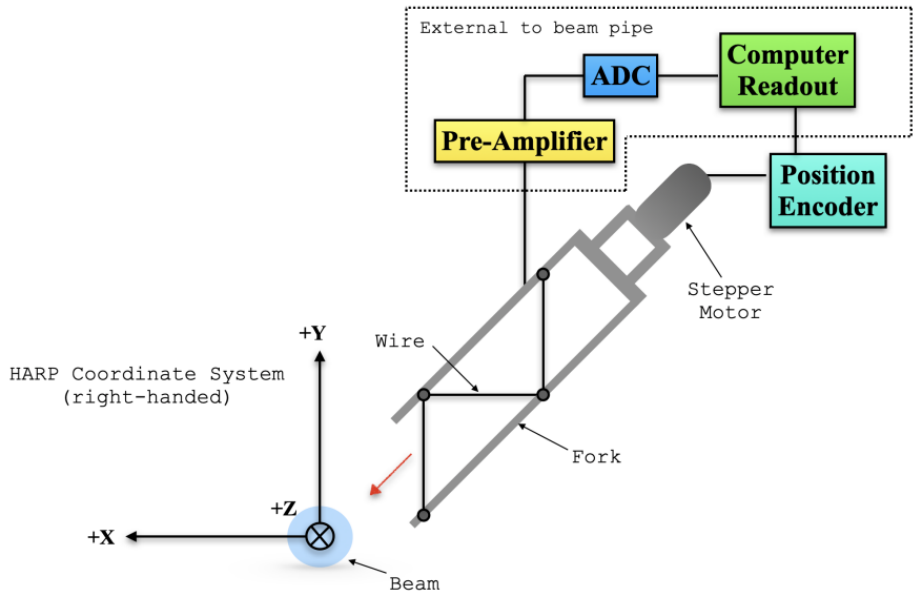


Figure 2.4: A HARP consists of a series of 3 wires held at right angles to one another. The wires are passed through the beam at a 45° angle. Secondary electron emission from the wires is measured by an ADC. The absolute positions and travel of each stepper motor encoder are measured by the Survey and Alignment group at JLab. The machine control center fits the resulting signal and supplies the fit results to each hall as needed. Figure reprinted from reference [36].

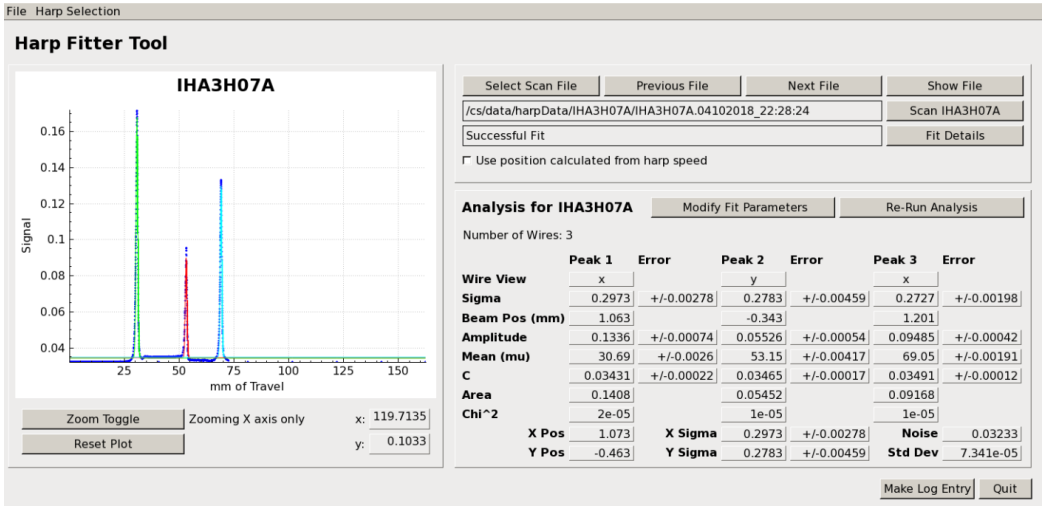


Figure 2.5: Images of the HARP Fitter Tool is provided by MCC. Peaks 1,2, and 3 correspond to the x, y, and x coordinates respectively. A database of absolute position measurements from the Survey and Alignment group are incorporated into the fitting tool, so the X Pos and Y Pos are correct. The instantaneous beam profile is ascertained from the fit to the peak. Reprinted from reference [36].

This is described in the beam raster section. A subset of accurate Harps called super-Harps are used to measure the beam energy. These are effectively regular harps with high accuracy that measure the profile of the dispersed beam as it bends without corrector magnets through the Hall C arc. A pair is at either end of the Hall C arc with a redundant super-harp half-way through the arc.

2.2.2 Beam Energy Measurement

Beam energy measurements are conducted regularly using the Hall C arc as a spectrometer. This technique was first proposed by Yan et al. and has been in use since hall C came online [37]. The hall C arc is 41.6m in length and consists of 8 arc magnets which bend the beam a total of 34.3°. This method uses the equation of motion of charged particles in a magnetic field,

$$|F_e| = e|\vec{v_e} \times \vec{B}| = \frac{\gamma m_e v_e^2}{r_{arc}} \tag{2.1}$$

where e, v_e, B, r_{arc} are elementary charge, electron velocity, magnetic field and arc radius respectively. γ is the lorentz factor. Rearranging equation 2.1, one can solve for electron momentum. The arc length may be expressed as $dL/d\theta$ and integrated across the length of arc. Additionally, the magnetic field must be evaluated at each point along the arc.

$$p_e = C\frac{\int_0^L B_\perp dL_\parallel}{\int_0^{37.5^\circ} d\theta} \tag{2.2}$$

The exact position at the beginning, middle, and end of the arc is measured with superharps as described in [38]. A field map of the dipoles is used in combination with the superharp information to determine the beam energy down to the level of $\delta p/p \approx 2x10^{-4}$ [38]. The beam energy measurement is only performed a few times during the experiment because the corrector magnets in the arc must be deactivated during the measurement. Deactivating the corrector magnets induces a more disperse beam and causes a higher level of downstream radiation damage. Only one magnet

has had its field accurately mapped and the others, being of the same design and construction, are normalized to the central field value. The beam energy obtained from this method does not take into account synchrotron radiation. The synchrotron energy loss is calculated using a simple program, but it is small, order 2-4 keV, when compared to the several GeV beam.

2.2.3 Beam Current Monitors

Precision measurement of the incident electrons on target, is required to obtain precise experimental cross-sections and cross-section ratios. A non-invasive beam current monitor (BCM) is used to sample the instantaneous current, which is integrated over the beam-on time, to obtain charge delivered to the hall. Beam current monitoring is also used to correct for density fluctuations in the target, as discussed later in section 2.3.1. Instantaneous beam current is measured using resonant microwave cavity BCMs. In order to couple the RF power of the beam to the cavity, the dimensions of the cavity are chosen such that they match a multiple of the machine frequency (1497.00 MHz). Changes in temperature can affect the cavity size and decrease the power coupled to the cavity, so the cavities are actively temperature controlled and kept at $110 \pm 0.2°C$. All resonant modes in the cavity dissipate power proportional to the power delivered to the cavity by the beam, and the power of the beam is proportional to beam current. A small wire loop at the edge of the cavity is set up to extract some power from the cavity via the TM_{010} mode as this mode is particularly insensitive to beam position. The resonant cavity BCMs have a relatively stable offset, but the gain can fluctuate throughout the run period. For this reason, the resonant cavity BCMs have their gain calibrated regularly to an Unser BCM, described below. The Unser (Parametric Current Transformer or PCT) is a beam current monitor composed of a series of circular coils arranged in a toroid with a high magnetic permeability. A series of sense coils become magnetized by the beam passing through them, and a magnetic modulator increases the current on a

set of compensation coils to cancel out the magnetic filed at the magnetic modulator. A high dynamic range is achieved with good linearity by combining the magnetic modulator in a feedback loop with a parametric current transformer. While this technique provides a stable gain, it is susceptible to zero-drift when the beam current fluctuates rapidly (i.e. beam turns off). The zero-drift makes the Unser a poor choice for active beam current measurement, but when used in combination with cavity BCMs the highest precision can be achieved. The stable Unser gain is used to calibrate the resonant cavity BCMs, which have relatively stable offsets. During scheduled accelerator downs, the Unser offset is determined with a precision current traveling inside the toroid through a wire. Several times throughout an experiment, a BCM calibration is performed to check the cavity BCM gain against the Unser gain and correct the cavity BCM gain, if required. This is accomplished by turning the beam on for two minute intervals and off for two minute intervals. The Unser gain is measured during beam on conditions and the gain is compared to beam off conditions. This is repeated several times at different currents such that each cavity's gain can be compared to the Unser gain as shown in figure 2.6. Cavity BCMs are not as reliable at low currents because the BCM offset begins to dominate the current read-back. In low-current situations a Faraday cup BCM is used to calibrate the cavity BCMs. No low-current production running was required for the experiment, so no Faraday cup BCM measurements were performed. The output RF signals from the BCMs of 1497 MHz must be down-converted to a lower frequency to be processed by the Hall C electronics. The signals from BCM1 and BCM2 are down-converted to 100kHz via an analog down-converter and the signal is sent to an RMS-to-DC converter with a 20kHz bandpass filter. The signal is then amplified before going through a voltage-to-frequency converter and read out to scalers. The other BCMs (BCM4A, BCM4B, BCM4C) are processed by a digital down-converter with an onboard ADC, FPGA and DAC, which provides an analog signal that can be sent to a V-to-F and finally to the scalers [39]. The nominal 4 mV/μA output signal from the Unser is also sent to a V-to-F before being read out as a scaler. All signals are also read out to EPICS using

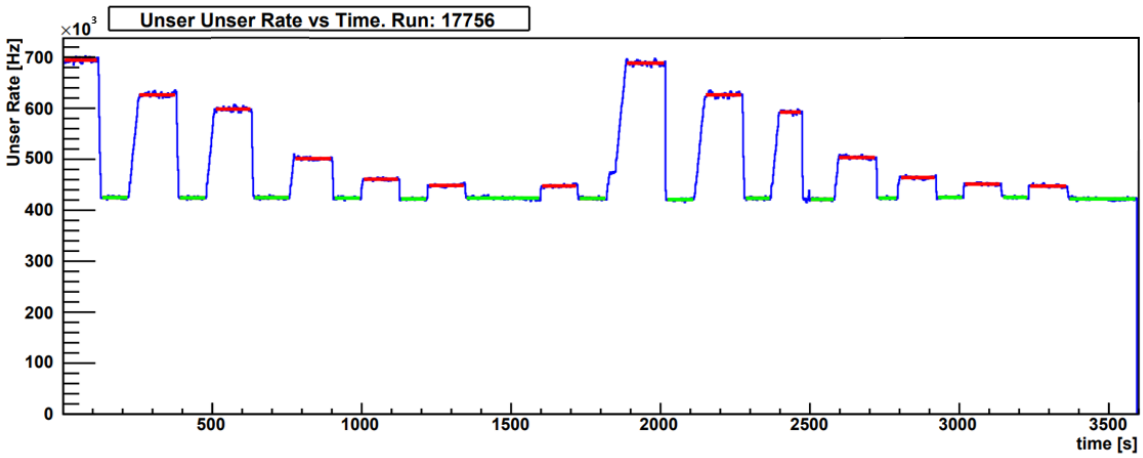


Figure 2.6: BCM Calibration run consisting of alternating periods of beam on and off with increasing current during each beam on period.

an EPICS controller located in the Hall C Counting Room. Additional information on the data stream, including a description of EPICS events, is detailed in section 2.6. Figure 2.7 illustrates the readout electronics.

2.2.4 Beam Raster

In Hall A and C, beam currents of up to $70\mu A$ can be reached. The Gaussian beam profile has an intrinsic size of $200 - 700\mu m$ FWHM for 12GeV operation[40]. The power per unit area at these currents and at this beam size is high enough to damage the solid targets and cause density fluctuations (boiling) of the cryogenic targets. Bubbles can start to form on the inside walls of the cryo target. To mitigate these issues, a beam raster is implemented approximately 13 m upstream of the target. The fast raster consists of two sets of steering magnets. The first set rasters the beam in the vertical direction and the second in the horizontal. The waveform of the linear raster system is triangular, which results in a rectangular shape at the target. The system maximizes linear velocity and minimizes turning time of the magnet current. The turning time at the vertex of the raster pattern is about 200 ns and the beam traversal time from edge-to-edge is around $20\mu s$. A raster size of 2mm x 2mm was used for the entire experiment. A diagnostic plot of the fast raster is shown in figure 2.8 If one of the two coils fails, a single coil can be set up to provide a 2x2mm raster by increasing the coil current, which is still within the 100A max with margin for longevity. The raster is hooked into the fast shut-down of the machine via two magnetic field probes. If the raster is deactivated for any reason it will stop the beam to protect the target. The field pickup probe is also sent to an ADC module in the counting house. These ADC signals are incorporated into the data stream and allow for a precise beam position on target to be calculated in combination with the survey and alignment information.

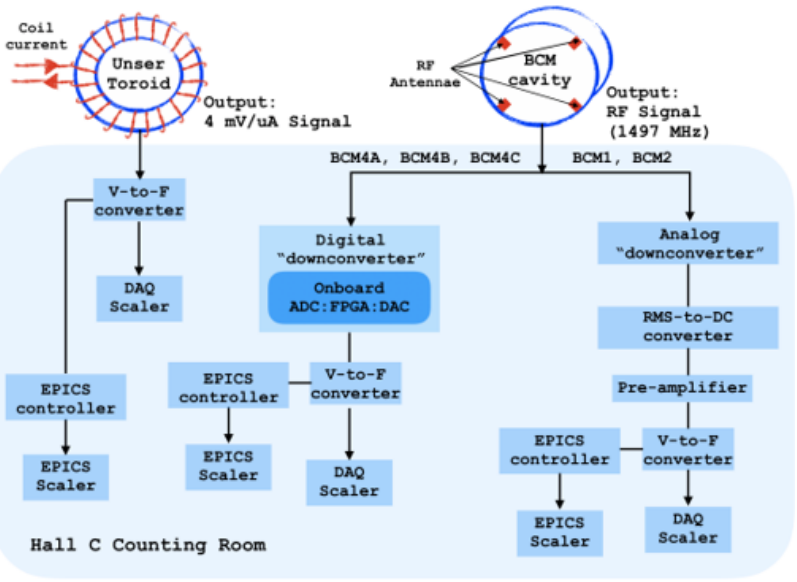


Figure 2.7: BCM readout electronics and their relationship to the data stream.[39].

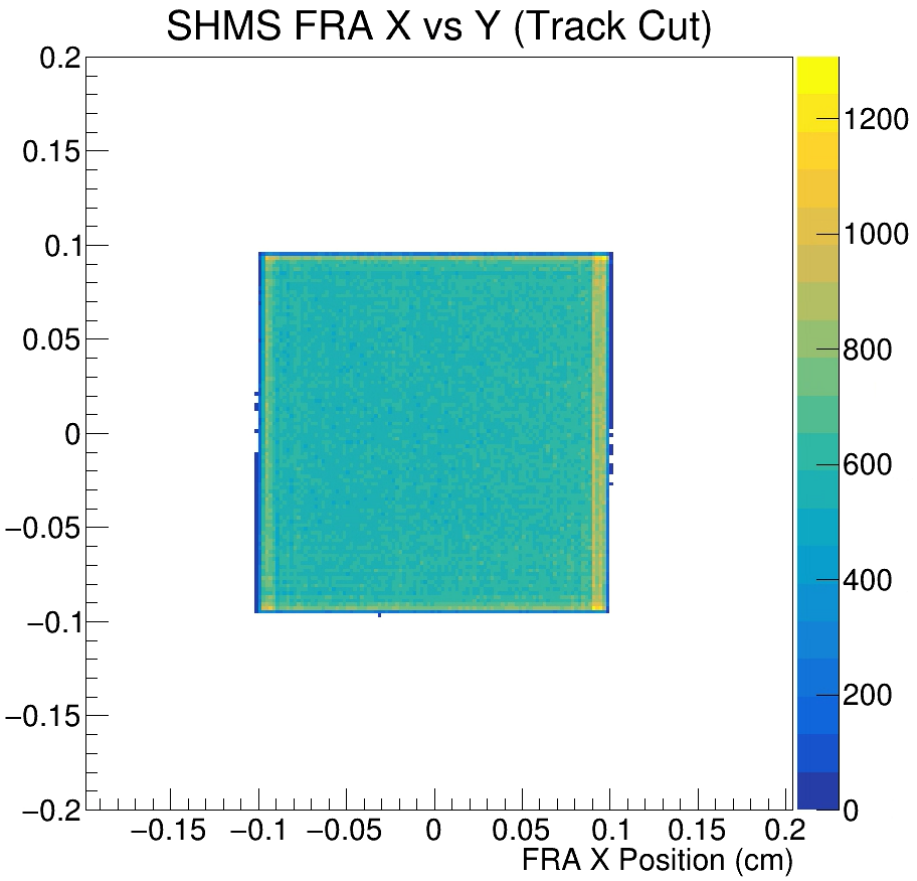


Figure 2.8: The beam is rastered by two pairs of X-Y coils. The magnetic field is read out to ADCs, which are tied into the machine fast shutdown. Shown are the positions at the raster as calculated by the ADC output. The raster distributes the power dissipated on the target over a larger area to prevent damage to the target.

2.3 Target Ladder

The physics targets are located on an indexing target ladder that is contained within an evacuated cylindrical chamber with two inch aluminum walls and an inner diameter of 41 inches. A hydro-formed window composed of 2024-T3 aluminum, 0.02 in thick, spans the exit side of the target chamber to accommodate the scattering angles of the SHMS and HMS as shown in figure 2.9. The thin aluminum window reduces background radiation with respect to the 2 inch thick chamber walls. The target chamber vacuum is held at 10^{-6} torr and is isolated from the upstream beamline with a thin beryllium window. The thickness of the hydro-formed aluminum, atmosphere and beryllium window are required to properly determine radiative effects as described in chapter 4.1. Figure 2.10 is a CAD rendering of the standard target ladder used in 2018 and 2019. Motion in the vertical axis is controlled remotely using EPICS via a GUI that is monitored by a target operator. Each target has operational restrictions that are set based on the heat load and dissipation of the material. The next two sections detail the specific targets used for this experiment and additional information on the pressurized helium target used during the full experiment. Figure 2.11 shows the control interface to manage the targets.

2.3.1 Cryotargets

The first three targets on the ladder are aluminum vessels cool to cryogenic temperatures using a closed loop of liquid helium. The cryo loops are filled from a series of gas bottles attacked to a gas panel and are recirculated through the target and heat exchanger. The heat exchanger is connected to the end station refrigerator and is supplied with 4K and 15K helium to cool the target. Depending on which cryogen is in use, the proportional–integral–derivative (PID) loop is set up to keep the target at a specified temperature. The parameters of the loop are set according to the thermal properties of the cryogens such that the heater will increase power when the beam is off and decrease power when the beam is on to maintain target

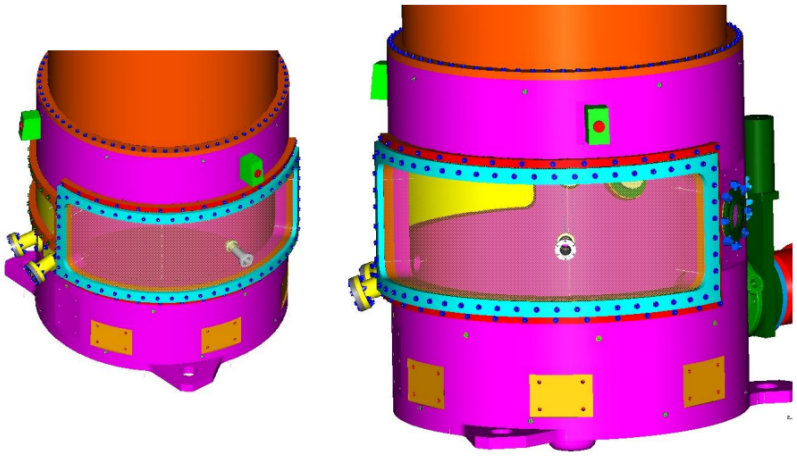


Figure 2.9: CAD drawing of the Hall C Target Chamber design. The flange of the beam exit subtends a small portion of the target window. This minimizes scattering from the target chamber. Reprinted from [40, 41].

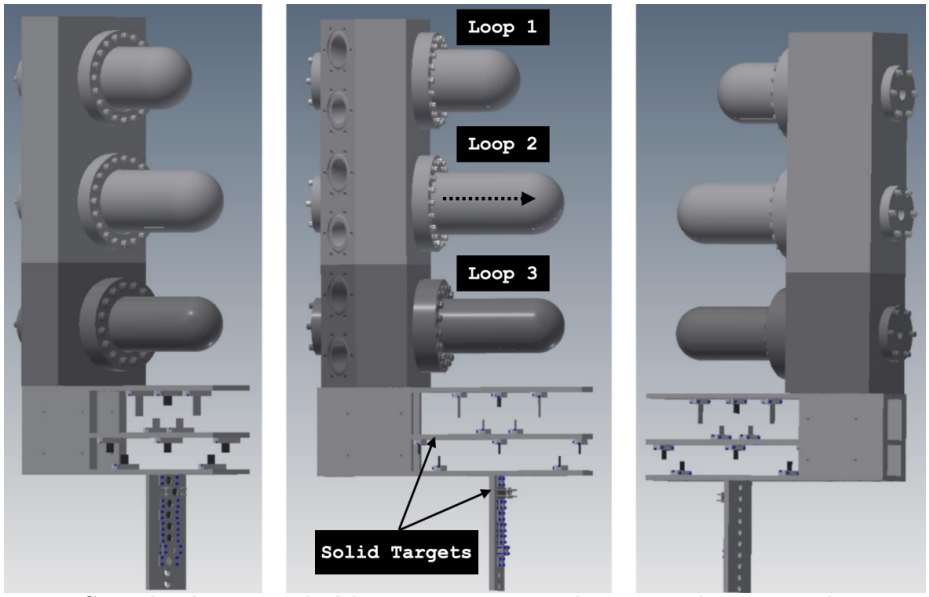


Figure 2.10: Standard Target ladder. From top to bottom, three cryo loops, two optics targets, and suspended solid target ladder[39].

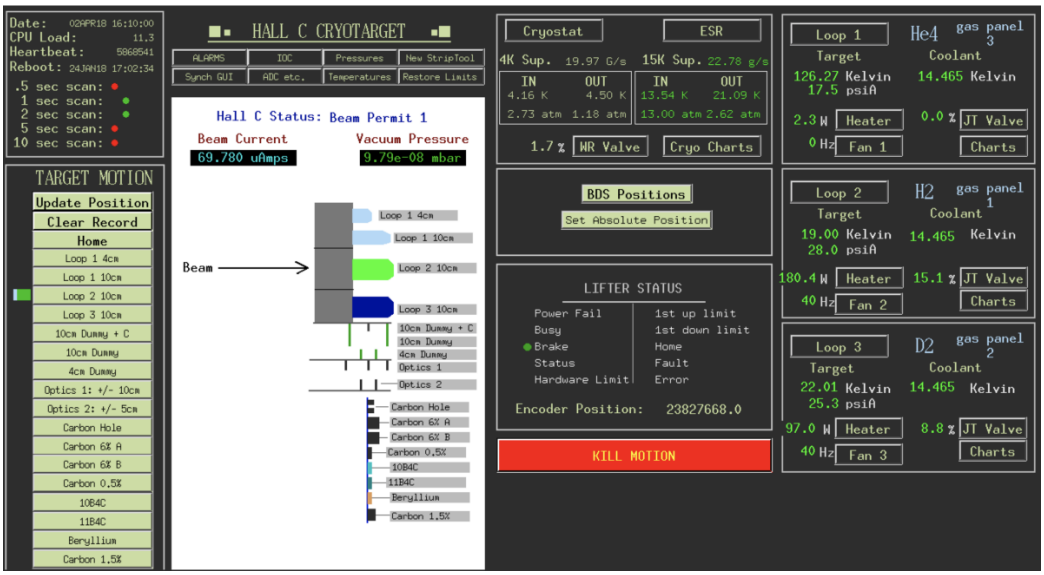


Figure 2.11: Target controls GUI used by target operators. Additional information about target operation is detailed in [36].

temperature. The cryogen flow can be increased to accept higher beam current with the same PID settings. When the beam is at full current, there should be a reserve of 75W of heater power. A flow diverter is placed inside the cryo cell to ensure a continuous flow velocity throughout the target cell. This ensures uniform target temperature and minimizes local density fluctuations, which would cause an apparent drop in target thickness.

2.3.2 Solid Targets

All the solid targets are thin foils with thicknesses ranging from 2% - 6% radiation lengths. The selection of nuclei targeted approximate scans at constant A and N/Z for the same density.

2.4 Spectrometers

All of the production data was taken using the super high momentum spectrometer (SHMS). On occasion, the high momentum spectrometer (HMS) was used in combination with the SHMS to measure exclusive processes for calibration purposes. Both the SHMS and HMS are focusing spectrometers with a high degree of background suppression and are capable of operating at high luminosity. The spectrometers are mounted on bearings at the central pivot and ride on train trucks on steel rails which allows for remote rotation. The optic elements of the spectrometers accept a collimated beam of scattered particles from the interaction point (target) and bend the particles up towards a series of detectors in a lead-lined concrete enclosure (detector hut). The bend disperses the particles according to momentum and the hut shields from other particles scattering in all directions in the hall. Spectrometer angles are determined remotely by a camera aligned with a high precision vernier scale that can measure angles to within 5 thousands of a degree as shown in figure 2.13. The SHMS is located beam left and can be rotated between 5.5°(8.0°) and

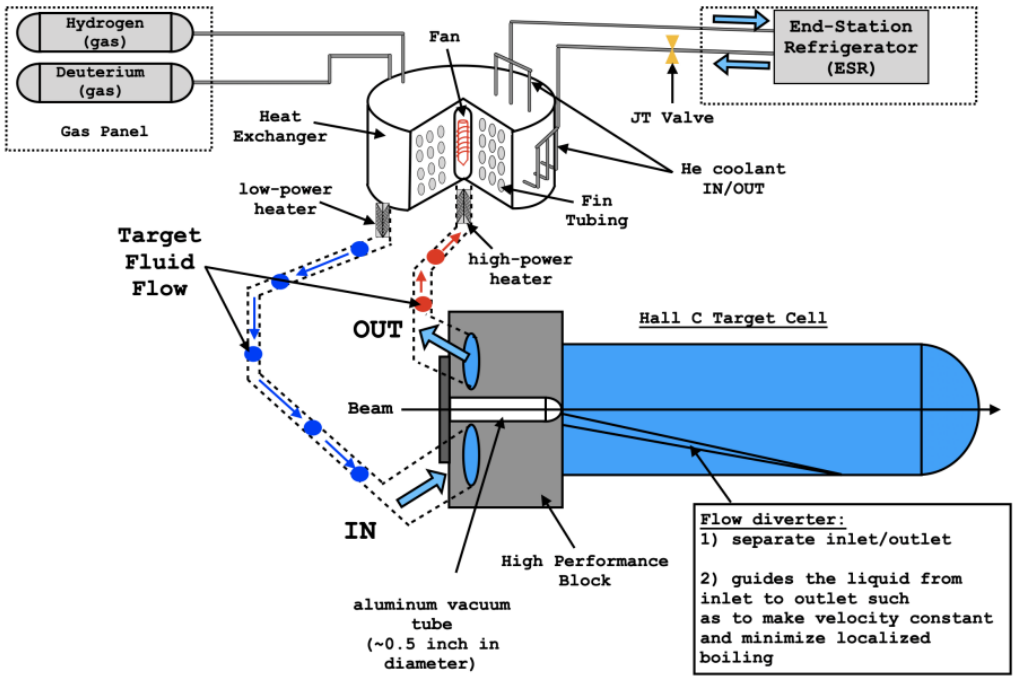


Figure 2.12: Illustration of heat exchanger for Hall C cryo targets [36].

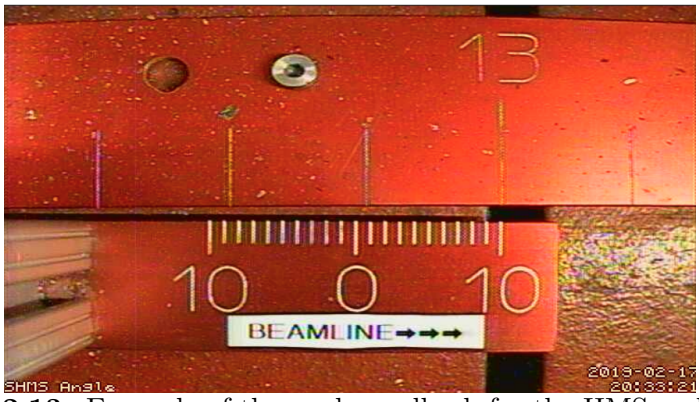


Figure 2.13: Example of the angle readback for the HMS and SHMS.

40° when the small (large) beam pipe is installed. The HMS is located beam right and can be rotated between 10.5° and 80°. The larger beam pipe was installed for all XEM2 running, so the minimum angle achievable was 8.0°. Spectrometer offsets are determined by the Survey and Alignment group and each component in the spectrometer is measured relative to the standard monuments in the hall. Additional information about spectrometer offsets is found in section 3.3.

2.4.1 Spectrometer Magnets and Optics

The spectrometer coordinates are defined with the $\hat{z}$ direction along the optical axis inside the spectrometer. $\hat{x}$ points down in the dispersive direction and $\hat{y}$ points in the non-dispersive direction (beam-left), shown in figure 2.14. There are two frames used, the focal plane frame and the target frame. The focal plane, denoted with 'fp', is centered half-way between the drift chambers and lies along the optical axis of the spectrometer detectors. The target frame is centered at the target and have the subscript 'tar'.

2.4.2 Event Reconstruction

Track information from the drift chambers, described in 2.5.2, are used in combination with a reconstruction matrix to determine particle trajectory and interaction point in the target. The position at the focal plane is defined by the variables $(x_{fp}, y_{fp}, x'_{fp}, y'_{fp})$. x'_{tar} and y'_{tar} are the slope of the tracks $\frac{dx}{dz}$ and $\frac{dy}{dz}$. The reconstruction is done by a set of polynomial functions, one for each reconstruction variable.

$$x'_{tar} = \sum_{i,j,k,l,m} X'_{i,j,k,l,m} x^i_{fp} x'^j_{fp} y^k_{fp} y'^l_{fp} x^m_{tar} \tag{2.3}$$

$$y_{tar} = \sum_{i,j,k,l,m} Y_{i,j,k,l,m} x^i_{fp} x'^j_{fp} y^k_{fp} y'^l_{fp} x^m_{tar} \tag{2.4}$$

$$y'_{tar} = \sum_{i,j,k,l,m} Y'_{i,j,k,l,m} x^i_{fp} x'^j_{fp} y^k_{fp} y'^l_{fp} x^m_{tar} \tag{2.5}$$

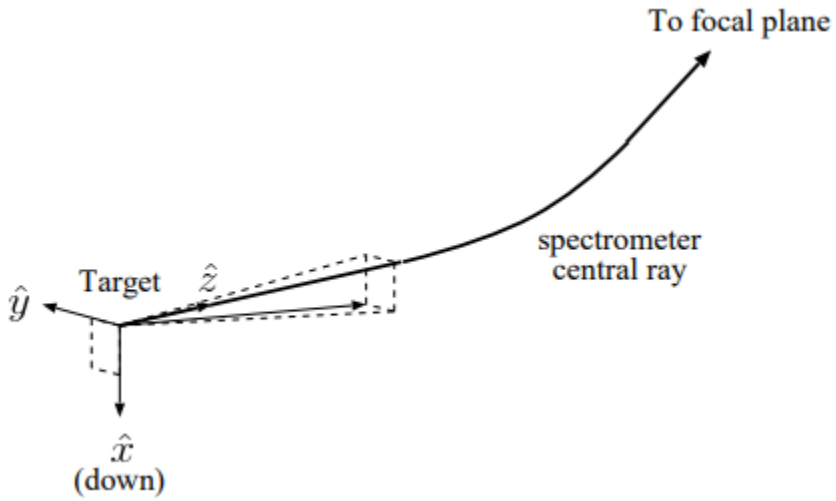


Figure 2.14: Mapping between beam and target coordinate system. Reprinted from [31].

$$\delta_{tar} = \sum_{i,j,k,l,m} D'_{i,j,k,l,m} x^i_{fp} x'^j_{fp} y^k_{fp} y'^l_{fp} x^m_{tar} \tag{2.6}$$

The system of equations is under-constrained (4 equations, 5 unknowns), so x_{tar} is taken to be zero. The small acceptance of the spectrometers ($<$ 100mr) allows the slopes to be treated as angles. Spectrometer mispointing, beam offsets, and raster effects must be taken into account to accurately reconstruct the position at the target from focal plane positions. The reconstruction equations are presented here without further elaboration.

$$y^{rec}_{tar} = y^{vert}_{tar} - z^{vert}_{tar} y'_{tar} \tag{2.7}$$

$$x^{rec}_{tar} = x^{vert}_{tar} - z^{vert}_{tar} x'_{tar} \tag{2.8}$$

$$z^{vert}_{tar} = \frac{y^{rec}_{tar} + x^{beam}(cos(\theta) + y'_{tar} sin(\theta)}{sin(\theta) - y'_{tar} cos(\theta)} \tag{2.9}$$

Vert in the equations refers to the vertex and rec corresponds to reconstructed quantity. The aforementioned quantities are used to set up a single value decomposition problem (SVD) to optimize the matrix elements given a sieve and hydrogen elastic data. This method is outlined in [42].

2.4.3 SHMS Capabilities

The SHMS was designed to accept electrons with a maximum momentum of 11GeV/c, which corresponds to the maximum beam energy deliverable to Hall C. The SHMS is also capable of reaching far forward angles at very high luminosities. Table 2.1 outlines the capabilities of the SHMS. True capabilities are limited by the chosen kinematics and physics of interest. Figure 2.15 and 2.16 illustrate the layout of the Hall C spectrometers.

Table 2.1: Capabilities of SHMS spectrometer.

Parameter	SHMS Design
Range of Central Momentum	2 to 11 GeV/c for all angles
Momentum Acceptance	$-10\% \leq \delta \leq 22\%$
Scattering Angle Range	5.5 to 40 degrees
Solid Angle Acceptance	>4.0 mSr
Horizontal Angle Resolution	0.5 - 1.2 mrad
Vertical Angle Resolution	0.3 - 1.1 mrad
Vertex Length Resolution	0.1 - 0.3 cm
Tracking Rate Capability	5 MHz
Beam Capability	Up to 90μA

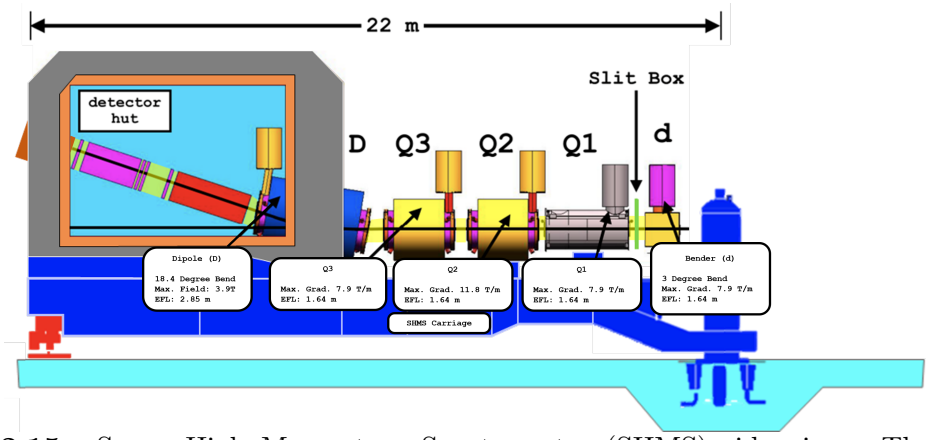


Figure 2.15: Super High Momentum Spectrometer (SHMS) side view. The magnet elements are arranged in dQQQD configuration. The first dipole (d) bends the beam in the non-dispersive direction to reach smaller beam angles. The quadrupoles (Q) focus the beam. Modified from [39].

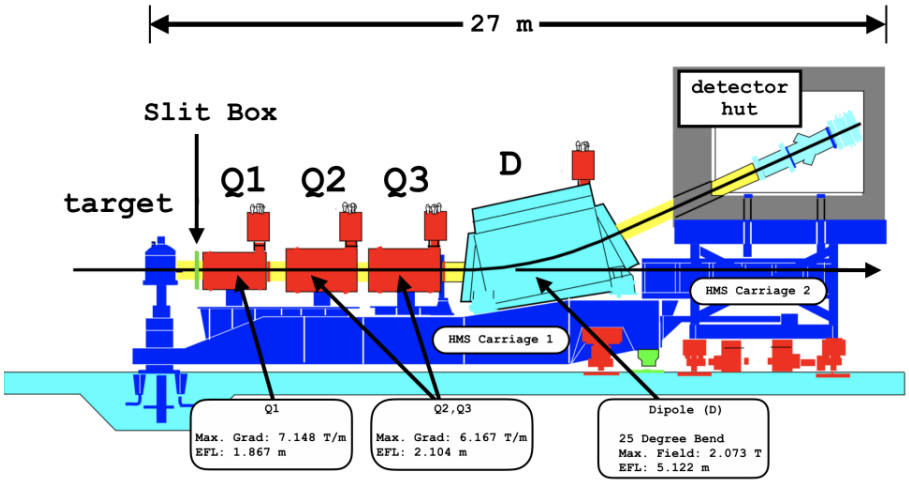


Figure 2.16: High Momentum Spectrometer (HMS) side view.[39]

2.5 Detectors

The SHMS and HMS have very similar detector stacks since the SHMS was modeled after the HMS. Both spectrometers have a pair of drift chambers, two pairs of hodoscope planes, a calorimeter and a series of Čherenkov detectors as illustrated in figure 2.17. The hodoscope planes register signals from charged particles passing through the detector stack, and are combined in hardware logic to form the main trigger. The drift chambers offer the highest track resolution and are the main tracking detector. The electronic calorimeter is split into a pre-shower and shower to absorb all of the energy of charged particles while distinguishing between pions and electrons based on energy absorption characteristics. The noble gas (heavy gas) Čherenkov detector can be tuned to specific pion thresholds by gas mix (pressure). The aerogel Čherenkov is used for very low momentum particle discrimination. Stricter triggers involving Čherenkov and calorimeter signals (particle ID, PID) in combination with the 3/4 hodoscope trigger can be used to further select electrons events at the trigger level. Additional details on the trigger are found in section 2.6.

2.5.1 Hodoscopes

The SHMS and HMS both have 4 hodoscope planes. S1X, S1Y, S2X, S2Y. The planes are grouped together into two X-Y pairs and are arranged 2.2 m apart from one another. The first pair is located upstream of the last drift chamber and the second pair is upstream of the pre-shower calorimeter. The first three planes of the hodoscope are made of scintillating plastic for fast timing response while the last plane is composed of quartz to reduce signals from low energy particles. The organic scintillator responds to charged particles by emitting electron-hole pairs that traverse the material until reaching luminescent centers where the molecules quickly relax via the emission of a photon via fluorescence. The quartz scintillating bars only produce light via Čherenkov radiation, which is detailed in the Čherenkov section. Once a charged particle passes through the scintillator, the light emitted is totally internally

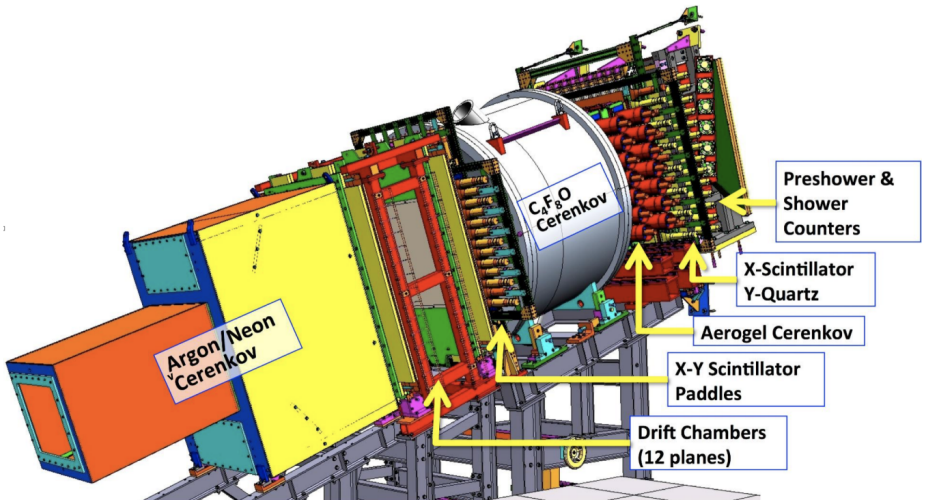


Figure 2.17: CAD rendering of SHMS detector stack located inside the shield hut[39].

reflected down to the end of the scintillating bars and into two photomultiplier tubes, one at each end. The scintillating bars are wrapped in aluminum and electrical tape to reflect any partially refracted light back into the scintillator and to prevent light in the detector hut from making it into the PMTs. The scintillating bars are overlapped with one another so no charged particles are missed as they pass through the planes. In the SHMS, S1X and S1Y have 13 scintillating bars, S2X has 14 bars, and S2Y has 21 quartz bars. Figure 2.18 illustrates the frame that holds the scintillating bars and PMTs in a hodoscope plane. Scintillators and PMTs respond quickly to incident light making hodoscopes ideal for triggering detector readout. Additional details of the 3/4 trigger are found in the trigger section. The hodoscopes are read out by both ADCs and TDCs. Enhanced timing resolution is achieved by taking the difference in timing between the PMTs on either end of a scintillating bar. This is discussed in detail in the detector calibration section 3.1. Additionally, the combinatorics of having 3/4 planes fire yields information about tracking efficiency and hodoscope efficiency that is used for absolute cross-section determination. This is discussed in more detail in 3.4.

2.5.2 Drift Chambers

The drift chambers are the primary tracking detector in the SHMS and HMS. Drift chambers are multi-wire proportional chambers (MWPCs) with additional timing information of current pulses. This increases the precision of path reconstruction. The key operating characteristic of a MWPC is the uniform electric field that draws ions into the anode with minimal lateral motion. This characteristic ensures a uniform mapping exists between drift-time and drift distance. As charged particles of at least a few keV travel through a gas, they ionize the gas on average once every $300\mu m$ at STP. When charged particles liberate electrons in the presence of an electric field, the electrons will drift towards the anode and create knock-on electrons causing a Townsend avalanche. The avalanche collects on a sense wire and is amplified.

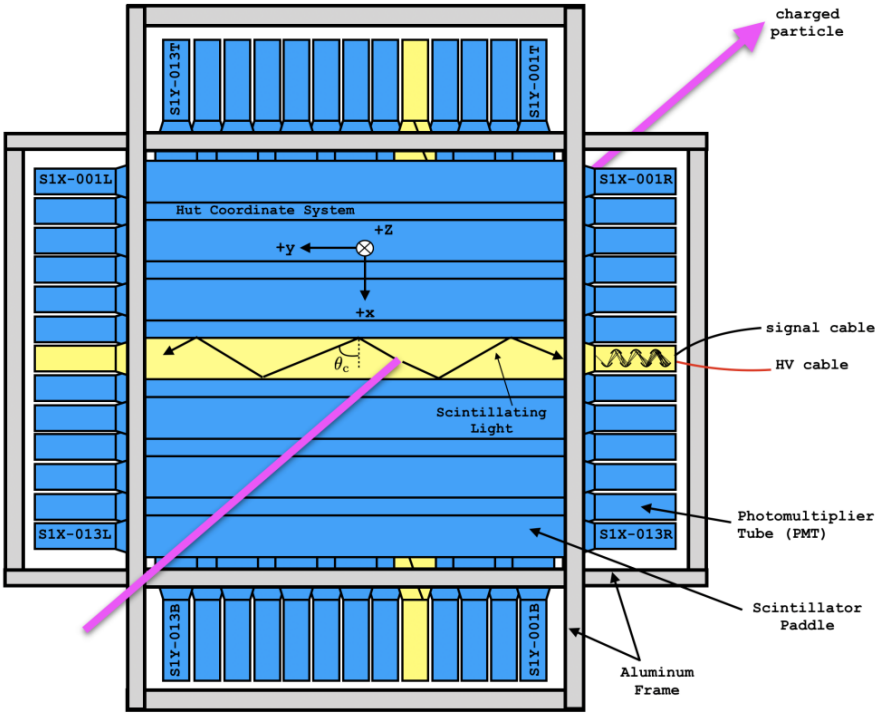


Figure 2.18: Hodoscope plane illustration reprinted from [36]

Timing information for current pulses is captured using a time-to-digital converter in reference to the 3/4 hodoscope trigger and provides sub-millimeter precision to tracks. The avalanche of electrons is quenched using a secondary gas that acts as an electron donor to allow the drift chamber to return to normal operation. Figure 2.19 illustrates the operating principle of a drift chamber. For the HMS and SHMS, each drift chamber consists of 6 wire anode planes and 8 cathode planes positioned between two cathode windows. A middle plane acts as the mounting plane for 16-channel amplifier/discriminator cards, and separates the chamber into two segments. DC1 and DC2 are of the same design and are mounted about 80cm from each other as measured from the middle plane as shown in figure 2.20. The focus of the SHMS coincides with the center of the two drift chambers. The sealed drift-chamber has a flow of 50:50 Argon/Ethane, which is contained by the edges of the drift-chamber planes and the cathode windows. There are three sets of planes each held at 60° relative to one-another so up to three coordinates can be used to form a track. An additional three primed coordinates are introduced to make a second independent measurement of the position to resolve what is known as the left-right ambiguity. It is impossible to determine which side of a sense wire the ionization occurred with respect to the wire, so a second sense wire is oriented in the same direction with a slight offset to make a second measurement. Figure 2.21 illustrates a head-on view of the drift chambers. Details pertaining to the calibration and geometry of the drift chamber are outlined in chapter 3.1.

2.5.3 Gas Čherenkov

The main purpose of Čherenkov detectors in this experiment is to suppress pions at the trigger level and identify pion background. When a charged particle passes through a material faster than light could travel in that medium, an electromagnetic disturbance is created in the medium that produces light. The light is conically

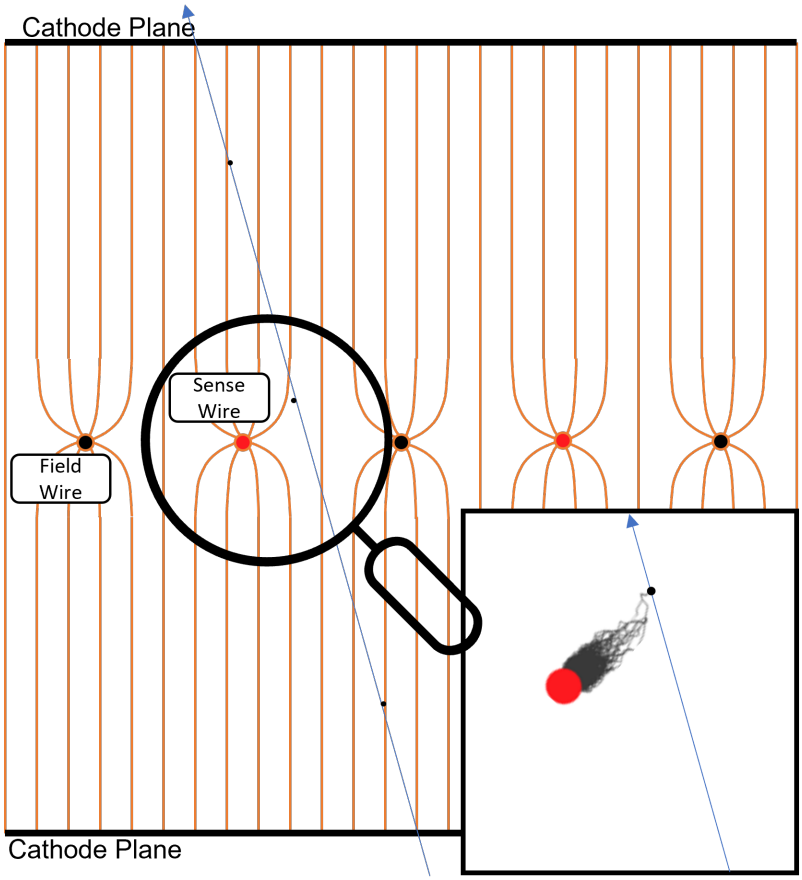


Figure 2.19: Each plane consists of alternating field and sense wires. Each sense plane is separated by cathode planes. Top view of a sense wire surrounded by field wires. Distance between field wires and cathode planes not to scale.

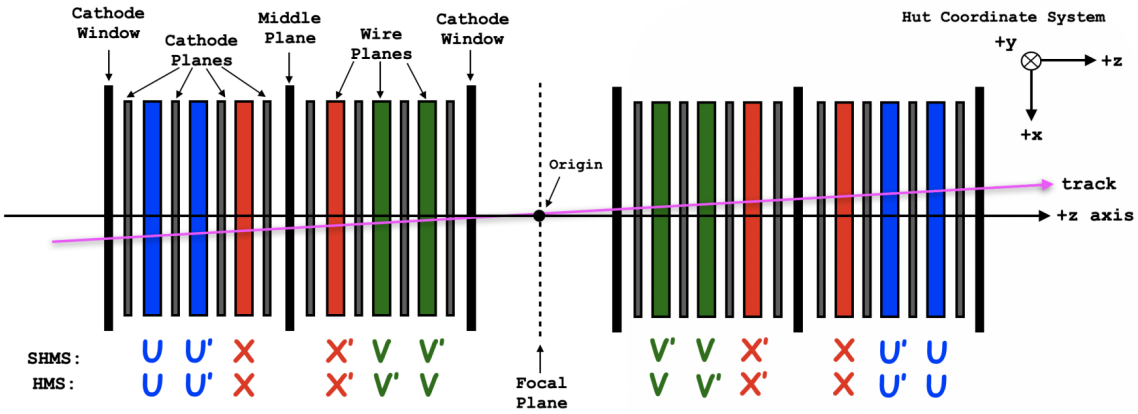


Figure 2.20: Side view of drift chambers. Reprinted from [36]

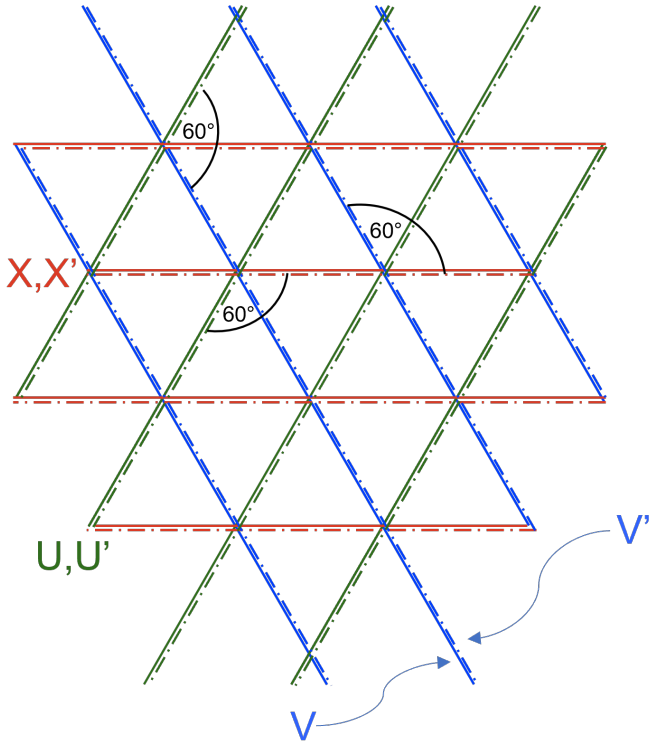


Figure 2.21: Each plane consists of alternating field and sense wires. Each sense plane is separated by cathode planes. Top view of a sense wire surrounded by field wires.

distributed along the trajectory of the particle with an angle given by

$$\cos\theta = \frac{1}{\beta n} \tag{2.10}$$

The index of refraction $n = c/u$ and $\beta = v/c$ where c is the speed of light in a vacuum, u is the speed of light in the material, and v is the speed of the particle. Low momentum pions are separated from high momentum pions by choosing a minimum momentum over which particles must move to produce Čherenkov light. This is commonly referred to as pion threshold because low momentum pion background can be separated from a sample of high-momentum electrons. Above a certain pion threshold, the pions are indistinguishable from electrons in the Čherenkov detector. The index of refraction can be manipulated by changing the makeup of the gas or by changing the pressure of the gas since the index of refraction of a gas is proportional to Pressure by

$$P \propto (n-1) \tag{2.11}$$

The SHMS has three Čherenkov detectors excluding the SHMS S2Y quartz hodoscope plane: The noble gas Čherenkov (NGC), heavy gas Čherenkov (HGC), and aerogel Čherenkov detectors. The NGC was the primary Čherenkov detector used, and thus is the only one described here. The NGC detector was designed to have thin windows to preserve the SHMS resolution by minimizing multiple scattering since the NGC is the furthest upstream detector. Due to the thin windows, the NGC is constrained to operated at one atmosphere, so the only way to modify the pion threshold is by altering the gas mixture. The NGC can distinguish between pions and electrons with momenta between 6 GeV/c and 11 GeV/c. This is accomplished by producing a mixture of Argon (6GeV/c pure atmosphere) and Neon (11 GeV/c pure atmosphere) to tune the pion momentum threshold. Figure 2.22 illustrates the noble gas Čherenkov detector. This efficiency is discussed more in the efficiencies section 3.4. The NGC detector is 0.9 m long with 4 spherical mirrors that reflect the light onto 4 PMTs. The inside surface of the tank is painted black to prevent reflection off the internal

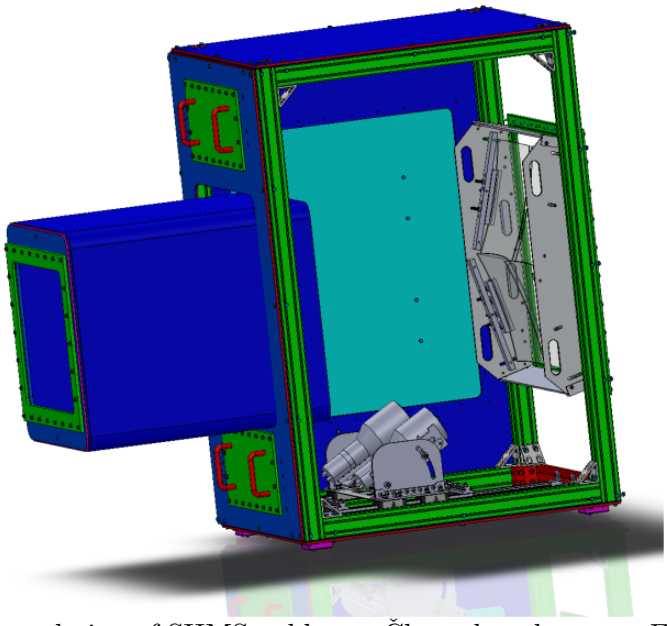


Figure 2.22: CAD rendering of SHMS noble gas Čhernekov detector. Four mirrors reflect light from four quadrants centered on the beam position to four PMTs located at the edge of the Čherenkov detector.[39]

surface to minimize light from cosmic rays. The 4 PMTs are outside of the active area of the detector volume. A major constraint in the gas selection is the number of photoelectrons expected from an electron of a specific energy. If the number of photoelectrons is too low, then there is a non-zero probability the Čherenkov detector would not fire for a real electron.

2.5.4 Lead Glass Calorimeters

Both spectrometers have a lead glass calorimeter at the end of the detector stack. The calorimeter is used to distinguish between electrons and pions. As electrons and pions traverse the lead-glass calorimeter blocks, they lose energy via Bremsstrahlung photons. Electrons also lose energy via pair-production while pions cannot pair produce. Since pions cannot pair produce, they deposit a relatively constant amount of energy in the calorimeter whereas the electrons deposit all of their energy in the calorimeter over a given radiation length of material. The length of the calorimeter must be long enough to absorb all of the energy. Radiation length is the length of material traversed by a high-energy electron whereby it will lose $1/e$ of its energy to Bremsstrahlung radiation. Radiation length also coincides with $7/9^{ths}$ the length a high energy photon will pair produce. This length can be expressed in cm by dividing by the materials density. The SHMS shower(pre-shower) is composed of F-101(TF-1) type lead glass blocks. The shower(pre-shower) blocks came from the decommissioned HERMES (SOS) detectors and are of different dimensions. The pre-shower blocks are 10 x 10 x 70 cm^3 and the 224 modules of the shower are 8.9 x 8.9 x 50 cm^3. The pre-shower blocks are oriented with their long axis perpendicular to the central axis of the hut and the shower blocks are oriented with their ends facing the axis of the hut. A small angle is introduced to the calorimeter of 2° to ensure particles don't pass straight through the pre-shower between the blocks as illustrated in figure 2.23. The thickness of the pre-shower is 3.65 radiation lengths given and the thickness of the shower is 14.6 radiation lengths.

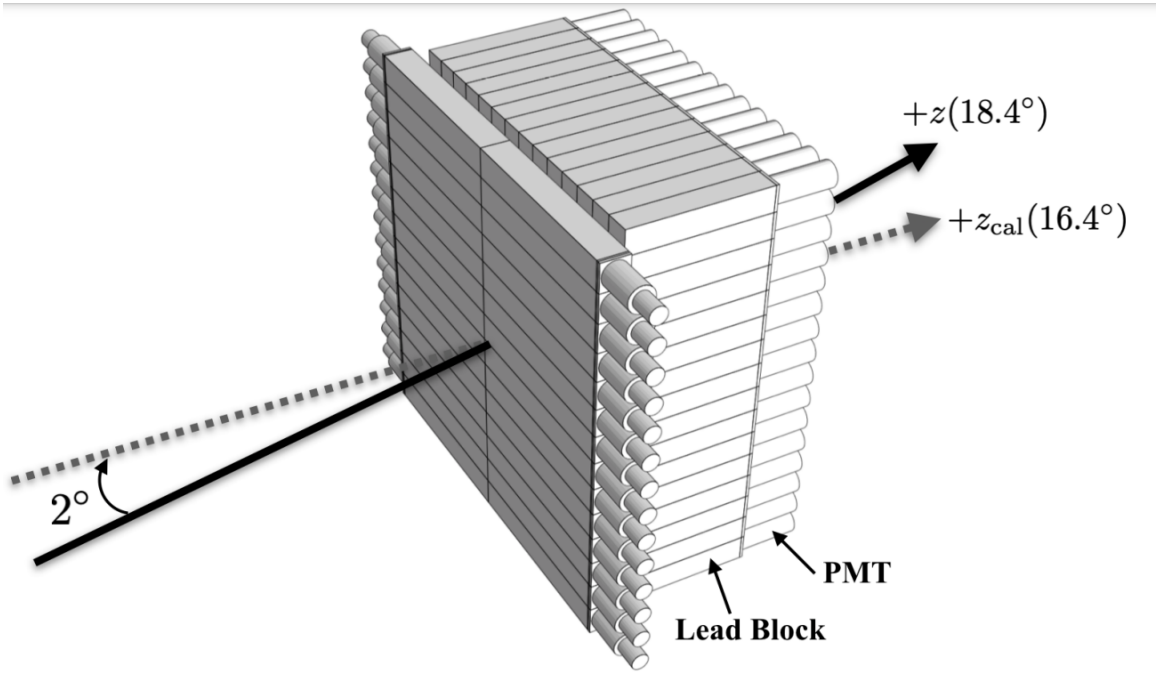


Figure 2.23: SHMS pre-shower and shower calorimeters. A slight angle is introduced relative to the z axis of the hut to prevent electrons from going between blocks without detection. Reprinted from [39].

2.6 Data Acquisition and Trigger

Data is acquired and stored using an in-house software system called CODA (CEBAF Online Data Acquisition). Data is streamed into one or several files with headers describing events and event types. The meaning and form of each event type is described in section 2.6.2. Low level signals from ADCs and TDCs tied to detector elements are logically combined in hardware modules to form logical pulses called pre-triggers. These fast logic pulses are then combined to form higher level logic pulses (triggers) that likely map to real physics events. The highest logic pulse is called level one accept, which subsequently requests all slave modules to write the previous event to disk. If the system is not busy, the current event is written to disk, but if the computer is busy the computer is said to be dead. Computer and electronic dead time are described in 3.2. The standard Hall C triggers were used for all XEM2 experimental run periods. These triggers are well studied and minimize random coincidence events while maximizing real physics events. The triggers are defined in such a way that the efficiency of each trigger can be determined. The definition of the triggers used are described in 2.6.1.

2.6.1 Trigger Configurations

There were several different triggers used for different purposes during the experiment. The 3/4 trigger, which accepts the most events, was used to study the trigger-level rejection of events for triggers that require a particle ID cut. The ELREAL trigger, which places cuts on the noble gas Čherenkov and electron calorimeter, was used for most of the production data to minimize file size on disk and maximize the real physics data rate. The trigger rate is optimized to the write rate of the computer by the use of a prescale factor. This factor effectively writes every Nth event to disk. The pre-scale factor also allows us to minimize the systematic uncertainties associated with beam current by reducing the total number of events written. This is expanded in section 3.2. This minimizes computer dead time, minimizes file size on disk, minimizes

post-analysis time, and maximizes physics events of interest. Although the DAQ is capable of taking multiple trigger types at a time, it was decided to only one trigger type at a time to minimize the uncertainty on dead time. Having multiple trigger types increases the time to analyze the data and introduces an ambiguity as to which trigger fired an event and what the associated dead times are for each trigger type. The trigger that accepts the most events is the 3/4 trigger, which only depends on the hodoscope. All of the other triggers used utilize the 3/4 trigger and apply more stringent particle ID cuts using the calorimeter and Čherenkov detectors. The main trigger that was used for production data taking was EL-REAL, which is can be traced in 2.24. EL-REAL is an electron trigger that requires scintillator hits and user-defined particle identification signals.

2.6.2 CODA Event Types

Multiple read out controllers (ROCs) send their data to the trigger interface to be saved to disk according to criterion set by the trigger supervisor. There are three types of events considered here, scaler events, epics events, and trigger events. Scalers are modules that simply count very accurately and accumulate said counts in a regular interval set by the trigger rate and time between scaler reads. EPICS events is a stream of output from the Experimental Physics and Industrial Control System (EPICS). Devices such as temperature probes, position encoders, beam state, etc. are read at regular intervals. These are useful in diagnosing issues such as unintended target motion, BCM warm-up events, etc. Finally, Trigger events are the readout of all detector components at the acceptance of the main trigger (L1-accept).

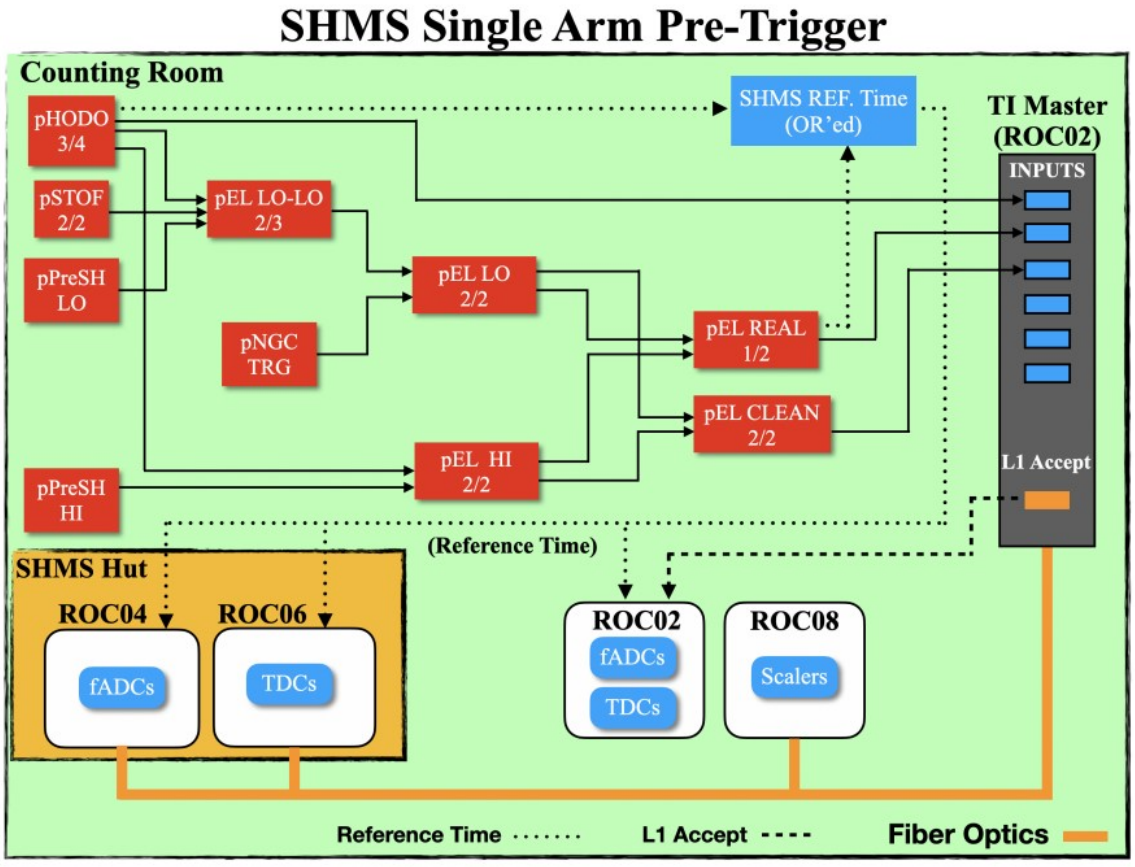


Figure 3.46: SHMS single arm trigger electronics diagram.

Figure 2.24: SHMS trigger map from reprinted from DocDB[36]. The EL-REAL trigger was the main trigger used in this experiment, and requires at least EL-LO or EL-HI to trigger.

Chapter 3

Inclusive Data Analysis

This chapter builds upon details provided in the experimental setup on the detectors, trigger and data acquisition system. Once the raw data is written to disk, a series of detector calibrations and efficiency corrections are applied to the data using the hall C analyzer (hcana). By the end of this chapter, the charge normalized and efficiency correct electron yield will be presented. After correcting the electron yield for all known experimental effects, we are able to directly compare the reconstructed data to a Monte Carlo simulation of the acceptance and cross-section model to extract experimental cross-sections. The Monte Carlo and cross-section model is described in chapter 4. First, detector calibrations methodology will be presented. Next, the computer and electronic live time is determined. Then, detector and trigger efficiencies are determined. Finally, studies are presented on target density fluctuations, and spectrometer optics.

3.1 Detector Calibrations

Before any detector calibrations are performed, cuts are placed on event timing to select good events and to reduce random coincidence. A large sample of events are binned to the resolution of the ADCs and TDCs and a well placed cut removes accidental events from the analysis. In the case of multi-hit ADCs and TDCs, the

reference time cut selects the first event after the cut as the primary physics event. To refine the event selection further, window cuts are placed on each detector component to remove backgrounds that come after the reference time, but are not correlated with the physics trigger.

Once the Reference time signals and timing window signals are determined, each detector is calibrated individually starting with the hodoscope, and Čherenkov detectors. Calibration of the drift chambers and calorimeter follow as they depend on the other detector calibrations. The hodoscope calibration is performed only once per experiment since the timing of events does not change throughout the experiment unless a hardware change occurs. Čherenkov detectors are typically a small number of channels and are only checked once per high voltage setting. The characteristic response of the PMTs are calibrated to the single photo electron peak where possible.

The drift chamber and calorimeter have many channels that need to be calibrated at each kinematic setting and for each trigger configuration. In this way, track resolution in the drift chambers is optimized and the best separation between pions and electrons is achieved in the calorimeter. Only once these low-level signals are calibrated can systematic checks on detector performance be ascertained.

3.1.1 Reference Times and Timing Windows

The logical pulse(s) that make up the trigger as described in section 2.6 are copied and distributed to each read out controller (ROC) in the detector stack so common timing can be established. This signal is known as the reference time and it serves two functions:

- Define a common stop for all detectors so that a pre-determined lookback window can be written to disk.
- Determine precise timing of pulses in TDC1190 modules.

Readout of the TDC1190 modules is initiated by a copy of the level-1 accept signal sent to the front-end electronics. There is a 4 ns jitter on the L1 accept that is intrinsic

to the data acquisition system. There are two clocks on the TDC, a fast clock (10 GHz) and a slow clock (40 MHz). The detector start latches onto the 40MHz clock and so the timing of the signal can fall any time within a 25 ns period. In order to increase the timing resolution to the specified 0.1ns, a copy of the L1-accept is sent into a channel of the TDC. The copy of the L1-accept acts as the stop signal and the 10 GHz fast clock is latched to the leading edge of the next clock cycle. In this way, the time resolution of the TDC module is about 0.1ns. The raw TDC spectrum does not account for this precise clock and so a 29 ns (25 ns intrinsic + 4 ns trigger) signal peak is visible within the raw TDC spectrum.

The analyzer takes the first signal within the TDC spectrum to be a good hit, but that is not always the hit associated with the trigger. By placing a reference time cut, hcana uses the first hit after the cut which is more likely than not a good hit. Figure 3.1 illustrates the reference time cut and background removal. The cut is kept loose to ensure no events are lost. Non-physics events can be excluded by physics cuts, so only a small inefficiency is introduced with a loose reference time cut.

3.1.2 Timing Windows

Timing window cuts are used to remove background events that are out-of-time with the physics signal relative to the trigger time that pass the reference time cut. Timing window cuts are made on a per-PMT basis and are defined as the time difference between the TDC time and ADC pulse time. This difference accounts for the time an event started based on the hodoscope. The difference between ADCs and TDCs is calculated for each hit in each ADC and TDC. Drift chamber timing windows are based on the drift times for each plane. Adc and Tdc times are relative to the reference time subtracted times, so they are known to about 0.1ns.

The ADC-TDC difference would ideally be a delta function for real physics events and all other events would be out-of-time. The expected delta function of events is spread out to form a gaussian distribution because of the finite resolution of the

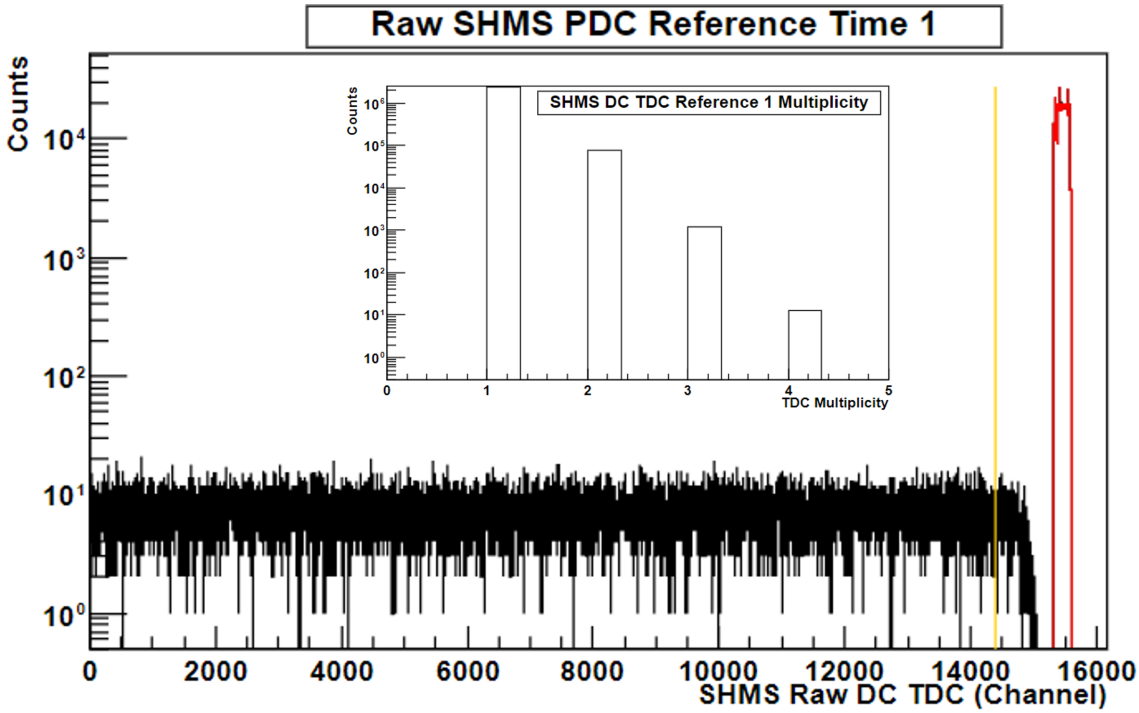


Figure 3.1: SHMS reference time spectrum for a 3/4 single-arm trigger. Background hits are shown in black and good hits in red. Multiplicity for the selected reference time spectrum. Width of the 3/4 trigger is 300 channels ($\approx 30ns$). Yellow line is the reference time cut applied for production data.

detectors and target thickness. Drift chamber timing window cuts are made using the raw drift time spectrum to remove background when there are many TDC hits. Some PMT timing window cuts are shown as examples in 3.2.

The green lines represent the timing window cuts. Events outside this region are removed. The Čherenkov detector is a special case where multiple peaks are integrated to obtain the total light yield.

3.1.3 Hodoscope Calibration

The hodoscope is used to form the primary trigger and it provides propagation velocity of particles through the detector stack without track information. The propagation velocity is constructed from the arrival time at both PMTs in a hodoscope paddle with the output of at least two PMTs connected to another scintillating paddle in another plane. Several timing corrections must be applied to the TDC time as illustrated in figure 3.3. The corrected time is determined by applying a time walk correction (t_{TW}), a cable length correction (t_{cable}), a propagation time correction (t_{prop}), and finally a plane time difference correction (t_λ).

$$t_{corr} = t_{raw} - t_{TW} - t_{cable} - t_{prop} - t_\lambda \tag{3.1}$$

T_{raw} is the reference time subtracted output of the TDC1190 and t_{corr} is the arrival time of the particle to the paddle. The plane time difference correction is the single value decomposition of a system of six linear equations defined by the time difference between any two paddles. See figure 3.4. More details on the calibration of the Hall C hodoscopes is found in [43]. For a relativistic electron, the velocity relative to the speed of light, β, is given as:

$$\beta = \frac{v}{c} = \frac{pc}{E} = \frac{pc}{\sqrt{p^2c^2 + m^2c^4}} = \frac{1}{\sqrt{1 + (mc/p)^2}} \tag{3.2}$$

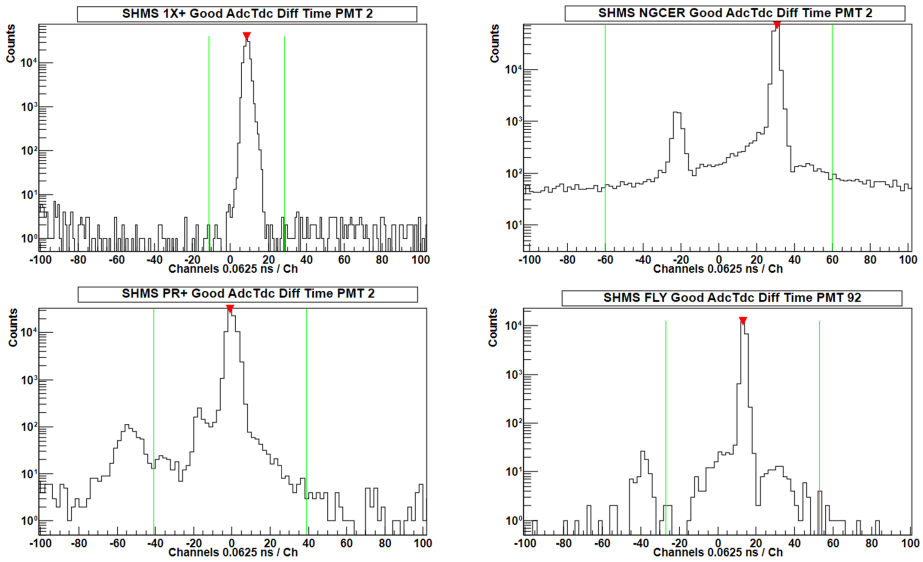


Figure 3.2: SHMS hodoscope (top left), Noble gas Čherenkov (top right), SHMS calorimeter pre-shower (bottom left) and SHMS flyseye calorimeter (bottom right). Time is time window cuts for an individual PMT channel (or DC plane). x-axis given as time difference in channels.

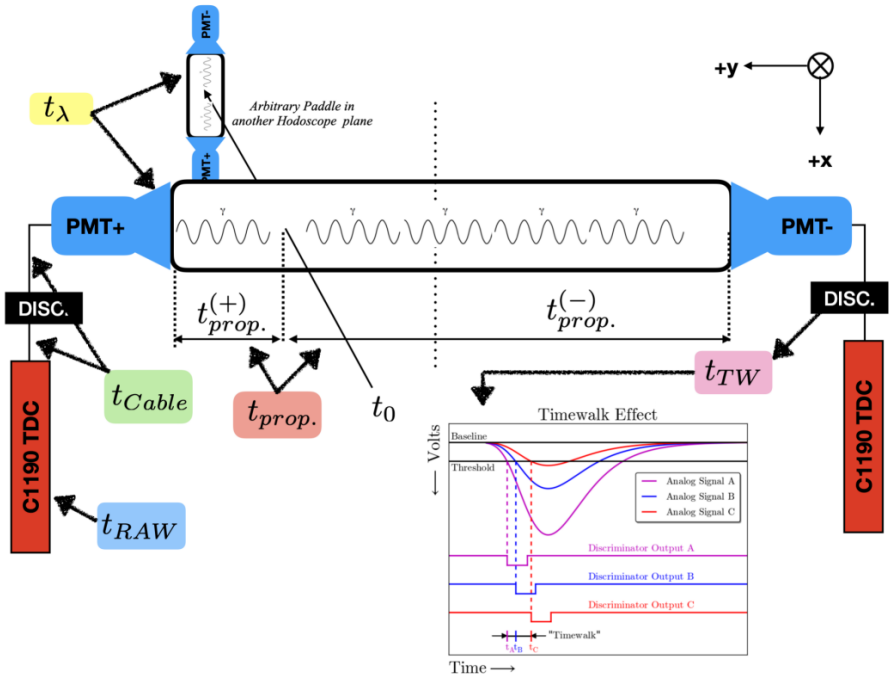


Figure 3.3: Reprint of SHMS hodoscope cartoon [43]. Illustrate of timing corrections applied to each paddle in the hodoscope. Time-walk Effect illustration reprinted from Ref. [43]

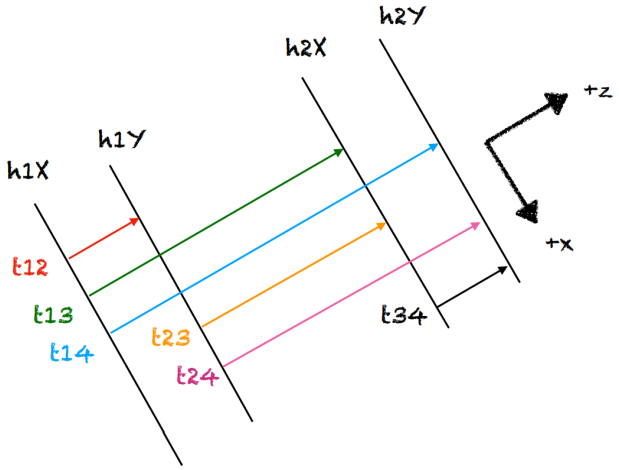


Figure 3.4: Possible hodoscope timing differences between planes, reprint from [43].

In our inclusive experiment, both the pions and electrons are indistinguishable in the hodoscopes and travel at $\beta \approx 1$. Although our final electron yield does not directly depend on the non-tracking β distribution, the timing corrections are applied to get good calibrations in other detectors. Figure 3.5 illustrates the β distribution before and after calibration.

3.1.4 Čherenkov Calibration

Gain matching was performed on each PMT in the Čherenkov detector to ensure that for a given signal, the same response was observed for each PMT in the detector. After a hardware (high voltage) gain match was performed, a software calibration was performed such that the charge output from the PMTs (pC) corresponded with the number of photoelectrons for an event. When the single photoelectron peak is observable in the ADC, a simple mean weighting can be applied to the output signal to get the number of photoelectrons.

$$n_{pe} = C \cdot ADC_{raw}, C = \frac{1}{\mu} \tag{3.3}$$

When the single photo-electron peak is observable, the calibration is simply the mean of a gaussian fit to the single photoelectron peak. This is how the SHMS heavy gas Čherenkov (HGC) is calibrated, but the HGC was not used for this experiment because of a large hole in the center of the acceptance. The single photoelectron peak is not visible in the SHMS noble gas Čherenkov (NGC) distribution, so a secondary calibration technique is employed.

An electron sample was selected by moving the spectrometer to a clean part of phase space (minimal pion background). The distribution of events follows a Poisson statistics extended to a continuous distribution with a normalization to the number of events used.

$$f(x) = A\frac{(\lambda/\mu)^{x/\mu} \cdot e^{-\lambda/\mu}}{\Gamma(x/\mu + 1)} \tag{3.4}$$

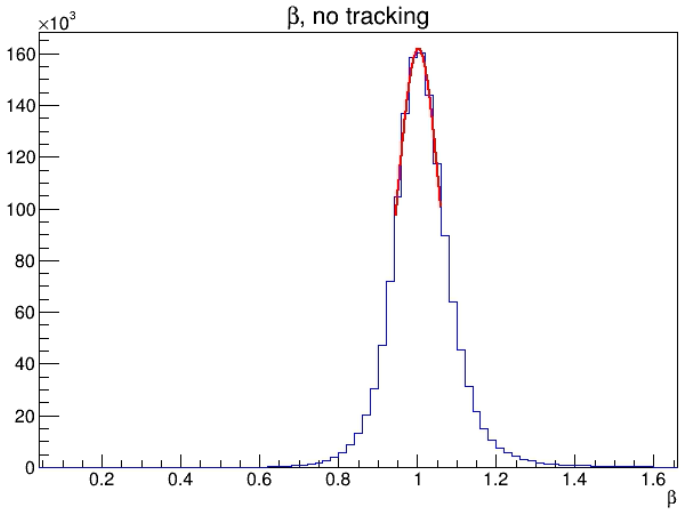


Figure 3.5: Beta distribution from the hodoscope without tracking from the drift chamber. The spread in β away from 1 is primarily due to timing resolution of the hodoscope.

A geometrical cut using coarse track information is placed on each mirror of the NGC and a multiplicity cut of 1 is applied. Using events with a single hit (multiplicity of 1) is ideal since it ensures it is associated with the physics trigger. The fit is extracted and a set of calibration coefficients for each PMT is applied in software. Figure 3.6 shows the fit results on PMTs 1-4 in the noble gas Čherenkov.

This process is complicated by the fact that PMT1 is quite noisy, so a multiplicity cut of 1 removes nearly all real events. For PMT1, the multiplicity cut was removed and a calibration constant was obtained albeit with a larger error bar.

There is an additional level of systematic error added to the calibration process for SHMS NGCER. The SHMS NGCER was used to select electron events. At the kinematics of interest for SRCs, it has been shown that there is minimal pion contamination[31]. The SHMS calorimeter is quite good at separating the pion background from the electron signal as will be shown in the next chapter.

3.1.5 Drift Chamber Calibration

The drift chambers provide tracking information for charged particles. The arrival time of multiple current pulses is recorded by a 16-channel multi-hit TDC card. The timing information from the hodoscopes is used in combination with the arrival time of hits on individual drift chamber wires to convert raw TDC time to drift time via equation 3.7.

$$t_D = (t_{meas} - t_{REF}) - [(t_{wire} + t_{cable}) - t_{REF}] \tag{3.5}$$

This provides course track information in combination with the position of wires in the drift chamber. The full resolution of the drift chamber is realized by using multiple drift chamber planes and knowledge that the distribution of events in a single drift cell as described below.

The position of a hit in a drift plane can be further refined by creating a time-to-distance lookup table from a collection of events that hit a wire in the drift chambers. Drift chambers are designed such that a uniform distribution of events pass through a

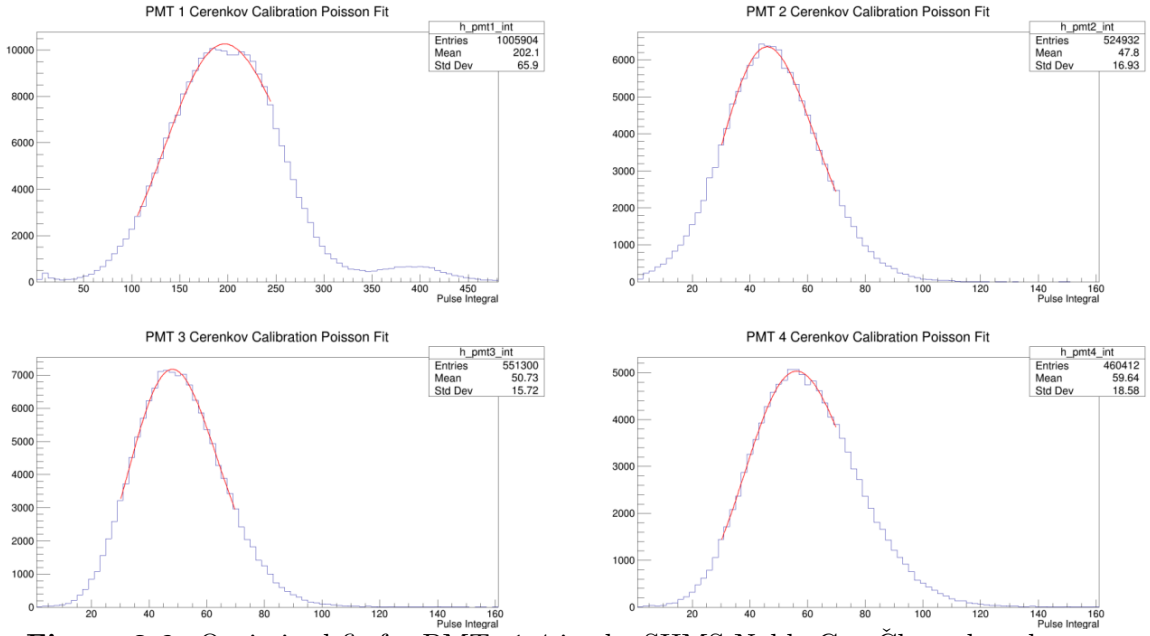


Figure 3.6: Optimized fit for PMTs 1-4 in the SHMS Noble Gas Čherenkov detector.

drift cell. First, the zero crossing of the drift-time is corrected for each TDC for each card in the drift chamber shown in figure 3.7. The zero crossing is set for each card separately because of some time differences between cards. In the edges of the drift chamber, an average is used within a card since the edge wires see far fewer events and skew the distributions, see figure 3.8.

Once the t_o time is determined, a lookup table is created for each wire. There exists some function of drift time $f(\tau)$ such that a particle can be detected some distance away from the sense wire. In the case of the SHMS and HMS drift chambers, this distance is 0 t0 0.5cm. The distribution of events is uniform across the cell. The lookup table is constructed by solving equation 3.6 for a collection of events.

$$\frac{\sum_{bin(t_o)}^{bin(t_o+T)} f(\tau)\Delta\tau}{\sum_{bin(t_o)}^{bin(t_o+t_{max})} f(\tau)\Delta\tau} \rightarrow \frac{1}{N_{tot}} \sum_{bin(t_o)}^{bin(t_o+T)} f(\tau) \tag{3.6}$$

Additional details for calibrating the drift chamber are found in the calibration document.

Tracking Algorithm

For the high-rate physics, there can be multiple tracks in the drift chamber, but only one of those tracks is associated with the physics trigger. A tracking algorithm is used to determine the true track for an event based on given physics quantities. This is known as the pruning algorithm and is required for $x > 1$ physics tracking.

Tracks are formed from what are called track stubs, which are a combination of N hits in both drift chambers. When multiple hits are found in the drift chambers, all possible tracks are made in combination with the hits. Not all of these hits are well formed since at high rates, some noise can be detected. All possible tracks are categorized based on the chi-square fit of hits to a linear track. In the pruning algorithm, additional cuts are selected to remove the poorly formed tracks. Only a

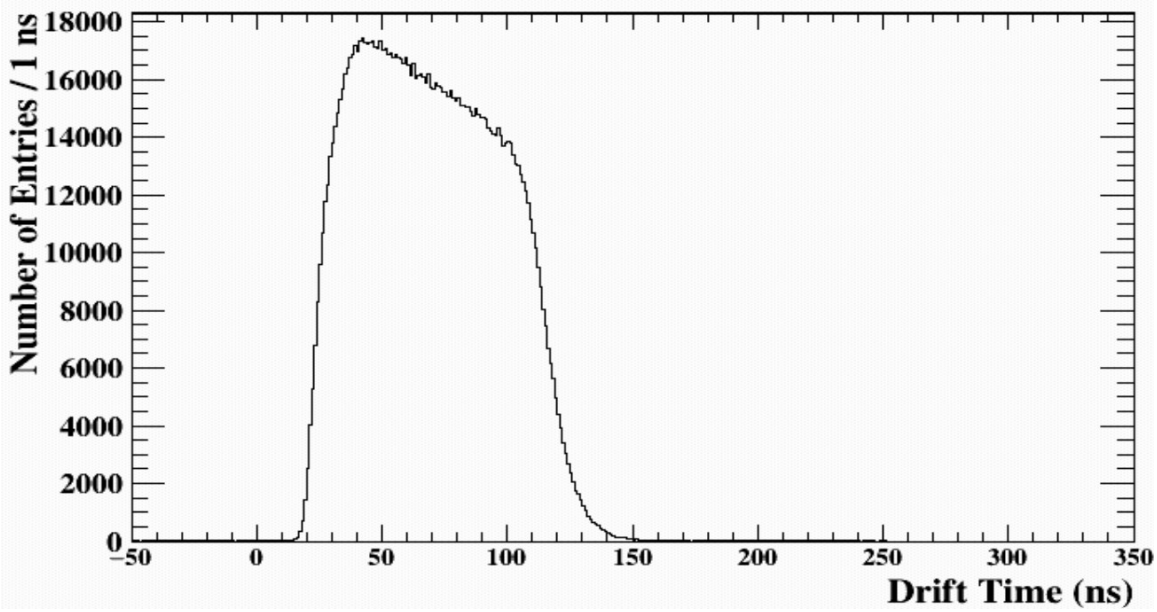


Figure 3.7: The raw drift time is shown in nanoseconds relative to the reference time subtracted start time. The start time is determined by fitting the steep rise in events.

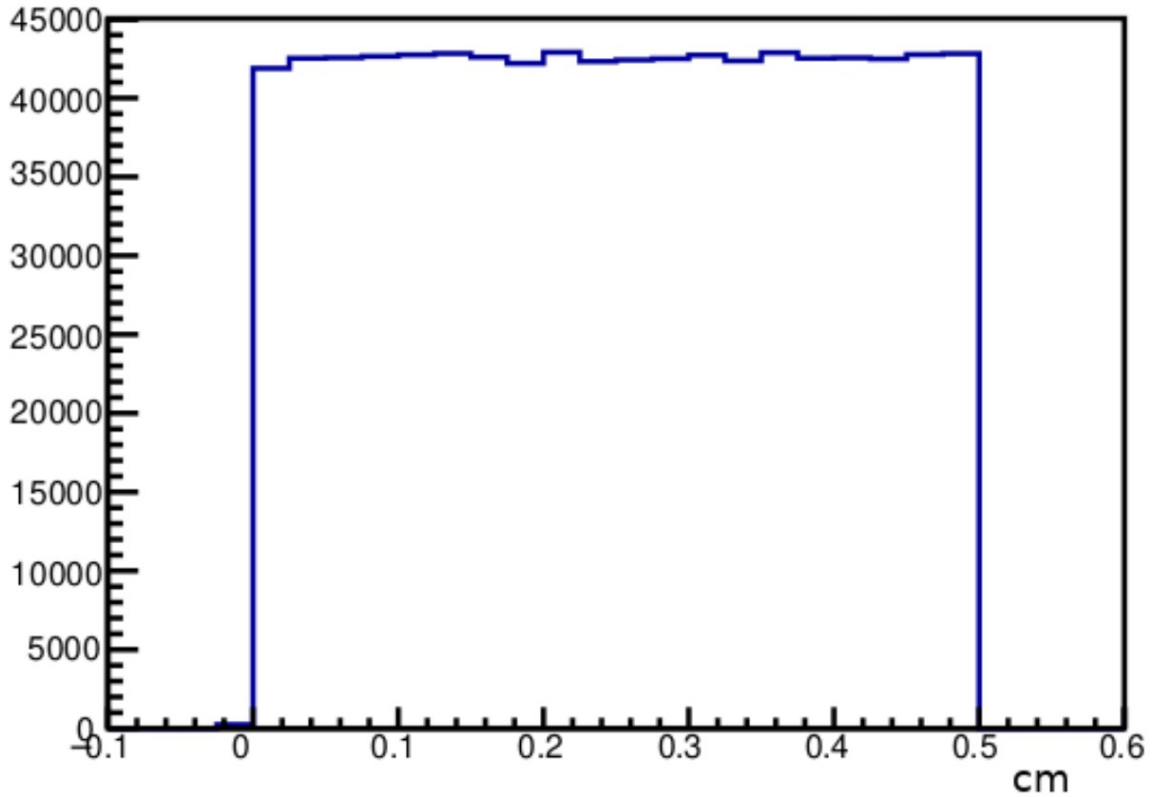


Figure 3.8: The arrival times are converted to distances by way of a time-to-distance lookup map. The uniform distribution of events is shown in centimeters for plane 1U1.

single track is selected based on the remaining tracks based on the track with the best chi square.

3.1.6 Calorimeter Calibration

The calorimeter is used to distinguish between pions and electrons (Particle ID) in this experiment. The particle ID is determined from the energy deposited in a cluster of lead-glass blocks associated with the track selected from the drift chambers. The energy deposited is normalized to the track momentum. Each block has either one or two PMTs attached, which had their high voltages matched to ensure a uniform trigger is formed across the calorimeter (used to form EL-REAL and EL-CLEAN trigger). Gain variations are seen across the acceptance since particles with lower momentum strike the top of the calorimeter and those with higher momentum strike the bottom (bent in the dipole). This is corrected in software by applying a software gain correction across each of the calorimeter blocks. There is a second correction for the light attenuation across the y direction of the blocks.

$$\epsilon_i = c_i \cdot (A_i - A_{ped}) \cdot f(y) \tag{3.7}$$

In equation 3.7, the $f(y)$ captures the variation across the non-dispersive (horizontal) direction, A_{ped} is the background noise on the PMT, and c_i is the software gain correction for the i-th block. The software gain correction for each block is found by minimizing the variance in total energy deposited in all blocks relative to the energy deposited by an incident electron. This is accomplished by single-value decomposition. Figure 3.9 is an example of the calorimeter calibration output. It can be seen from the plot that electrons are normalized to an energy of 1 while pions deposit significantly less energy, but with a long tail slipping under the electron distribution. It is important to characterize the pion contamination in the electron signal to properly extract the electron scattering cross-section for an event. This is described in the following 3.5.1 section. In the $x > 1$ experiment, the face of the calorimeter was

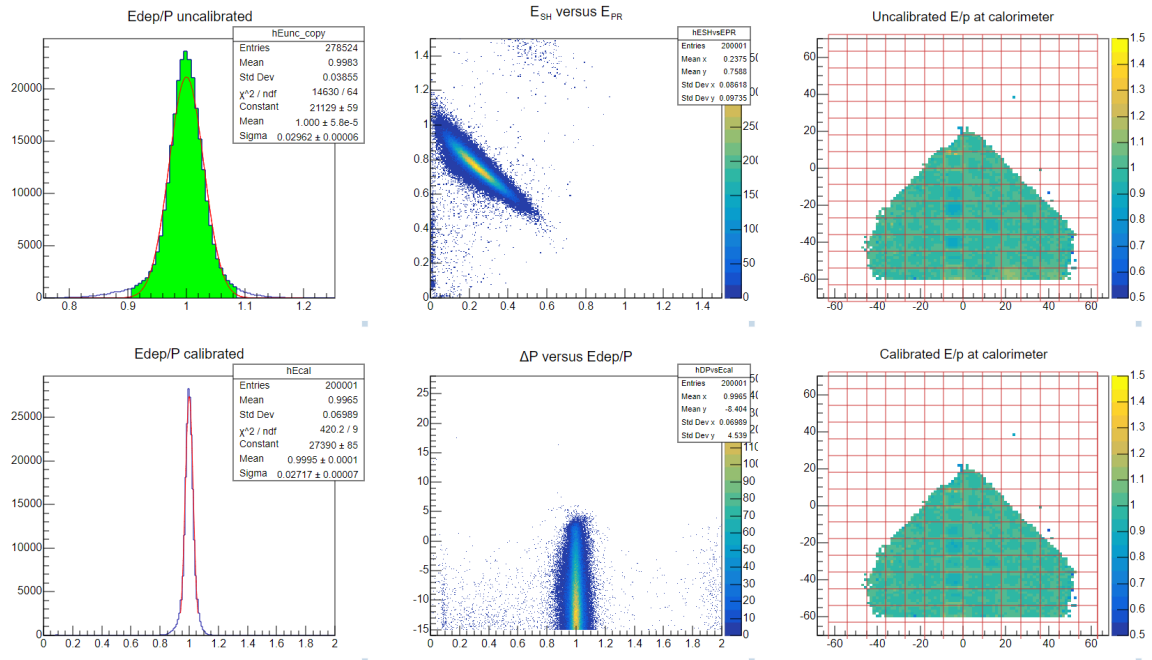


Figure 3.9: Output from the calorimeter calibration script, which applies a software gain correction to correct differences in gain between blocks. Top left: The starting distribution of energy deposited per event normalized by the drift chamber track momentum. Top middle: The distribution of shower and pre-shower energy deposited. Top right: The uncalibrated energy deposited per event extrapolated to the face of the calorimeter from the drift chamber track. Red grid markers depict block locations. A heatmap value of 1 specifies the relative energy yield for a specific event. Bottom left: Calibrated energy deposited normalized to track momentum for electrons. Bottom middle: The energy deposited normalized by track momentum shown against electron momentum. A straight line at one signals no issue in the calibration with respect to momentum. Bottom right: Same as top right, but with the new calorimeter gain coefficients applied.

not entirely illuminated because the higher regions of the calorimeter are physically forbidden. This had an adverse effect of shifting the calorimeter calibration and failing to calibrate some blocks at the edges of the acceptance. In the $x > 1$ experiment, the goal is to measure the electrons at the very edge of the physically forbidden zone, so the variation in gain lead to issues calibrating the calorimeter. Figure 3.10 shows the deviation from Gaussian the electron calorimeter distribution had for the 2018 and 2019 data. This was corrected in the full experiment by taking a devoted defocused Q2 run that scattered electrons across the face of the calorimeter. This calibration lead to much better characterization of the block-by-block gain coefficient.

3.2 Computer and Electronic Dead Time

Dead time is the time after each accepted event in which the detector system is unable to record another event. Figure 3.11 illustrates the dropped pulses due to the DAQ being dead, where τ is the time the DAQ is dead after an event is recorded. The dead time for a Poisson process with input rate ρ and output rate R is given as:

$$\frac{R}{\rho} = \frac{1}{1 + \rho\tau} \tag{3.8}$$

This is only the case for a non-extended system, but most systems now utilize a buffer to write events to disk. The buffer allows the computer to write data while no new events are coming into the system. The dead time is typically split up into two components, the computer and electronic dead time. Computer dead time refers to the time required to readout and store the data from the DAQ, which in most cases makes use of a buffer. Electronic dead time typically refers to the combination of all other dead times including intrinsic detector dead time, front-end electronics dead time, DAQ dead time. The time the DAQ is dead is sometimes referred to as the double pulse resolution, τ. For high rate experiments such as this one, the dominant dead time is the computer dead time, which is constrained by the write speed to disk.

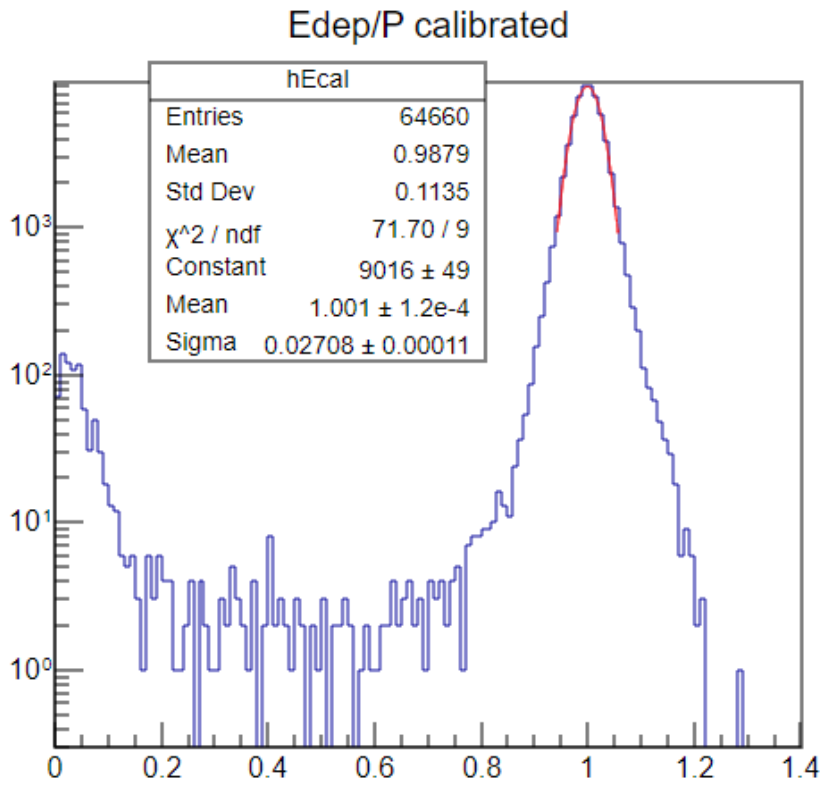


Figure 3.10: Shoulder from 1.1-1.2 in the energy deposited for electrons in the calorimeter. Likely cause is by incorrect gain coefficients.

Second order dead time effects in the logic chain are ignored here, but they may be important at extremely high rates.

3.2.1 Total Dead Time and the EDTM System

The electronic dead time monitoring system (EDTM) was implemented during the 12 GeV upgrade, which was modeled after a similar system used in Hall A. In this method, a clock pulse is injected into the trigger logic with a known frequency. The clock pulse is indistinguishable from a real trigger and can be blocked when the DAQ is busy. The trigger is split into its own TDC and scaler. Since the EDTM pulse is a clock, the scaler will count all events sent (no events are blocked). This method measures the total dead time, and not the separated electronic and computer dead time. Live time is simply the time the DAQ is alive $L = 1 - D$ The total live time for with no pre-scale is given in 3.9:

$$L_{EDTM} = \frac{S_{EDTM}}{T_{EDTM}} \tag{3.9}$$

The EDTM system does not measure the dead time it introduces to the system. The EDTM rate is set to the minimum possible value to have a reasonable uncertainty while avoiding unmeasured dead time. Given the DAQ dead time is around $250 \times 10^{-6} s$, an EDTM rate of 100Hz introduces an unmeasured dead time fraction of about 0.025 [44]. The uncertainty on total live time is reduced by taking longer runs and maintaining a given DAQ rate (maintain the same current). It is important to note the non-Poisson behavior of the EDTM pulses is not a significant difference when the EDTM rate is much lower than the physics rate. An added complication is the introduction of a pre-scale factor (PSF) and multiple trigger types as discussed in 2.6. Each trigger leg can have its own pre-scale value and thus events of that type are skipped accordingly. The total live time with a single trigger and a single pre-scale

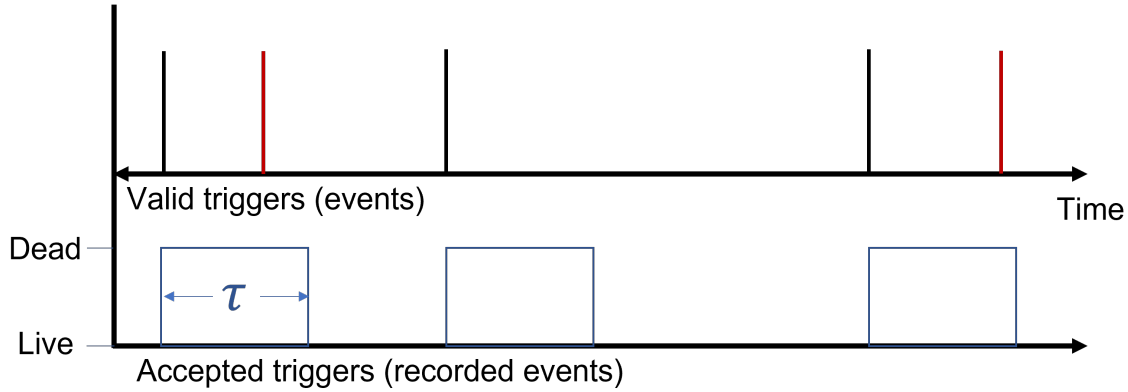


Figure 3.11: Illustration of accepted triggers compared to the valid triggers formed in the logic chain. Only three events were accepted in this example, so the dead time is 60%.

is given in 3.10.

$$L_{EDTM} = \frac{S_{EDTM}}{C \cdot T_{EDTM}} \tag{3.10}$$

Where C is the $1/PSF$. When multiple triggers are active, the weighting of each trigger leg is required. This leads to additional terms being added to C. Additional cuts on trigger type are also necessary, and the electronic dead time is non-trivial [44]. For this reason, only one trigger type was used for all production running for all XEM2 experiments.

3.2.2 Computer Live time

The computer live time simply refers to the time the DAQ is busy writing events to disk, which is by far the longest operation in any modern DAQ system. The DAQ was always running in buffered mode, which increases the number of events written to disk significantly. The computer live-time can be measured using the total number of triggers written compared to the total number of scalers.

$$C_A = \frac{T_{TRIG}}{S_{TRIG}} \tag{3.11}$$

To measure the computer live time for physics triggers, the number of EDTM events must be removed from scalers and triggers.

$$C_P = \frac{T_{TRIG} - T_{EDTM}}{S_{TRIG} - S_{EDTM}} \tag{3.12}$$

3.2.3 Electronic Dead Time

The electronic dead time can be extracted with knowledge of the total dead time and computer dead time using the EDTM system, scalers, and triggers. If the EDTM system is not set properly, as the case in 2018, the electronic live time cannot easily be obtained. Hydrogen elastic data was used to show that there was significant electronic dead time for in the 2018 runs. A combinatorial model was used to estimate

the electronic dead time. In this model, the scaler rate was combined with knowledge of the logic node's double pulse resolution. In this method, every combination of pre-trigger and trigger is analysed to determine the total contribution to electronic dead time. As an example, the hodoscope has 4 planes that can be combined to form the 3/4 trigger. Every combination of these planes has a scaler rate and dead time associated with it. The product of each weighted dead time gives the total dead time. This model was initially made by Dave Mack and I expanded it to work for the EL-REAL trigger[45]. An additional correction was applied because one cannot assume the planes fire randomly as they are correlated by events coming from the target. Figure 3.12 shows the electronic dead time model as a function of 3/4 trigger rate. It was difficult to validate the electronic live-time model because there was no other high-rate running taken during this period and the trigger was improved to have less electronic dead time shortly after. Figure 3.13 shows the agreement between hydrogen elastic and monte-carlo after electronic live time correction. The momentum saturation in our experiment combined with optics mis-setting made the validation with hydrogen elastics impossible.

3.2.4 Live Time Systematic Errors

Systematic error on the measurement of computer live-time is negligible. This is due to the sample size for triggers to scalers being extremely large for all runs. The systematic on the electronic live time is much harder to quantify given the simple dead time model used. The maximum S1X rate of the 2019 dataset was 400kHz. At this rate with 50ns gate widths, the electronic dead time is nearly zero. Given the simple model, a scale uncertainty of 0.1% was assigned. A linear rate dependence was used as a function of S1X rate as shown in Figure 3.14. Although the model does not perfectly fit the data, the point-to-point error on the electronic live time is less than 0.05% between runs. The updated EDTM system used for the full running will provide improved quantification of electronic dead time.

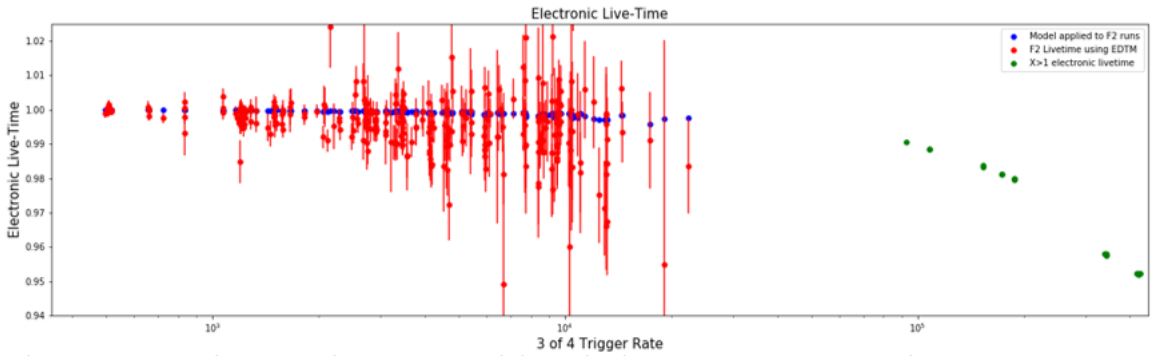


Figure 3.12: Electronic live-time model applied to F2 experiment and $x > 1$ experiment. Red points is electronic live time measured using the EDTM.

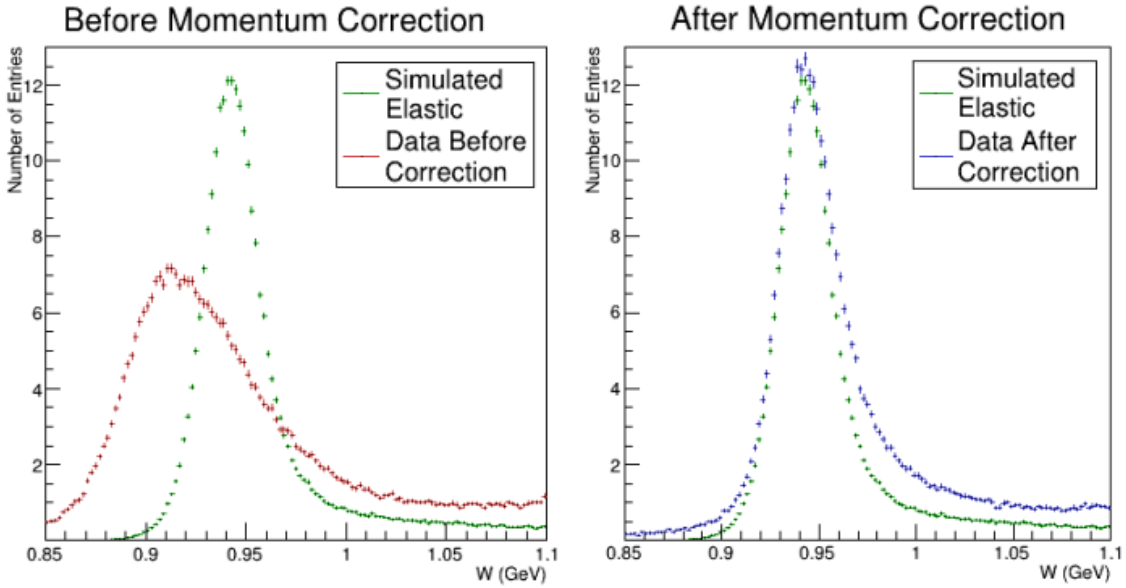


Figure 3.13: Hydrogen elastic data compared to SIMC. Agreement was observed in the the elastic peak after a momentum and ytar correction were applied. Separation of these two effects with a high degree of accuracy is not reasonably achieved.

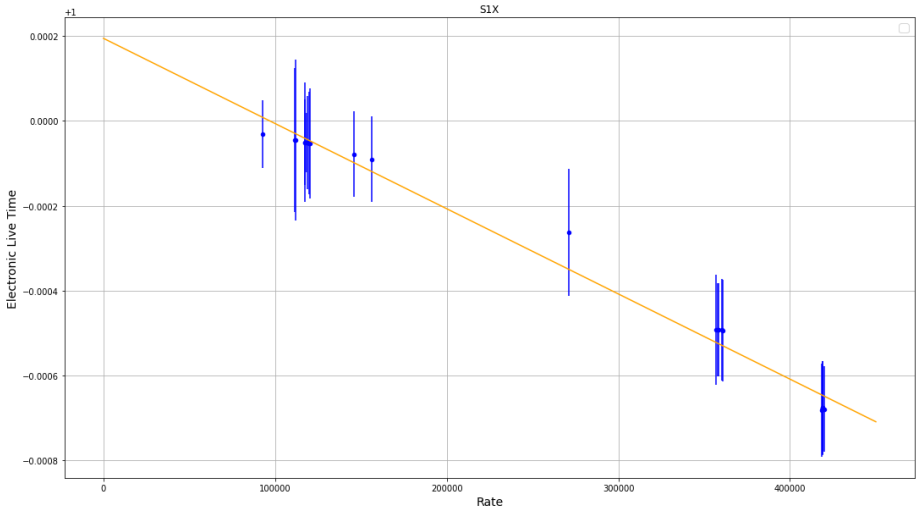


Figure 3.14: Linear fit to electronic live time model to calculate systematic error. A linear model is not ideal, but the electronic live time is so high any improvement to the dead time model has negligible benefit.

3.3 Optics and Offsets

The SHMS was installed and commissioned in 2017/2018 and optics checks were performed[46]. A series of field measurements were performed before installation of the SHMS quadrupole and dipole magnets. A field setting program is used to set the magnet to the desired field strength based on current. Saturation occurs in the magnets where a further increase in current does not lead to an increase of magnetic flux, though the flux will tend upward from paramagnetism. The field setting program is designed to account for saturation effects in the magnets to reach the desired field setting. While the field measurements indicated a need for a saturation correction in SHMS Q3, it was later found through elastic scattering data that a momentum saturation was not required for Q3 and the saturation for Q1 was modified. These quadrupole magnets focus the scattered particles in the dispersive direction, so any offset in their field causes the momentum distribution to be skewed. As long as the field setting for each magnet is in agreement with the other magnets, only a shift in central momentum is observed. Anything over $8.5 GeV/c$ needs to be studied for changes to the central momentum and focusing of the magnets. Unfortunately, the SHMS magnets were set with inappropriate saturation during the 2018 running which caused not only a momentum shift, but a distortion of the focus in y_{tar}. Figure 3.15 shows the distortion W for elastic electrons off hydrogen versus x'_{fp}. One would expect the distribution of elastic events to be independent of the x'_{fp} and δ. A second order polynomial correction to the momentum was applied in an attempt to correct for the mis-set optics.

$$\delta_c = \delta + 11.5 * x'_{fp} + 200.0 * x'^2_{fp} \tag{3.13}$$

All subsequent data cross-sections reported are from data taken opportunistically over a two day period in 2019. By this point, the SHMS Q3 offset was corrected and the momentum saturation had been characterized. A central momentum offset was noted, but since all of the optics elements were in agreement, this corresponds to a simple shift in the central momentum. The central momentum for the full

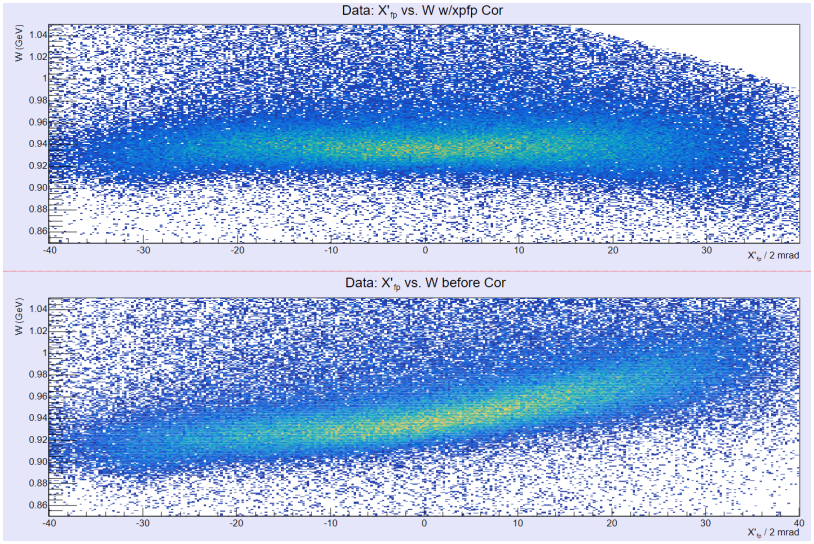


Figure 3.15: An attempt to correct for saturation effects in the quadrupole magnets for 2018 data. One would expect no focal plane dependence in W for hydrogen elastic events. A 2nd order polynomial fit was applied to the raw data (bottom). The top figure shows the corrected W distribution versus the focal plane quantity, X'. The uniqueness of this correction could not be determined.

experiment was reduced to 9.2GeV/c to minimize the effects of saturation on the magnets. Although the 2018 data was unrecoverable because of the optics issues and unmeasured electronic dead time, we learned many things that helped make the full experiment that ran in 2022 a success.

3.3.1 Momentum Offsets

In 2019 the SHMS optics were aligned, but were not corrected up to $9.8 GeV/c$. In order to determine the central momentum, a series of single-arm hydrogen elastic measurements were made at $8.5 GeV/c$, $9.0 GeV/c$, and $9.5 GeV/c$. A Monte Carlo simulation tool called SIMC was used as 'truth' data to compare the hydrogen elastic data. More details of the Hall C Monte Carlos are found in 4.1.2. Figure 3.16 show the comparison between data and SIMC and the required momentum offset to achieve agreement. The central momentum was determined for each setting and is given in table 3.1. There is linear magnet saturation evident in the magnet settings. The central momentum at the true setting was extrapolated since no hydrogen data was taken at this setting. There is still some possibility of mis-alignment in the optics. A 1% scale uncertainty was assigned to our ability to set the central momentum. Additionally, a 0.2% point-to-point uncertainty was set for setting the central momentum.

3.3.2 Spectrometer Offsets

The position of the target, magnets, beam components, and spectrometer detectors are determined relative to each other by the Survey and Alignment group at JLab. The SHMS magnet position relative to the central pivot has been measured several times at the same SHMS angle setting. A vertical displacement of 1 mm has been observed in the SHMS magnets relative to the central pivot at small angles. The path length of charged particles through the SHMS magnets is altered by the small vertical displacement. Ideally the spectrometer would not be moved during the entire run, but

Table 3.1: Set Momentum and True momentum setting from hydrogen elastic data

Set Momentum	True Momentum	Percent Offset	Measured
$8.5GeV/c$	$8.454GeV/c$	0.54%	Yes
$9.0GeV/c$	$8.942GeV/c$	0.64%	Yes
$9.5GeV/c$	$9.431GeV/c$	0.73%	Yes
$9.8GeV/c$	$9.723GeV/c$	0.79%	No

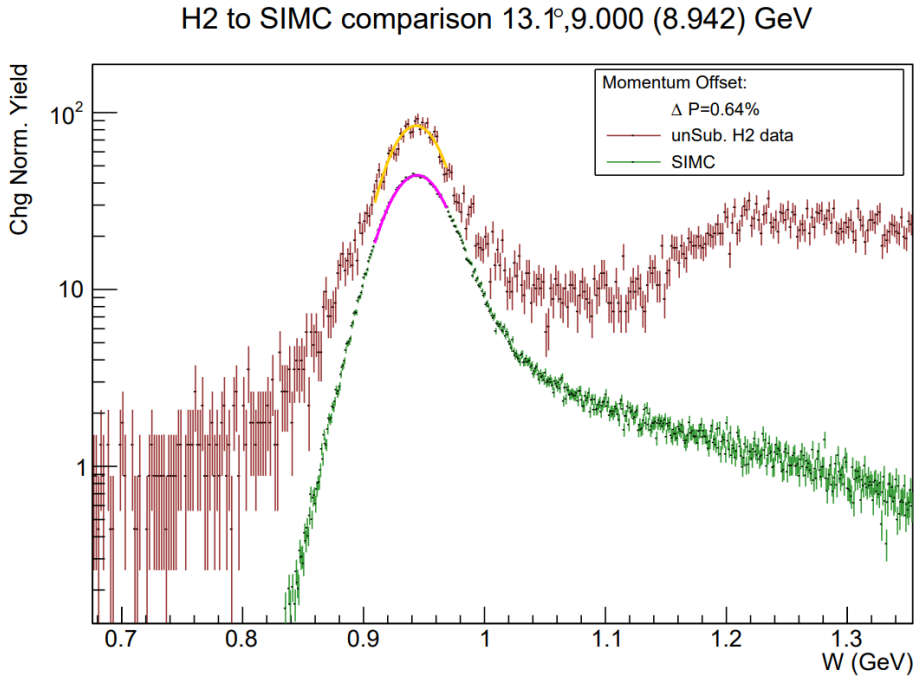


Figure 3.16: The central momentum offset for a central momentum setting of $9.0GeV$ is 0.64% lower than the set momentum.

that is not always possible. The SHMS was rotated from 13.100° to 25.0° and back to 13.100° during the spring 2019 run period. A discrepancy in the charge normalized yield prompted a multi-month investigation into the cause of the difference in charge normalized yield. The difference in charge normalized yield was determined to be due to changes in the vertical offset of the magnet elements. The difference in yield observed of 6% is corrected for by offsetting the central momentum on the second day by 0.2%. The single-arm Monte Carlo was ran with a 1 mm vertical offset and the discrepancy went away. Based on the long investigation, we are 75% confident that the cause of the discrepancy is the reproducability of the SHMS magnets. A systematic uncertainty of 2% was obtained determined from this procedure.

3.4 Efficiencies

The detectors and triggers of the SHMS do not fire for every and all events that pass through it. The detectors were designed with this in mind, and redundant systems are in place to measure the absolute efficiency of detector components. Electron detection efficiencies are determined for the noble gas Čherenkov, calorimeter, and drift chambers. The efficiency of the trigger is also determind.

3.4.1 Noble Gas Čherenkov Efficiency

A sum of 2 photoelectrons was required from the Čherenkov detector to accept good electrons in our analysis. This will remove some number of good electrons, and cause an inefficiency. By selecting a pure sample of electrons without the Čherenkov, we can determine the inefficiency of the detector.

$$\epsilon_{cer} = \frac{N_{all}}{N_{EL_HI}} \tag{3.14}$$

The EL_HI trigger requirement is more strict than the EL_LO and CER trigger leg. This efficiency is calculated where the electron sample is small. Elastic runs from

previous experiments were also used. A delta dependence was observer on the on the efficiency. A one-dimensional fit of efficiency vs. delta was used as shown in figure 3.17. The Čherenkov efficiency was determined in our sister experiment and first reported here [47]. A point-to-point systematic uncertainty of 0.2% was assigned to the delta dependent Čherenkov calibration.

3.4.2 Calorimeter Efficiency

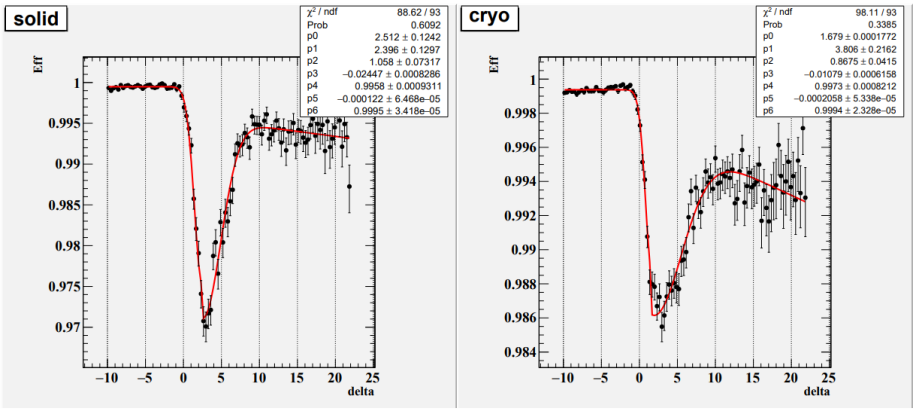
The calorimeter is used in combination with the noble gas Čherenkov to separate pions from electrons. A cut of $E_{cal}/E' > 0.7$ is used in the analysis, which will remove a small sample of good electrons. A pure electron sample is made without explicitly cutting on the calorimeter. Elastic electron scattering was used to determine the calorimeter efficiency because additional kinematic cuts can be used. An invariant mass cut along with particle velocity, β, is used from the drift chambers. A more strict noble gas Čherenkov cut is also used. The efficiency of the calorimeter at high momentum was found to be nearly 100%, shown in figure 3.18.

3.4.3 Tracking Efficiency

Tracks are required to form good electron events. The event must not have more than 25 hits in either drift chamber, but must have enough hits to resolve the left-right ambiguity. The tracking efficiency is determined by taking the number of tracks that did form a track and those that should have formed a track.

$$\epsilon_{trk} = \frac{N_{did}}{N_{should}} \tag{3.15}$$

Here, N_{should} is a number of valid triggers that satisfied certain criteria. A good hit is required in the hodoscope with a good beta. Additionally for an electron, energy should be deposited in the calorimeter and a hit should be seen in the noble gas Čherenkov. None of the cuts on good events require a track to be formed. The



(a) (b)

Figure 3.17: Parameterization of the noble gas Čherenkov efficiency as a function of δ. No significant difference between solid targets (left) and cryo targets (right). Reprinted with permission from the author of [47].

Table 3.2: Nominal good electron cuts for tracking efficiency

Variables	Cut
Momentum	-10 <dp <22
Invariant Mass Squared	$0.9 < W^2 < 1.1$
Noble Gas npeSum	npeSum >2
Drift Chamber Particle Velocity	$0.85 < \beta < 1.1$
Number of Tracks	1

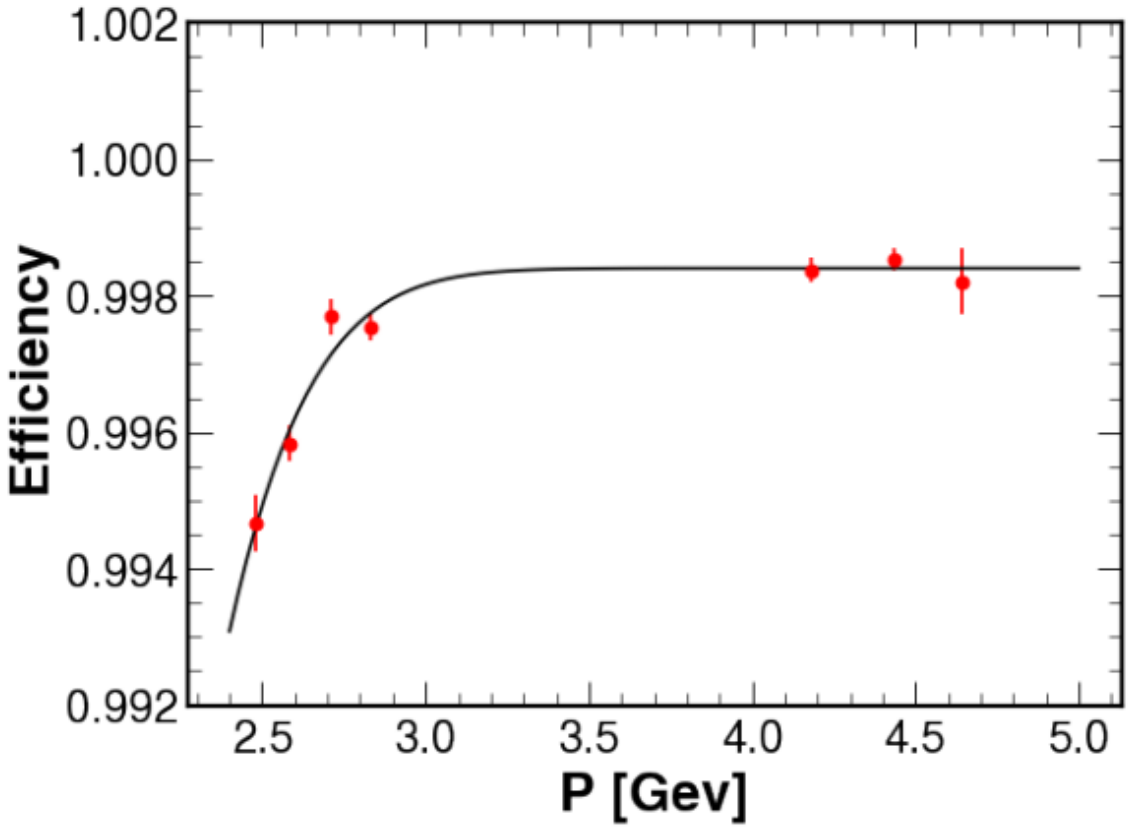


Figure 3.18: Calorimeter efficiency as a function of central momentum. The efficiency approaches a constant value for momentum values relevant for this experiment $P > 8GeV$.

only difference between N_{should} and N_{did} is that one or more tacks must have been formed. The track forming algorithm is not tested in the aforementioned schema. The track forming algorithm is expected to perform adequately in the reconstruction of real and physical tracks. The track selection algorithm used in this experiment is described in 2.5.2. The pruning method was employed for this experiment due to the higher rates experienced. No decrease in tracking efficiency was found compared to the χ^2 minimization method, but more ideal tracks were found. Figure 3.19 shows the tracking efficiency for all runs in the 2019 experiment.

3.4.4 Trigger Efficiency

Not all electron events will trigger the 3/4 hodoscope at all times and this leads to an inefficiency in measuring real electron events. The probability for any hodoscope plane to fire for an electron event is constructed for all events detected. From this distribution, there is 5 ways the 3/4 trigger can fire: P1234, P123, P124, P134, P234 where the numbers represent the planes and P represent probability of firing. A running sum is accumulated for each plane for each event, and the final probability is determined. The 3/4 trigger efficiency was found to be 96%-97% efficient. This was applied on a run-by-run basis. In addition to the 3/4 trigger, electron specific triggers were used to minimize pions firing the trigger. The EL-REAL trigger is the OR of ELLO and ELHI. It was found the efficiency of these legs was 100% efficient. This is to be expected as there are very few pions at SRC kinematics.

Table 3.3: Tracking Efficiency Parameters for Good Electrons

Hodoscope Good Scintillator Hit	True
Hodoscope β no track	$0.8 < \beta < 1.4$
Calorimeter E (normalized)	etotnorm >0.8
NGC npeSum	npeSum >2

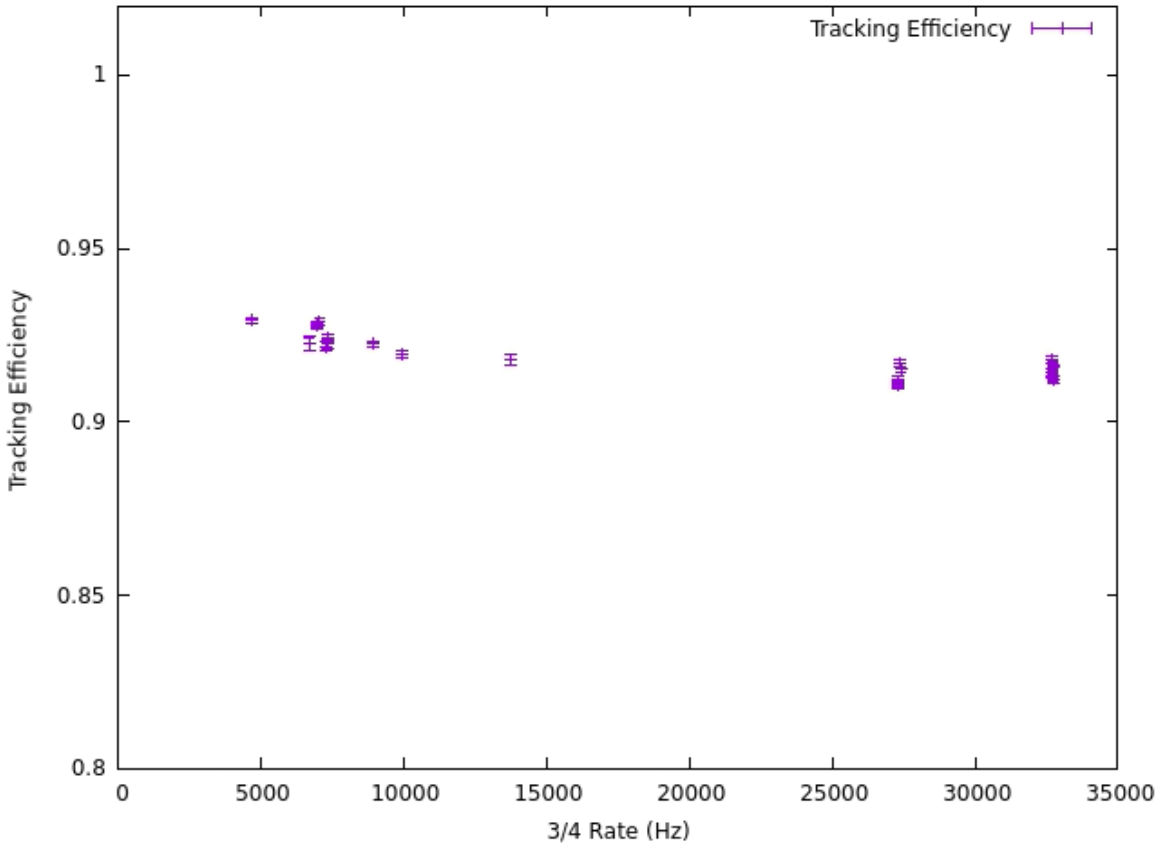


Figure 3.19: Tracking efficiency as a function of 3/4 trigger rate.

3.5 Electron Yield Corrections

3.5.1 Target Corrections

Cryogenic Cell Subtraction

The cryogenic targets are contained within an aluminum cell. The cell walls are 0.1 mm - 0.2 mm thick with a density of $2.7 g/cm^3$. A larger percentage of events come from the aluminum end caps and sidewalls (10-20%). A larger fraction of events come from the aluminum end caps as the liquid deuterium or liquid hydrogen cross-section go to zero. The electron yield from the end caps must be subtracted off, and that is accomplished with a stand-in target made of two slabs of aluminum. The stand-in target is about 2 times thicker than the cryo cells and there is only one to compare to all cryo cells. The two slabs of aluminum are placed ± 5 cm upstream and downstream of the target center to align with the cryo cell end caps. The charge normalized yield for both the stand-in and cryo target is taken and a portion of events is subtracted according to a scaling factor. The scaling factor relates the dummy thickness to the cryo cell thickness, listed in table 3.4. Another reason the aluminum dummy is slightly thicker is the radiation length is approximately equal to the radiation length for cryo targets. This simplifies radiative effects for most settings, but the radiative effects are more significant for $x > 1$ physics. The radiative effects were determined using the radiated cross-section model described in 4.2. The size of the radiative effects is shown in 3.20.

3.5.2 Cryogenic Target Boiling

Since dummy subtraction is so important at high-x, an in-depth study was performed to ensure that contributions from the cryo cell walls were totally removed. A large portion of events come from the dummy cell walls. Although the average aluminum stand-in is 10% of the events, at high-x the aluminum stand-in contributes up to 80% of the events. Our ability to measure the aluminum stand-in thickness relative to the

Table 3.4: Cryogenic Loop and Aluminum Stand-in Parameters

Target	Loop	Ratio $\left(\frac{t_{stand-in}}{t_{cryo}}\right)$
D2	2	4.063
H2	1	3.789

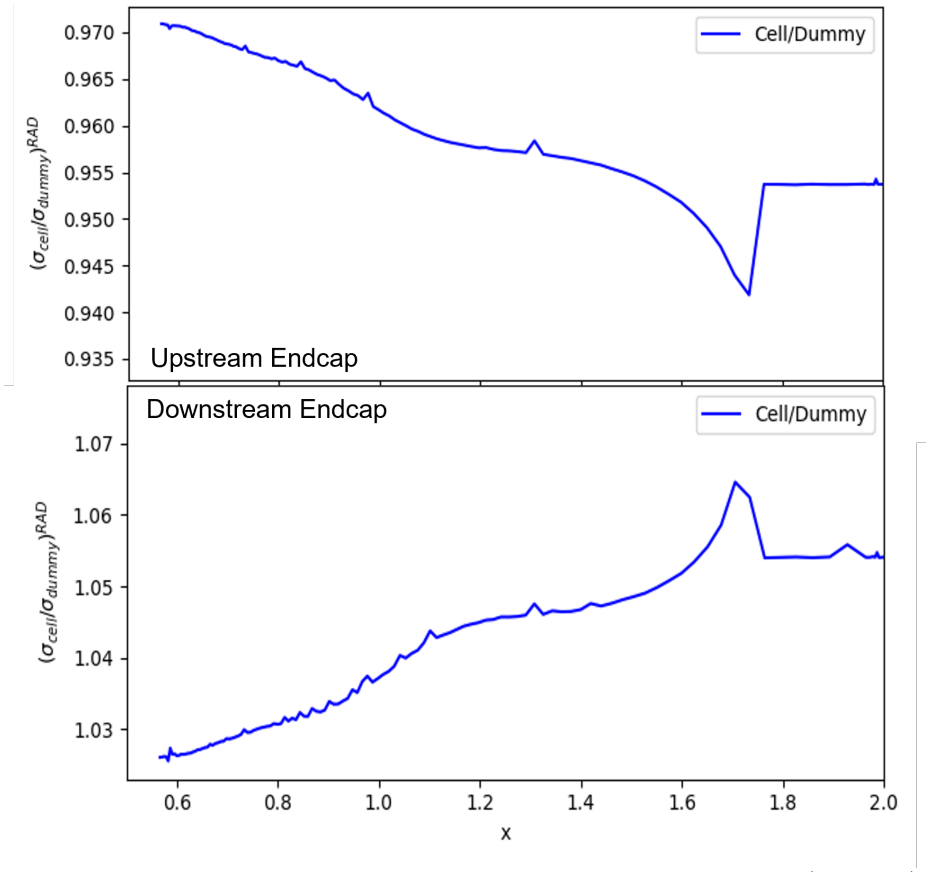


Figure 3.20: Ratio of radiative corrections for aluminum stand-in cell (dummy) and cryo cell. At small angles, the events travel through the downstream end of the target as opposed to the sidewalls. Both are modeled here.

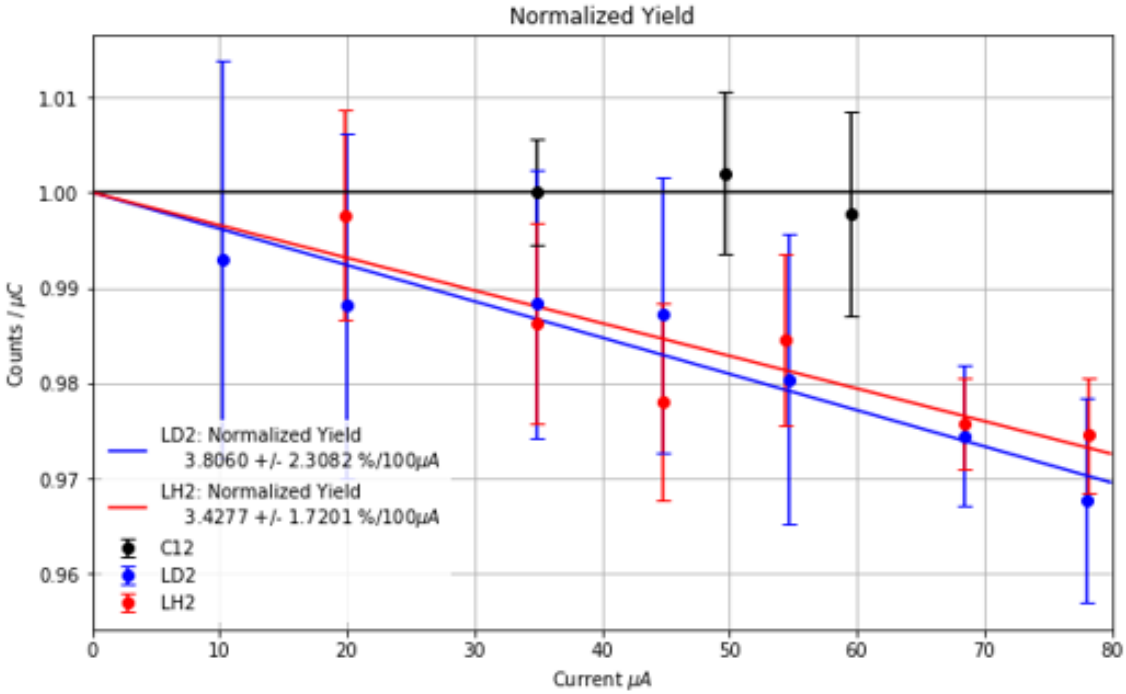


Figure 3.21: Cryogenic target boiling for 2018 run period.

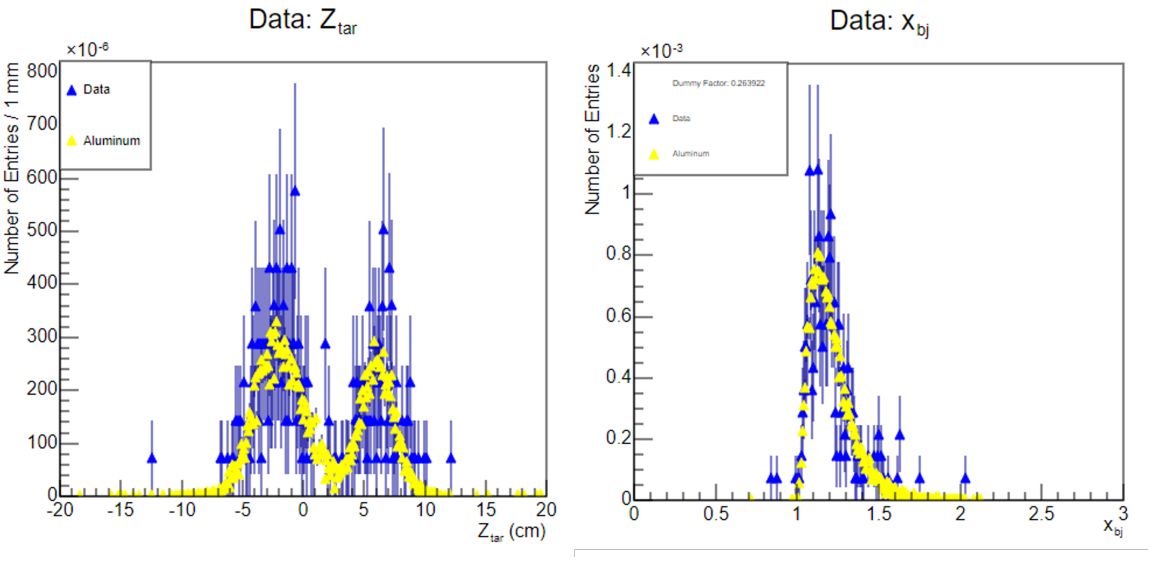


Figure 3.22: Comparison between stand-in target and cryo target with hydrogen. On the left, charge normalized yield vs target position (along beam). Right plot shows agreement between cryo cell and stand-in cell contributions at $x > 1$, which is physically forbidden for hydrogen.

aluminum cryo cell endcaps is used as the systematic uncertainty on the aluminum subtraction. Table 3.4 gives the ratio and measurement uncertainty for the cryo-cell to stand-in target. The aluminum thickness is known to __%. A bin-by-bin correction to the dummy subtraction is determined ranging from 0__% - __%.

Target Thickness Measurement

Target density

The liquid deuterium target is held at 22K and the liquid hydrogen target is held at 19K. Any deviation from this temperature will cause the density to change causing a decrease in the electron yield as described in 2.3.1. The PID loop controlling the target is based on temperature probe 1. During the 2018 run period, the readback temperature between the 5 temperature probes was observed. It was assumed the temperature probe T1 used to PID off of was the accurate model. The same thing was observed in 2019 and 2022. The true temperature of the cryogen as it gives up its latent heat is constant, which gives us a benchmark to calibrate all the temperature probes to. This involves not only the temperature information, but since the pressure may vary, the equation of state for each cryogen needs used. This information is published on the NIST website[48]. Figure 3.23 illustrates the archived EPICS data for the target including pressure and temperature. The temperature offset for several cool-down and warm-up events is given below. The same procedure was performed for both target cells. It was found that half-way through the 2018 experiment, the temperature probe used to PID off of was changed from T1 to T3. Table **??** gives the offsets for each temperature probe given this study for spring 2018 running.

3.5.3 Charge Symmetric Background

High energy electrons have the potential to emit high-energy photons in the target, which can produce electron-positron pairs. Some of the electrons form a trigger and fire off the detector. This is called the charge symmetric background (CSB). At small

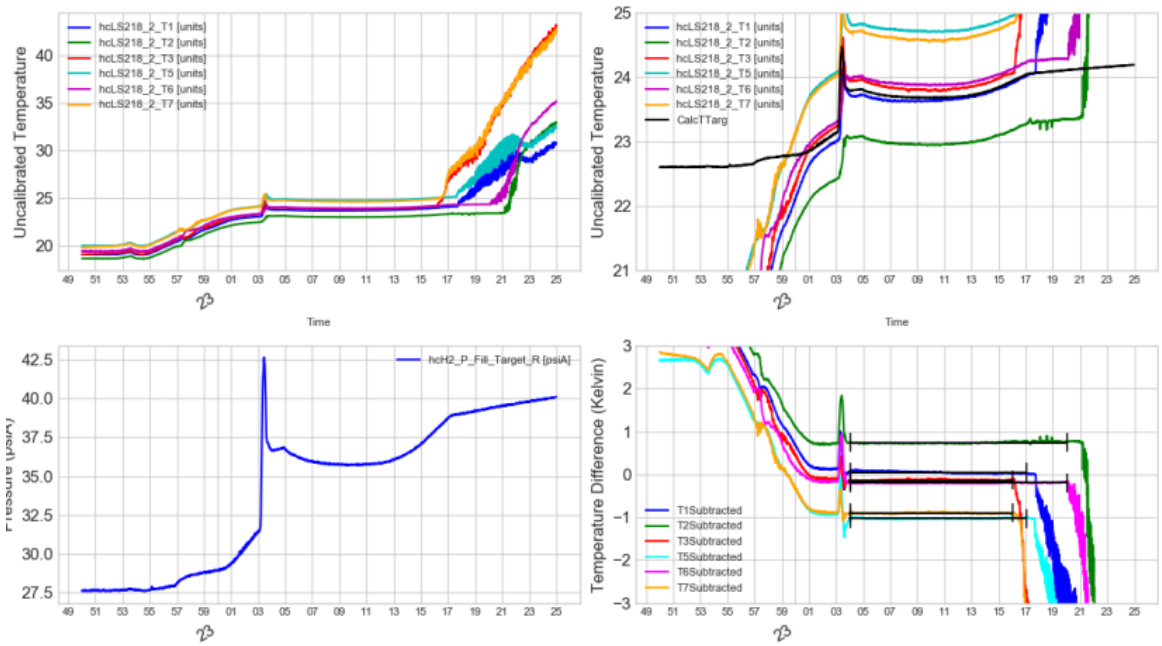


Figure 3.23: Liquid hydrogen. Top right, the uncalibrated temperature probes. Bottom right, region used to calibrate shown in black.

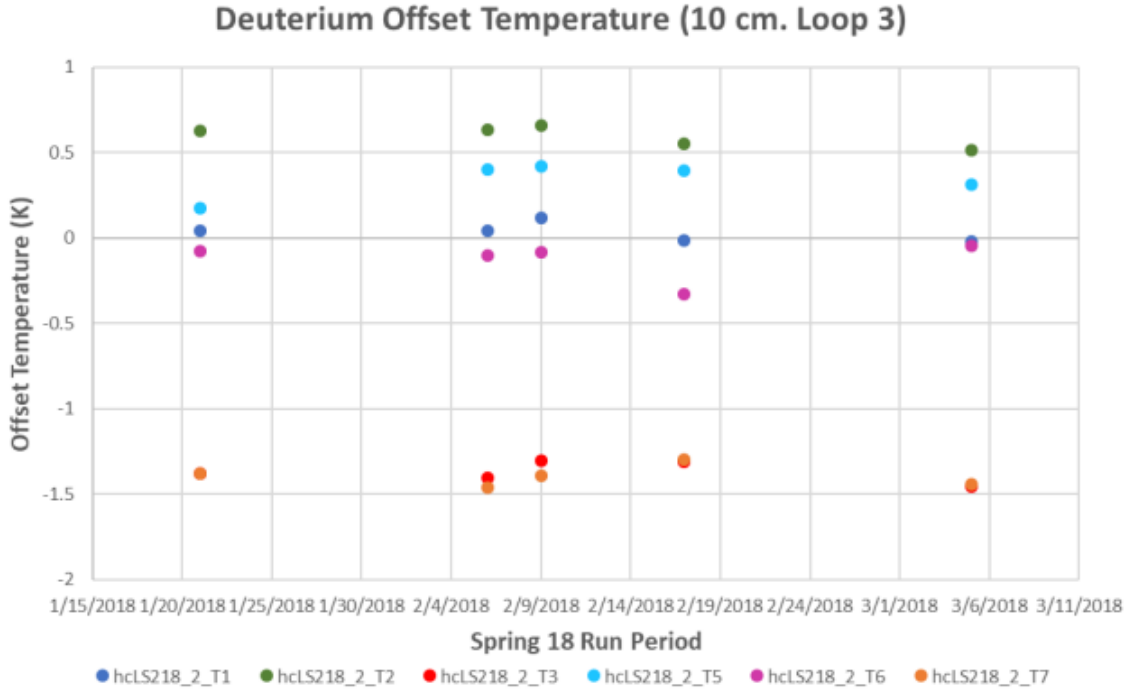


Figure 3.24: Target probe offsets for multiple warm-up and cool-down periods.

Table 3.5: Hydrogen Probe Offsets

Temp Probe	Offset
hcLS218_3_T1	0.070958
hcLS218_3_T2	0.77798167
hcLS218_3_T3	-0.08981
hcLS218_3_T5	-0.958
hcLS218_3_T6	-0.19805833
hcLS218_3_T7	-0.8673275

Table 3.6: Deuterium Probe Offsets

Temp Probe	Offset
hcLS218_2_T1	0.032548
hcLS218_2_T2	0.595358
hcLS218_2_T3	-1.371128
hcLS218_2_T5	0.338468
hcLS218_2_T6	-0.128632
hcLS218_2_T7	-1.394798

angles and high momentum such as the kinematics for this experiment, the positron background is expected to be very low. One way of determining this background is by running the spectrometer in positive polarity at the same kinematics and observing the number of positrons. There is an equal number of positrons created as electrons, $\pi_o \rightarrow 2\gamma \rightarrow e^+e^-$, so the cross section for these reactions is the same. This was measured during the 6 GeV inclusive SRC measurement, which had many more angles and lower momentum. Figure 3.25 shows the measured charge symmetric background for the 6 GeV SRC experiment[31] No charge symmetric background measurement was performed for this experiment since the background was already negligible by 18∘ and $4.43GeV$.

3.5.4 Pion Contamination

Knock-on electrons can be created from pions while passing through the windows of the upstream Čherenkov detectors. The subsequent track in the drift chamber and shower in the calorimeter are a source of background similar to the charge symmetric background. The pions that appear like electrons are called pion contamination. The pions will deposit less energy into the calorimeter than the electron cut will accept, but the tail of this distribution extends into the electron peak. The distribution of pions is assumed charge symmetric, so a study similar to the CSB can be performed for positive pions. The number of pions present inside the electron cut is removed from the electron distribution. No devoted study was done for this experiment, but the previous 6 GeV experiment showed minimal pion contamination at the highest momentum and lowest angle. The pion contamination is also minimized in this experiment because pion production increases with A, the number of nucleons in the target. The thickness of the windows on the SHMS noble gas Čherenkov detector is about the same radiation length as the HMS Čherenkov detector, so the amount of pions produced should be about the same in both spectrometers. No devoted pion contamination study was performed for this experiment. A study of pion

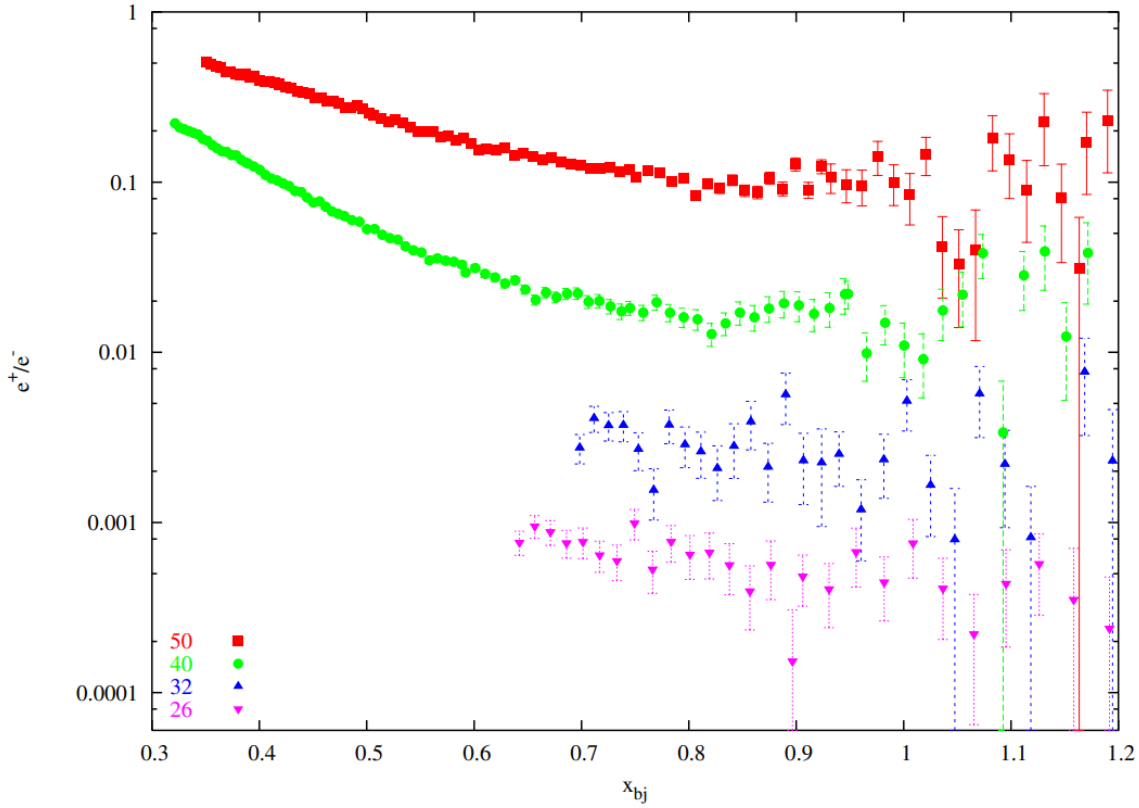


Figure 3.25: Observed charge symmetric background for 6 GeV inclusive SRC experiment, E02-019. Angle setting 18° corresponds with 4.43 GeV, half that of this experiment[31].

contamination was performed for the 6 GeV experiment up to 26° up to an HMS momentum of $4.5 GeV/c$, shown in figure 3.26 Additionally, our sister experiment measured pion contamination up to 5.0 GeV/c. The pion threshold for the gas selected in the noble gas Čhernekov was between 4.2 and 4.6 GeV. Thus, no pion rejection is available for the noble gas Čherenkov above 5.0 GeV/c. Figure 3.27 shows the pion-to-electron ratio as a function of momentum for Carbon and Deuterium. From the figure, the worst case scinario is a flat pion-to-electron distribution above 5.0 GeV/c for both Carbon and Deuterium. A 0.3% systematic error was used as a conservative estimate.

3.5.5 Charge Normalized Yield

Once all efficiencies and corrections have been determined, one can obtain the charge normalized yield of electrons, which is the total number of electrons that pass the 'good' electron cuts corrected for detector efficiencies and normalized by charge:

$$Y_i^{data} = \frac{N_i^{e-} \cdot PS}{Q_i \cdot_i \cdot L_i} \tag{3.16}$$

Where,

- N_i are the total number of electrons that passed the 'good' electron cut.
- $_i$ is the combination of all efficiencies including tracking efficiency, trigger efficiency and Čherenkov efficiency for a specific run, i.
- Q_i is the accumulated charge from the BCMs for a given run, i.
- PS is the pre-scale for a given run, i. Described in 2.6.2.
- Li is the total live time of the for a given run, i.

The period over which a run is collecting data is somewhat arbitrary if all other experimental parameters remain the same throughout the run. For this reason, the

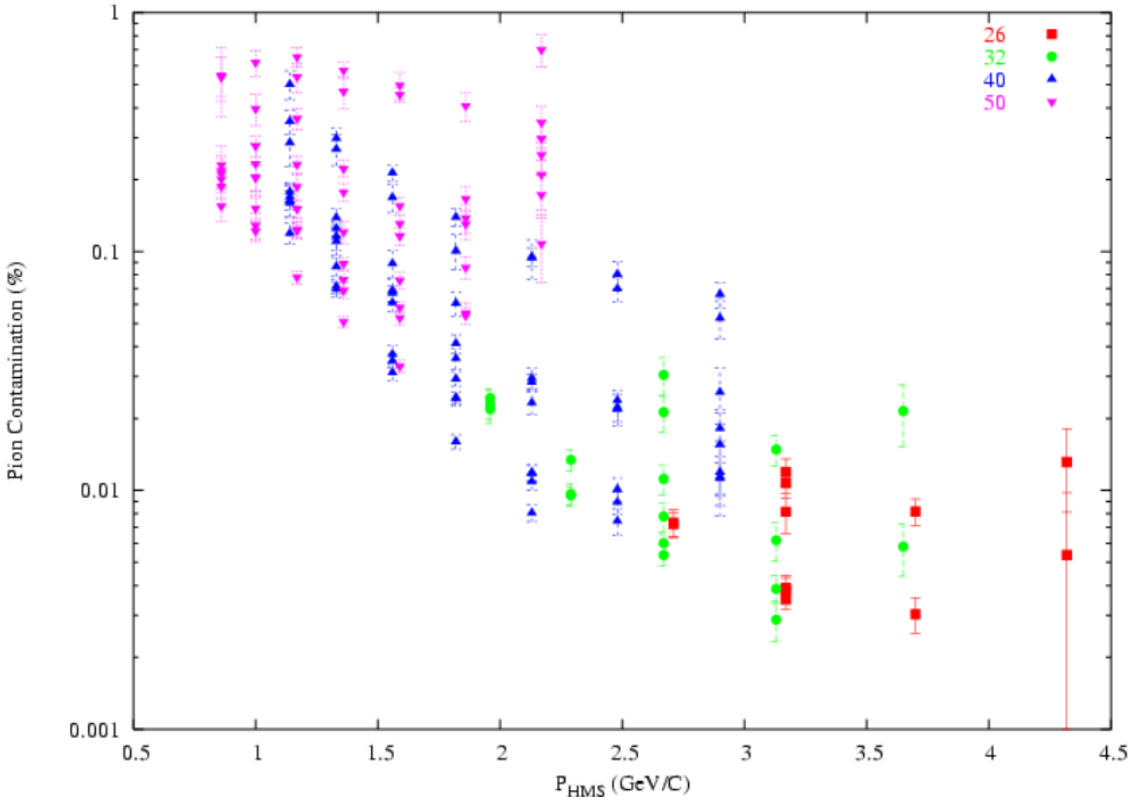
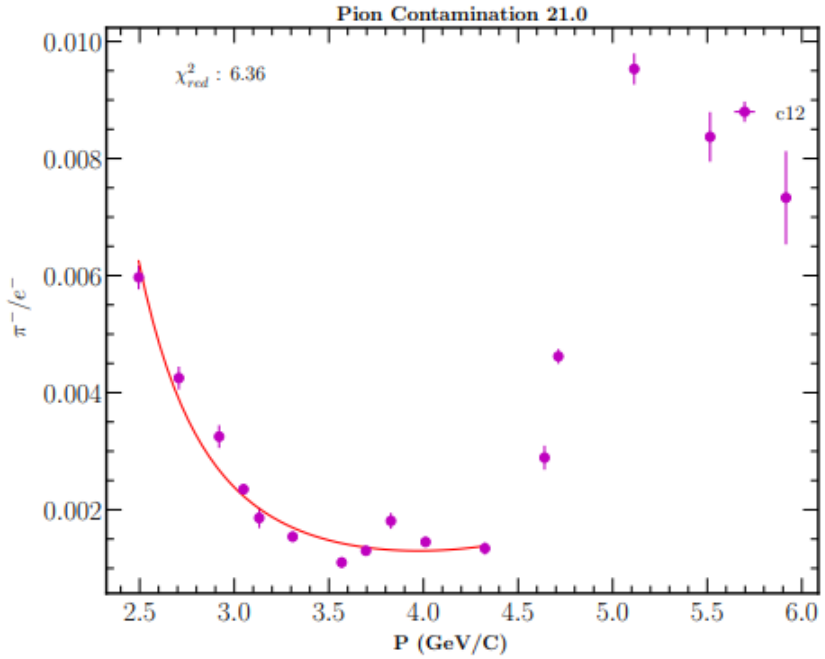
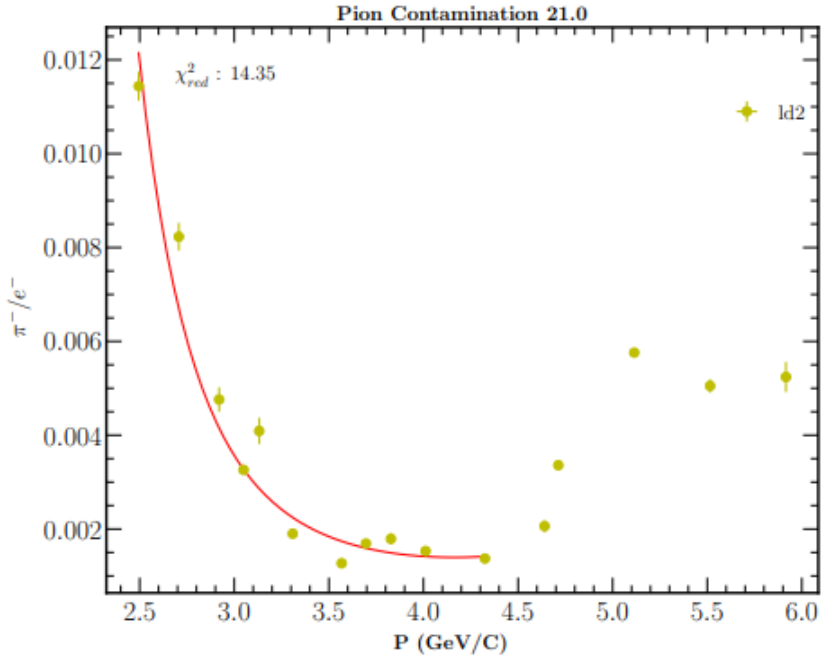


Figure 3.26: Pion contamination for experiment E02-019. Pion contamination was down to less than 0.01% at the lowest angle setting. The kinematics for this experiment were 13.1° and 9.8GeV/c, so the pion contamination is expected to be smaller. Reprinted with permission from [31].



(a)



(b)

Figure 3.27: pion-to-electron ratio for SHMS for Carbon and Deuterium.

electron yield for the entire experiment for a given target can be written as:

$$Y_{tot} = \frac{\sum_i N_i \cdot PS_i}{\sum_i Q_i \cdot_i \cdot L_i} \tag{3.17}$$

This method is an improvement over adding the runs according to Poisson statistics. It is often not the case that every run in the experiment is treated equivalently since there are time-dependent corrections. The time-dependent corrections are treated on a run-by-run basis and the statistics are accumulated as described above. The dominant error on an experiment like this is the statistical error on the number of counts, $\sqrt{N_{e-}}$. Statistical errors are also propagated for each efficiency, and live time factor. The charge normalized yield is typically binned in kinematic variables and target reconstruction variables to verify the data quality. The charge normalized yield is then compared to the acceptance Monte Carlo weighted by the radiated model as described in 4.1.2. Any momentum offsets are used to re-calculate x on an event-by-event basis. The aluminum dummy is subtracted from the deuterium data and composite targets such as boron have carbon subtracted.

Chapter 4

Cross Section Extraction

4.1 Cross Section Extraction

Up to this point, only the charge normalized electron yield has been discussed. The detector system and trigger is largely separate from the optics system that focuses events into the detector hut. In order to correct for the finite acceptance of the spectrometer, we use a Monte-Carlo that transports particles from the target volume, through the optics and into the detector stack. The probability of an event propagating into the detector hut is reconstructed in phase space variables $(\delta, x'_{tar}, y'_{tar})$. A cross section model is presented in the y-scaling formalism. Radiative corrections are applied to the cross-section model to match the experimental data based on the Tsai formalism[49]. A table of systematic errors is presented as a summary of previous sections.

4.1.1 Cross Section Extraction Methodology

There are two approaches to obtain the cross-section reported in the literature: The acceptance correction method and the ratio method.

4.1.2 Monte-Carlo Ratio Method

Events are generated in a cylindrical volume with a Gaussian beam profile to match the beam interacting with the target. Each event is transported through the optics elements given its initial momentum and energy. The detector hut is simulated with simple planes used to determine if events would have passed through the detector. Multiple scattering and particle decay are simulated at each transport if required. The resulting distribution of events that made it to the Monte-Carlo are weighted according to their initial state in the radiated model. The radiated model cross-section weighted acceptance Monte-Carlo can then be directly compared to the charge normalized data yield. Given the data and Monte-Carlo share the same binning, the ratio of data to Monte-Carlo can be compared. and the born cross section can be applied. In this way, the radiative effects are removed upon iterating the model until agreement is reached between data and monte-carlo.

4.2 Radiative Corrections

The born cross-section is not directly obtained because of additional processes that occur in the scattering of electrons off nuclei and nucleons. Radiative corrections are processes whereby the incoming or outgoing electron or hadron emit a real or virtual photon. The main contributions are summarized in figure **??**. For large acceptance spectrometers such as the HMS and SHMS, the effects of radiation are simulated in a Monte Carlo where the input model is iterated until agreement between the data and Monte Carlo is met. The foundations of unfolding the entire cross-section used to weight the Monte Carlo are discussed at length in Ref. [50]. This technique is in contrast to earlier experiments with narrow acceptance that utilized a correction factor calculated at a given Q^2 and W. The formalism used to compute radiative effects is described in Refs. [50–52].

Radiative effects in electron scattering are separated into the external and internal corrections. External corrections, those where a real photon is radiated due to the field of nuclei other than the target nucleon. These processes happen far away from the primary scattering vertex and as such scatter incoherently, so no interference is observed. The internal radiative effects refer to the interaction of the incoming or outgoing electron or hadron in the field of the target nucleus. The result is coherent scattering, which leads to interference terms that must be calculated. Figure 4.1 shows the Feynman diagrams for the first order processes accounted for in this work. $\gamma - Z$ interference and hadronic radiation were not included here as they are negligible contributions for this experiment. The second order corrections preserved are those processes that cancel infrared divergent terms from the first order corrections (vacuum polarization, self-energy diagrams, etc.).

There are multiple approximations typically used in calculating radiative corrections due to the high computational intensity. The so-called peaking approximation treats the Bremsstrahlung radiation primarily as a single-photon process along the radiating particle direction. The peaking approximation was not used here and the full treatment of Bremsstrahlung radiation was used. The method of equivalent radiators is a semi-empirical formula obtained by assuming that the effect of the internal bremsstrahlung on the elastic or inelastic electron scattering is equivalent to placing one radiator before the scattering and another radiator of the same thickness after the scattering[49].

4.3 Cross Section Model

The cross-section model consists of two parts, a quasi-elastic part and deep inelastic part. The quasi-elastic part is calculated from a scaling function, namely F(y), the off-shell electron-nucleon cross-section and kinematic factor (K)

$$\frac{d\sigma}{d\Omega d\nu} = F(y) \cdot (Z \cdot \sigma_p + N \cdot \sigma_n) \cdot K \tag{4.1}$$

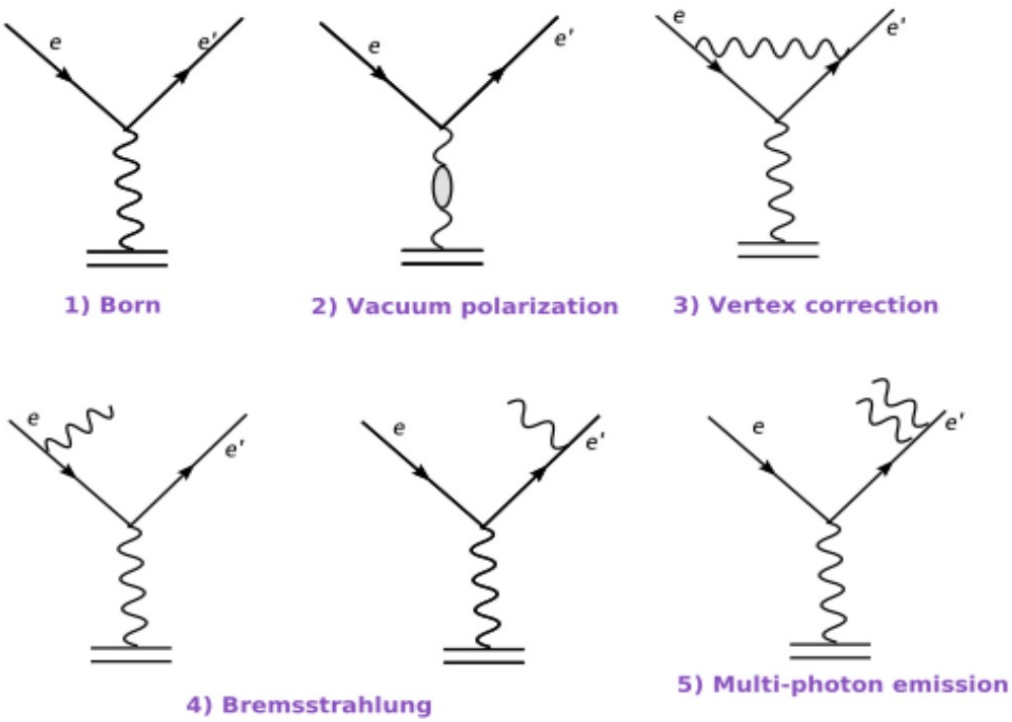


Figure 4.1: Feynman diagrams for internal and external radiative effects. Reprinted with permission from [47].

The scaling function for light nuclei takes the form proposed in [53]:

$$F(y) = (f_o - B) \cdot \frac{\alpha^2 e^{-(ay)^2}}{\alpha^2 + y^2} + Be^{-b|y|} \tag{4.2}$$

The parameters a, b, f_o, B and α are fits to the data for each target. For unmeasured targets, the initial parameters are the same as those for carbon.

4.3.1 Coulomb Corrections

The acceleration (deceleration) of charged particles of incoming (outgoing) electrons in the Coulomb field of nuclei must be accounted for. This correction is known as a coulomb correction. The nucleus accelerates the electron upon approach compared to the measured beam energy and vice versa for the scattered electron. A local Effective Momentum Approximation (EMA) was [54] used to account for this effect. The enhancement of the momentum is given as: $k'_f = k_f + \Delta k$, where $\Delta k = -0.775 V_o/c$.

4.3.2 Iterative model cross-section

The quasi-elastic contribution is determined by subtracting the inelastic contribution described below and fitting the model. The model deviates from experimental results at low Q^2 and negative values of y. This corresponds to high-x ($x > 1.4$) where final state interactions become expressed. A simple polynomial fit is applied to this region and the model is iterated.

The inelastic cross-section is well measured at moderate values of x and the nucleon structure functions from such data can be used to construct the inelastic cross-section at high-x. World data on the proton and neutron structure functions ($F_2^n and F_2^p$) are smeared out using a momentum distribution n(k). The momentum distribution is constructed from the F(y) scaling model used to form the quasi-elastic part of the cross-section. Imperfections in this model fit are corrected with a polynomial fit, and at ($x > 0.9$) only a smearing prescription is used. A smooth transition between low-x

and high-x is accomplished with a weighted ratio in ($0.8 < x < 0.9$). This model has had great success for previous inclusive measurements.

4.4 Systematic Errors

Most of the systematic errors have been presented in their relevant sections. This section is presented as an overview of all systematic errors calculated with links to the section in which they are discussed.

The beam energy, angle, and momentum all have systematic errors associated with them and they are related to one another. To evaluate the effect kinematic quantities have on the cross-section, the cross-section model was evaluated at shifted kinematics. The shifts correspond to our ability to resolve the beam energy, angle, and momentum. The shifts used were $\pm 0.02\%$, $\pm 0.01\%$, and 0.5 mr for beam energy, SHMS momentum, and SHMS angle respectively. An additional point-to-point shift of 0.2 mr to account for re-setting the SHMS angle to 13.1 degrees between days. The correlated error between the beam energy and spectrometer momentum is not reported here. Table 4.1 summarizes the systematic errors for the 2019 data set. Details are provided for each in their relevant section.

Table 4.1: Systematics Summary. The scale errors are errors associated with the absolute scale of the cross-section measurement. Point-to-point errors are variations on individual data points. The values in the last column are errors on the cross-section ratio.

Source	**Scale**	**Point-to-Point**	$d\sigma/\sigma$
Trigger Eff	-	0.02%	0.02%
CPU LT	-	-	-
Calo Eff	-	-	-
Positrons	-	-	-
Track Eff	1.00%	0.20%	1%
Targ Boil	0.44%	0.20%	0.50%
τ_D	0.6%	-	0.6%
τ_C	0.5%	-	0.5%
τ_{B10}	0.66%	-	0.66%
τ_{B11}	0.65%	-	0.65%
Cer Eff (delta dep)	-	0.20%	0.20%
Ytar accpt. Cor	-	0.5%	-
Charge	1%	0.35%	1%
Pion Contamination	-	0.30%	0.50%

Chapter 5

Results and Conclusion

In this chapter, the results for the commissioning phase of the XEM2 experiments is presented. Differential cross sections for Deuterium, Carbon, Boron-10 and Boron-11 are presented. The cross section ratio to deuterium is presented. The extracted a_2 ratios are presented in comparison to world data as a function of a commonly used model for nuclear density for light nuclei. All results are presented with statistical error bars only.

5.1 Cross Sections

The measured cross-sections are shown for Deuterium, Boron-10, Boron-11, and Carbon in figure 5.1. The data are plotted as a function of x, and the characteristic quasi-elastic peak can be seen for deuterium.

5.2 Inclusive SRC Ratios

2N SRCs were studied by taking cross section ratios to deuterium. The plateau is believed to be a signature of 2N correlations, as described in chapter 1. Scattering from a correlated pair is believed to occur in the x range: $1.4 < x < 2.$, while scattering from a single moving nucleon occurs at $x < 1.4$. The cross section ratio to

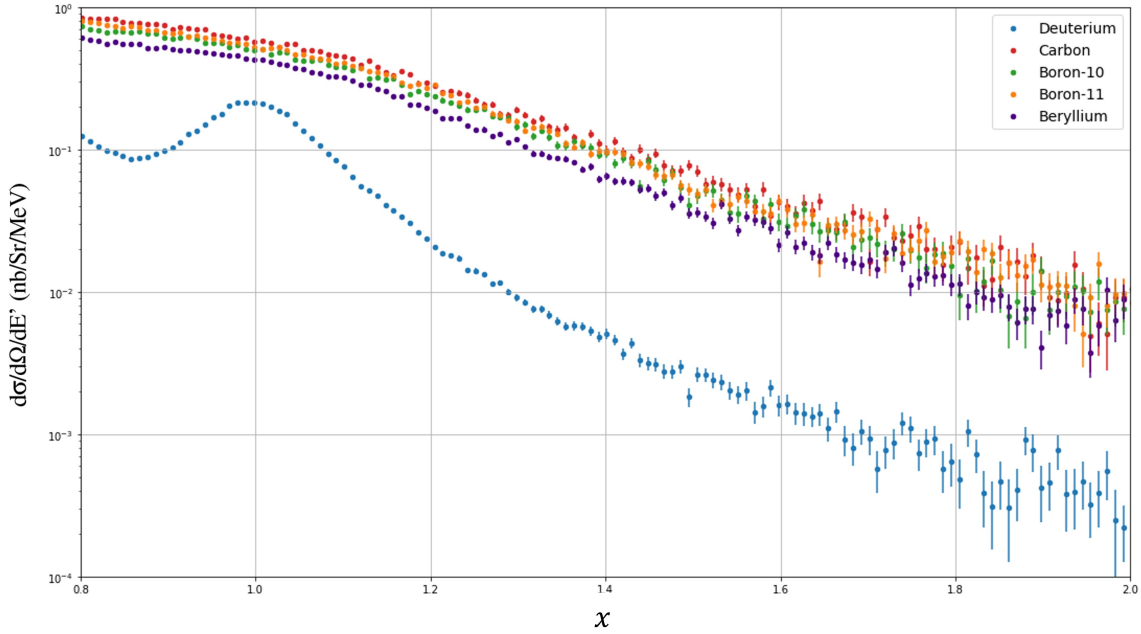


Figure 5.1: Spring 2019 cross-section. Nominal acceptance from $x > 1.35$, expanded to include quasi-elastic peak.

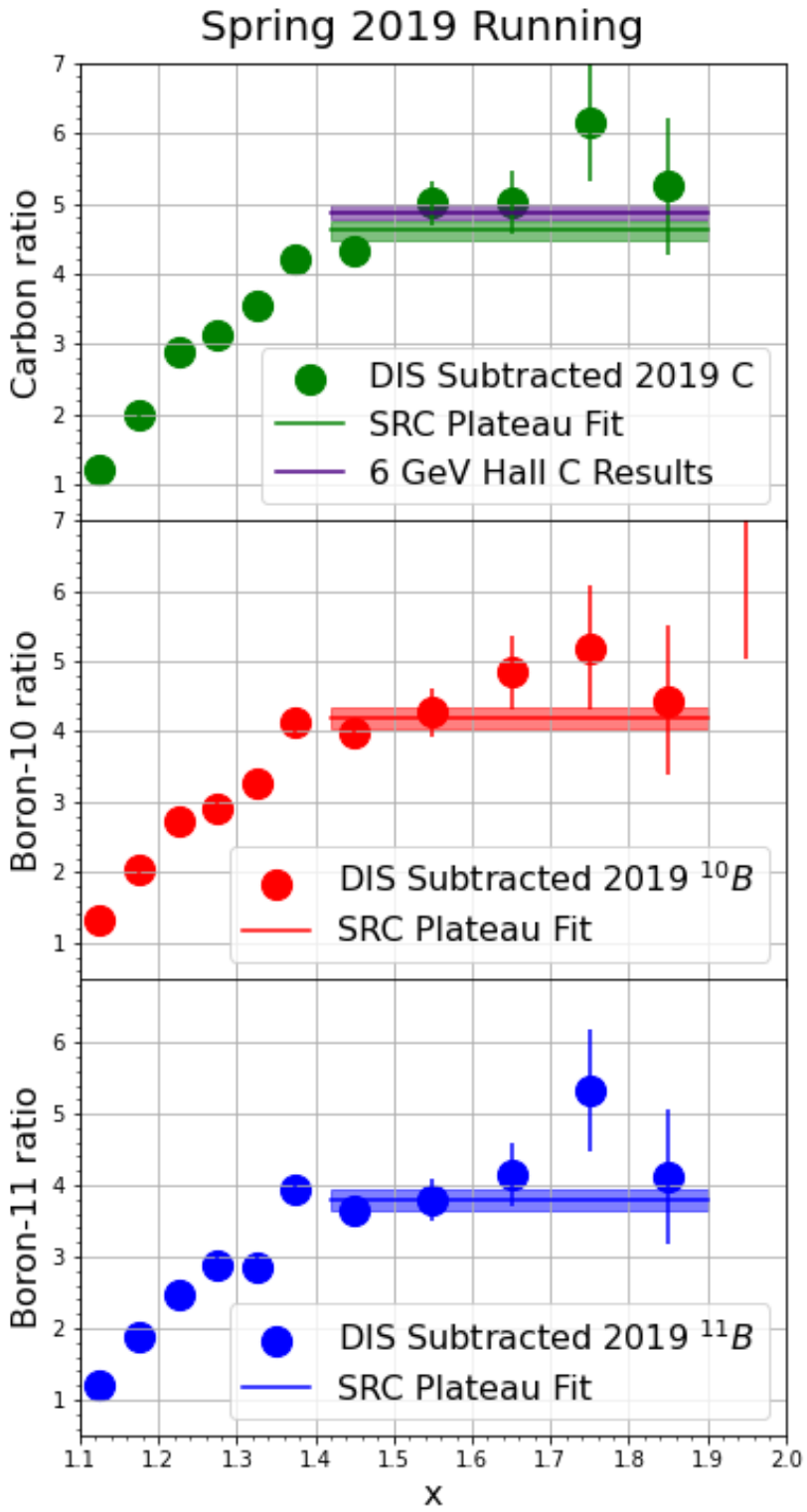


Figure 5.2: New measurements of a_2 ratio for ^{10}B and ^{11}B. Carbon for this experiment compared to Hall C 6 GeV results.

deuterium is limited by the aluminum container holding the liquid deuterium and the kinematic limits of deuterium. The contribution from the container grow as a function of x and account for 100% of the cross-section at $x \approx 2$. As in previous inclusive measurements, the FSIs cancel in the ratio. There is good agreement between carbon from this experiment and carbon from the 6 GeV inclusive experiment.

5.3 a_2 Ratios and Scaled Nuclear Density

Light nuclei are an ideal for the study of SRCs because they can be directly compared to calculations of the nuclear ground state using 2-body and 3-body forces[55]. Short range correlations can be studied in connection to the local density of the nuclear medium they experience. Figure 5.3 shows the extracted SRC plateau, a_2 compared to a calculation of nuclear scaled density[56].

5.4 Summary and Conclusion

The first 2N SRC measurements were made on ^{10}B and ^{11}B during commissioning of the SHMS in spring 2018 and spring 2019. The 2018 data was unrecoverable due to optics issues discovered after the data was collected. The extracted SRC plateaus for C, ^{10}B and ^{11}B are shown in figure 5.2 for the 2019 commissioning period. Carbon was found to agree with previous measurements at SLAC and JLab giving confidence in our measurement on Boron-10 and Boron-11. Future comparisons are planned for Boron-10 and Boron-11 to nuclear ground state calculations. The SHMS was successfully characterized for the full experiment run. The success of the full experiment was primarily the result of the commissioning experiments described here.

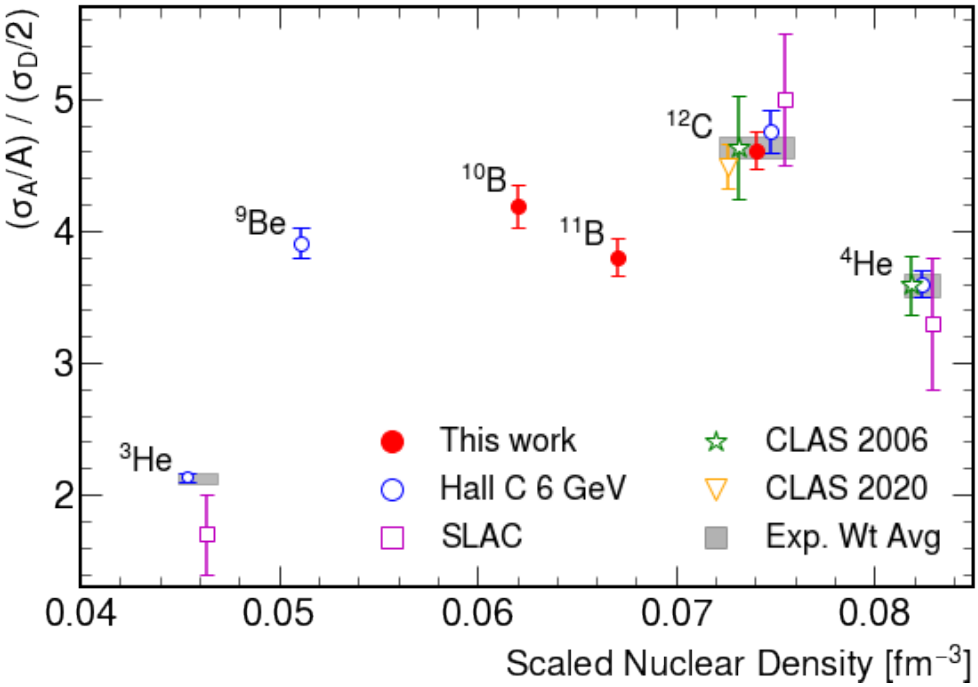


Figure 5.3: a_2 plateau with statistical error bars compared to world data versus scaled nuclear density. The nuclear density, extracted from [56], is scaled by $A/(A-1)$. Red circles are new measurements for ^{10}B and ^{11}B from this work. Blue circles are from the Hall C 6 GeV measurement, [31]. Magenta squares are from the SLAC experiment[57]. The yellow triangle and green stars are from CLAS20[58] and CLAS06[59] respectively.

Bibliography

[1] J. Arrington, "Update to proposal e12-06-105inclusive scattering from nuclei at $x > 1$ in the quasielastic and deeply inelastic regimes," 2019.

[2] G. Garvey, D. Harris, H. Tanaka, R. Tayloe, and G. Zeller, "Recent advances and open questions in neutrino-induced quasi-elastic scattering and single photon production," eng, *Physics reports*, vol. 580, no. C, pp. 1–45, 2015, ISSN: 0370-1573.

[3] J. Bjorken, "Asymptotic sum rules at infinite momentum," eng, *Physical review*, vol. 179, no. 5, pp. 1547–1553, 1969, ISSN: 0031-899X.

[4] [Online]. Available: http://www.mit.edu/~hasell/DKH_zeus.html.

[5] C. G. Callan and D. J. Gross, "High-energy electroproduction and the constitution of the electric current," *Phys. Rev. Lett.*, vol. 22, pp. 156–159, 4 1969. DOI: 10.1103/PhysRevLett.22.156. [Online]. Available: https://link.aps.org/doi/10.1103/PhysRevLett.22.156.

[6] C. E. Carlson and J. L. Poor, "Distribution amplitudes and electroproduction of the delta and other low-lying resonances," *Phys. Rev. D*, vol. 38, pp. 2758–2765, 9 1988. DOI: 10.1103/PhysRevD.38.2758. [Online]. Available: https://link.aps.org/doi/10.1103/PhysRevD.38.2758.

[7] D. Nguyen, "The isospin dependence of short range correlations through inclusive electron scattering from 40ca and 48ca," Ph.D. dissertation, University of Virginia, 2018.

[8] O. Benhar, "D. day, and i. sick," *Rev. Mod. Phys*, vol. 80, no. 189, p. 50, 2008.

[9] J. Arrington, "Inclusive scattering from nuclei at $x > 1$ in the quasielastic and deeply inelastic regimes.," Argonne National Lab, Tech. Rep., 2006. [Online]. Available: https://www.jlab.org/exp_prog/proposals/06/PR12-06-105.pdf.

[10] A. Rinat and M. Taragin, "Some remarks on off-shell scattering in the eikonal approximation and applications to semi-inclusive reactions," *Nuclear Physics A*, vol. 623, no. 3-4, pp. 519–528, 1997.

[11] D. Day, J. McCarthy, T. Donnelly, and I. Sick, "Scaling in inclusive electron-nucleus scattering," *Annual Review of Nuclear and Particle Science*, vol. 40, no. 1, pp. 357–410, 1990.

[12] B. L. Cohen, *Concepts of nuclear physics*. 1971.

[13] G. Choppin, J.-O. Liljenzin, and J. Rydberg, *Radiochemistry and nuclear chemistry*. Butterworth-Heinemann, 2002.

[14] B. Martin, "Nuclear and particle physics an introduction second edition," 2021.

[15] J. Mougey, "The (ee'p) reaction," *Nuclear Physics A*, vol. 335, no. 1-2, pp. 35–53, 1980.

[16] D. S. Koltun, "Total binding energies of nuclei, and particle-removal experiments," *Physical Review Letters*, vol. 28, no. 3, p. 182, 1972.

[17] L. Lapikas, "Quasi-elastic electron scattering off nuclei," *Nuclear Physics A*, vol. 553, pp. 297–308, 1993. DOI: https://doi.org/10.1016/0375-9474(93)90630-G..

[18] J. Arrington, D. Higinbotham, G. Rosner, and M. Sargsian, "Hard probes of short-range nucleon–nucleon correlations," *Progress in Particle and Nuclear Physics*, vol. 67, no. 4, pp. 898–938, 2012, ISSN: 0146-6410. DOI: https://doi.org/10.1016/j.ppnp.2012.04.002. [Online]. Available: http://www.sciencedirect.com/science/article/pii/S0146641012000749.

[19] R. B. Wiringa, V. G. J. Stoks, and R. Schiavilla, "Accurate nucleon-nucleon potential with charge-independence breaking," *Phys. Rev. C*, vol. 51, pp. 38–51, 1 1995. DOI: 10.1103/PhysRevC.51.38. [Online]. Available: https://link.aps.org/doi/10.1103/PhysRevC.51.38.

[20] A. Schmidt *et al.*, "Probing the core of the strong nuclear interaction," *Nature*, vol. 578, no. 7796, pp. 540–544, 2020.

[21] R. Machleidt, "High-precision, charge-dependent bonn nucleon-nucleon potential," *Phys. Rev. C*, vol. 63, p. 024 001, 2 2001. DOI: 10.1103/PhysRevC.63.024001. [Online]. Available: https://link.aps.org/doi/10.1103/PhysRevC.63.024001.

[22] V. G. J. Stoks, R. A. M. Klomp, C. P. F. Terheggen, and J. J. de Swart, "Construction of high-quality nn potential models," *Phys. Rev. C*, vol. 49, pp. 2950–2962, 6 1994. DOI: 10.1103/PhysRevC.49.2950. [Online]. Available: https://link.aps.org/doi/10.1103/PhysRevC.49.2950.

[23] N. Ishii, S. Aoki, and T. Hatsuda, "Nuclear force from lattice qcd," eng, *Physical review letters*, vol. 99, no. 2, pp. 022 001–022 001, 2007, ISSN: 0031-9007.

[24] T. W. Donnelly, J. A. Formaggio, B. R. Holstein, R. G. Milner, and B. Surrow, *Foundations of nuclear and particle physics*. Cambridge University Press, 2017.

[25] R. Subedi *et al.*, "Probing cold dense nuclear matter," *Science*, vol. 320, no. 5882, pp. 1476–1478, 2008.

[26] O. Hen, D. W. Higinbotham, G. A. Miller, E. Piasetzky, and L. B. Weinstein, "The emc effect and high momentum nucleons in nuclei," *International Journal of Modern Physics E*, vol. 22, no. 07, p. 1 330 017, 2013.

[27] J. Arrington, A. Daniel, D. Day, N. Fomin, D. Gaskell, and P. Solvignon, "Detailed study of the nuclear dependence of the emc effect and short-range correlations," *Physical Review C*, vol. 86, no. 6, p. 065 204, 2012.

[28] A. Gezerlis *et al.*, "Quantum monte carlo calculations with chiral effective field theory interactions," *Physical review letters*, vol. 111, no. 3, p. 032 501, 2013.

[29] J. Hoppe, C. Drischler, R. Furnstahl, K. Hebeler, and A. Schwenk, "Weinberg eigenvalues for chiral nucleon-nucleon interactions," *Physical Review C*, vol. 96, no. 5, p. 054 002, 2017.

[30] A. Tropiano, S. Bogner, and R. Furnstahl, "Short-range correlation physics at low renormalization group resolution," *Physical Review C*, vol. 104, no. 3, p. 034 311, 2021.

[31] N. Fomin, "Inclusive electron scattering from nuclei at $x > 1$ and high q**2 with a 5.75-gev beam," Ph.D. dissertation, Virginia U., 2008. arXiv: 0812.2144 [nucl-ex].

[32] J.-J. Aubert *et al.*, "The ratio of the nucleon structure functions f2n for iron and deuterium," *Physics Letters B*, vol. 123, no. 3-4, pp. 275–278, 1983.

[33] A. Bodek *et al.*, "Electron scattering from nuclear targets and quark distributions in nuclei," *Physical Review Letters*, vol. 50, no. 19, p. 1431, 1983.

[34] J. Gomez *et al.*, "Measurement of the a dependence of deep-inelastic electron scattering," eng, *Physical review. D, Particles and fields*, vol. 49, no. 9, pp. 4348–4372, 1994, ISSN: 0556-2821.

[35] *The 12 GeV Energy Upgrade at Jefferson Laboratory*, 2012. [Online]. Available: https://accelconf.web.cern.ch/LINAC2012/papers/th3a02.pdf.

[36] C. Yero, "Cross section measurement of deuteron electro-disintegration at very high recoil momenta and large 4-momentum transfers (q2)," Ph.D. dissertation, 2020. DOI: 10.25148/etd.FIDC009154. [Online]. Available: https://digitalcommons.fiu.edu/etd/4479/.

[37] C. Yan, R. Carlini, and D. Neuffer, "Beam energy measurement using the hall c beamline," in *Proceedings of International Conference on Particle Accelerators*, IEEE, 1993, pp. 2136–2138.

[38] J. Arrington, "Inclusive electron scattering from nuclei at $x > 1$ and high q2," Ph.D. dissertation, 1998. DOI: 10.2172/859147. [Online]. Available: https://www.osti.gov/biblio/859147.

[39] S. A. Wood, "2019 version: Jefferson lab hall c standard equipment manual, 2019.," Jefferson Lab, Tech. Rep., 2019. [Online]. Available: https://hallcweb.jlab.org/safety-docs/current/Standard-Equipment-Manual.pdf.

[40] ——, *2019 version: Jefferson lab hall c standard equipment manual*, 2019. [Online]. Available: https://hallcweb.jlab.org/safety-docs/current/Standard-Equipment-Manual.pdf.

[41] G. Smith, *Cryotarget training*, 2019. [Online]. Available: https://userweb.jlab.org/~smithg/target/Qweak/HallACTgt_Training.pdf.

[42] J. Bericic, "Notes on hms$_o$*ptics*," Jefferson Lab, 2017. [Online]. Available: https://hallcweb.jlab.org/DocDB/0008/000849/001/HMS_optics_notes.pdf.

[43] C. Yero, "Hodoscopes calibration documentation," Jefferson Lab, Tech. Rep., 2021.

[44] J. Murphy, "Edtm study report," Jefferson Lab, Tech. Rep., 2022.

[45] D. Mack, "Non-obvious sources of dead time in nominally dead time-free electronics," Jefferson Lab, Tech. Rep., 2021.

[46] H. Szumila-Vance, "Notes on the shms optics in the 2017-18 run period," Jefferson Lab, 2019. [Online]. Available: https://hallcweb.jlab.org/DocDB/0010/001007/001/shmsNote.pdf.

[47] A. Karki, "Precise measurement of the nuclear dependence of the emc effect in light nuclei," Ph.D. dissertation, 2022. [Online]. Available: https://scholarsjunction.msstate.edu/cgi/viewcontent.cgi?article=6640&context=td.

[48] I. A. Richardson, J. W. Leachman, and E. W. Lemmon, "Fundamental equation of state for deuterium," *Journal of Physical and Chemical Reference Data*, vol. 43, no. 1, 2014.

[49] Y. Tsai, "Radiative corrections to electron scatterings," 1971. [Online]. Available: https://www.slac.stanford.edu/cgi-bin/getdoc/slac-pub-0848.pdf.

[50] L. W. MO and Y. S. TSAI, "Radiative corrections to elastic and inelastic ep and up scattering," *Rev. Mod. Phys.*, vol. 41, pp. 205–235, 1 1969. DOI: 10.1103/RevModPhys.41.205. [Online]. Available: https://link.aps.org/doi/10.1103/RevModPhys.41.205.

[51] Y.-S. Tsai, "Radiative corrections to electron-proton scattering," *Phys. Rev.*, vol. 122, pp. 1898–1907, 6 1961. DOI: 10.1103/PhysRev.122.1898. [Online]. Available: https://link.aps.org/doi/10.1103/PhysRev.122.1898.

[52] S. R. Dasu, "Precision measurement of x, Q^2 and a-dependence of $R = \sigma_L/\sigma_T$ and $F2$ in deep inelastic scattering," Ph.D. dissertation, 1988. [Online]. Available: https://wiki.jlab.org/xem2wiki/images/f/f1/Dasu.pdf.

[53] C. C. d. Atti and G. B. West, "Old and new facets of y-scaling: The universal features of nuclear structure functions and nucleon momentum distributions," *arXiv preprint nucl-th/9702009*, 1997.

[54] A. Daniel, "Precise measurement of the nuclear dependence of the emc effect," Ph.D. dissertation, 2006.

[55] R. Schiavilla and Wiringa, "Tensor forces and the ground-state structure of nuclei," *Phys. Rev. Lett.*, vol. 98, p. 132 501, 13 2007. DOI: 10.1103/PhysRevLett.98.132501. [Online]. Available: https://link.aps.org/doi/10.1103/PhysRevLett.98.132501.

[56] M. Piarulli, S. Pastore, R. B. Wiringa, S. Brusilow, and R. Lim, "Densities and momentum distributions in $A \leq 12$ nuclei from chiral effective field theory interactions," *Phys. Rev. C*, vol. 107, p. 014 314, 1 Jan. 2023. DOI: 10.1103/PhysRevC.107.014314. [Online]. Available: https://link.aps.org/doi/10.1103/PhysRevC.107.014314.

[57] L. L. Frankfurt, M. I. Strikman, D. B. Day, and M. Sargsian, "Evidence for short range correlations from high Q**2 (e, e-prime) reactions," *Phys. Rev. C*, vol. 48, pp. 2451–2461, 1993. DOI: 10.1103/PhysRevC.48.2451.

[58] B. Schmookler *et al.*, "Modified structure of protons and neutrons in correlated pairs," *Nature*, vol. 566, no. 7744, pp. 354–358, 2019. DOI: 10.1038/s41586-019-0925-9. arXiv: 2004.12065 [nucl-ex].

[59] K. S. Egiyan *et al.*, "Measurement of 2- and 3-nucleon short range correlation probabilities in nuclei," *Phys. Rev. Lett.*, vol. 96, p. 082 501, 2006. DOI: 10.1103/PhysRevLett.96.082501. arXiv: nucl-ex/0508026.

Vita

Casey Morean was born in 1995 in rural Pennsylvania. As a child, he would join his father out on the railroad where they would run a two-foot-guage locomotive. During the summer months, he and his family would travel to New Hampshire where he would work on his uncle's farm where he milked cows and stacked hay. In his teenage years, he set up his Lego train display at his father's national model railroaders association jamboree. Casey worked second shift at Super Abrasive Machining Innovations, LLC with his father in vibratory finishing of powder metal parts. Following a short term employed in a grocery store, Casey found himself back in manufacturing powder metal parts at Metal Powder Products.

Casey Morean attended Lock Haven University of Pennsylvania LHU) where he received a Bachelors in Applied Physics with a concentration in nanotechnology and a minor in mathematics and chemistry. He completed a certificate program in nano-manufacturing through Penn State University. In his Sophomore year, Casey participated in the Science Undergraduate Laboratory Internships (SULI) program at Oak Ridge National Laboratory. His project involved characterizing plasma temperatures using Thompson scattering under the supervision of Dr. Biewer.

Casey Morean returned to Tennessee in 2017 to start his PhD in physics at the University of Tennessee. Casey Morean received the outstanding graduate teaching assistant award in 2019 for his devotion to outcomes in physics teaching. TA of the Casey Morean began research with Dr. Fomin in 2019, and later that year received a Office of Science Graduate Student Research (SCGSR) fellowship at Thomas Jefferson

National Accelerator Facility. He received the Jefferson Science Associates (JSA) fellowship award the following year. During his time at the University of Tennessee, Casey has been a part of 3 peer reviewed articles, and 4 national conferences. He presented short range correlation results on Boron-10 and Boron-11 at the ECT* conference in Trento, Italy in summer of 2023.

Casey Morean plans to continue his nuclear physics research at the Catholic University of America.